โครงการวิจัยการสังเคราะห์ซิงค์ออกไซด์ที่มีโครงสร้างนาโนเพื่อใช้เป็นตัวเร่งปฏิกิริยาทางแสงโดยทางเคมีสารละลาย

โดย

ผศ.ดร. อนุกร ภู่เรืองรัตน์

ศ.ดร. สมชาย ทองเต็ม

กรกฎาคม 2557

สัญญาเลขที่ MRG5580112

รายงานวิจัยฉบับสมบูรณ์
โครงการวิจัยการสังเคราะห์ซิงค์ออกไซด์ที่มีโครงสร้างนาโนเพื่อใช้เป็นตัวเร่งปฏิกิริยาทางแสงโดยทางเคมีสารละลาย

โดย
ผศ.ดร. อนุกร ภู่เรืองรัตน์
ภาควิชาวิทยาศาสตร์และเทคโนโลยีวัสดุ
คณะวิทยาศาสตร์ มหาวิทยาลัยสงขลานครินทร์

ศ.ดร. สมชาย ทองเต็ม
ภาควิชาฟิสิกส์และวัสดุศาสตร์
คณะวิทยาศาสตร์ มหาวิทยาลัยเชียงใหม่

สนับสนุนโดยสำนักงานกองทุนสนับสนุนการวิจัย
(ความเห็นในรายงานนี้เป็นของผู้วิจัย สกว.ไม่จำเป็นต้องเห็นด้วยเสมอไป)

Acknowledgement

I would like to thank my supervisors, Professor Dr. Somchai Thongtem and Associate Professor Titipun Thongtem, for my great opportunities of their supervisions, valuable suggestion and all supports. I am also grateful the Thailand Research Fund, Office of Commission on Higher Education and Prince of Songkla university, Thailand for the research scholarship on this research. Finally, I would like to thank all helps and supports form officers and technical staffs of Department of Materials Science and Technology, Faculty of science, Prince of Songkla University and Elentron Microscopy Research and Service Center, Faculty of science, Chiang Mai University for all the analysis.

Assistant Professor Dr. Anukorn Phuruangrat

Project Code : MRG5580112

Project Title : Synthesis of nanostructured zinc oxide used for photocatalysis by chemical solution route

Investidator : Assistant Professor Dr. Anukorn Phuruangrat

Professor Dr. Somchai Thongtem

E-mail Address : phuruangrat@hotmail.com

Project Period : 2 years (July 2012 - June2014)

Abstract : Nowadays, environmental problems are becoming more and more harmful, due to the development of industries and economies of the world. The photocatalysts have been regarded as the most effective ways to solve such the problems. For a number of photocatalysts, one metal oxide like zinc oxide is one of promising materials used for degradation organic pollutants by utilizing UV or visible light and anti-bacteria. In this research is thus focused on the synthesis of nanostructured zinc oxide (ZnO) by chemical solution route for application use in photocatalytic degradation of organic solvent.

Keywords : ZnO; Photocatalyst; Nanostructure

รหัสโครงการ : MRG5580112

ชื่อโครงการ : การสังเคราะห์ซิงค์ออกไซด์ที่มีโครงสร้างนาโนเพื่อใช้เป็นตัวเร่งปฏิกิริยาทางแสงโดยทางเคมีสารละลาย

ชื่อนักวิจัย : ผู้ช่วยศาสตราจารย์ ดร. อนุกร ภู่เรืองรัตน์
ศาสตราจารย์ ดร. สมชาย ทองเต็ม

E-mail Address : phuruangrat@hotmail.com

ระยะเวลาโครงการ : 2 ปี (กรกฎาคม 2555 – มิถุนายน 2557)

บทคัดย่อ : ปัจจุบันปัญหาสิ่งแวดล้อมที่เกิดเพิ่มมากขึ้นและเป็นอันตรายมากขึ้นเพราะเนื่องจากการพัฒนาของอุตสาหกรรมและเศรษฐกิจของโลก ตัวเร่งปฏิกิริยาทางแสงได้ถูกนำมาใช้ในการแก้ไขปัญหาดังกล่าวเนื่องจากวิธีนี้มีประสิทธิภาพสูง สำหรับตัวเร่งปฏิกิริยาทางแสงออกไซด์โลหะโดยเฉพาะย่างยิ่ง ซิงค์ออกไซด์เป็นหนึ่งในวัสดุที่ใช้สำหรับการย่อยสลายสารมลพิษอินทรีย์ภายใต้รังสียูวีหรือแสงที่มองเห็นและมีสมบัติต่อต้านแบคทีเรีย ในงานวิจัยนี้จึงมุ่งเน้นไปที่การพัฒนาสังเคราะห์ของโครงสร้างนาโนซิงค์ออกไซด์ (ZnO) โดยวิธีทางสารละลายเพื่อนำไปประยุกต์ใช้สำหรับการย่อยสลายปฏิกิริยาของตัวทำละลายอินทรีย์

คำหลัก : ZnO; Photocatalyst; Nanostructure

Tables of Contents

List of Figures

Chapter 1
Ultrasound-assisted synthesis, characterization and optical property of 0–3 wt% Sn-doped ZnO

1.1 Introduction

ZnO (3.37 eV wide band gap at room temperature and 60 meV large exciton binding energy) is one of the most promising semiconductors used for short wavelength optoelectronic devices operating in the blue and ultraviolet region. It has been investigated as transparent conductors and piezoelectric materials for solar cells, transparent electrodes and gas sensors. To enhance the electrical/optical properties, ZnO was doped with group III, IV and V elements due to its superior conducting properties based on oxygen vacancies [1–6]. Recently, ZnO doped with Al, Ga, In, Sn and Sb were reported to have high potential applications for gas sensors, dye-sensitized solar cells and photocatalysis [6–8]. In particular, ZnO film doped with 1–2 at% Al exhibited low resistivity and was regarded as an alternative potential candidate for indium-tin-oxide [1,9]. In-doped ZnO films showed excellent conductive property and high transparency [10]. ZnO was able to emit shorter wavelengths by doping with In [11] and red spectrum by doping with Eu^{3+} ions [12]. The main reason of choosing tin-doped ZnO is to enhance the electrical conductivity. When ZnO is doped with Sn^{4+}, the ions substitute for Zn^{2+} sites in ZnO crystal, leading to two more negative charges to enhance the electrical conductivity. Furthermore, Zn^{2+} ions can be easily substituted by Sn^{4+} ions without large lattice distortion, because they are almost the same size (radii: Zn^{2+} = 0.074 nm, Sn^{4+} = 0.071 nm) [2-4, 13].

In this research, the synthesis of crystalline ZnO doped with different contents of Sn^{4+} via ultrasonic chemical method is reported. The ultimate goal is to improve the optical property of the crystals to utilize for visible sunlight.

1.2 Experiment

Typically, 0.01 mole zinc nitrate hexahydrate and 0–3 wt% Sn^{4+} of tin chloride were dissolved in 100 ml deionized water, into which a 28 % ammonium hydroxide solution was continuously dropped and stirred until the solution pH reaching at 8.5. Upon

irradiation with 35 kHz ultrasound at 80 ^{o}C for 3 h, the precipitates were synthesized, filtered, washed with methanol several times and dried at 80 ^{o}C for 12 h. The products were characterized by X-ray diffraction, electron microscopy and UV-visible spectrometry.

1.3 Results and discussion

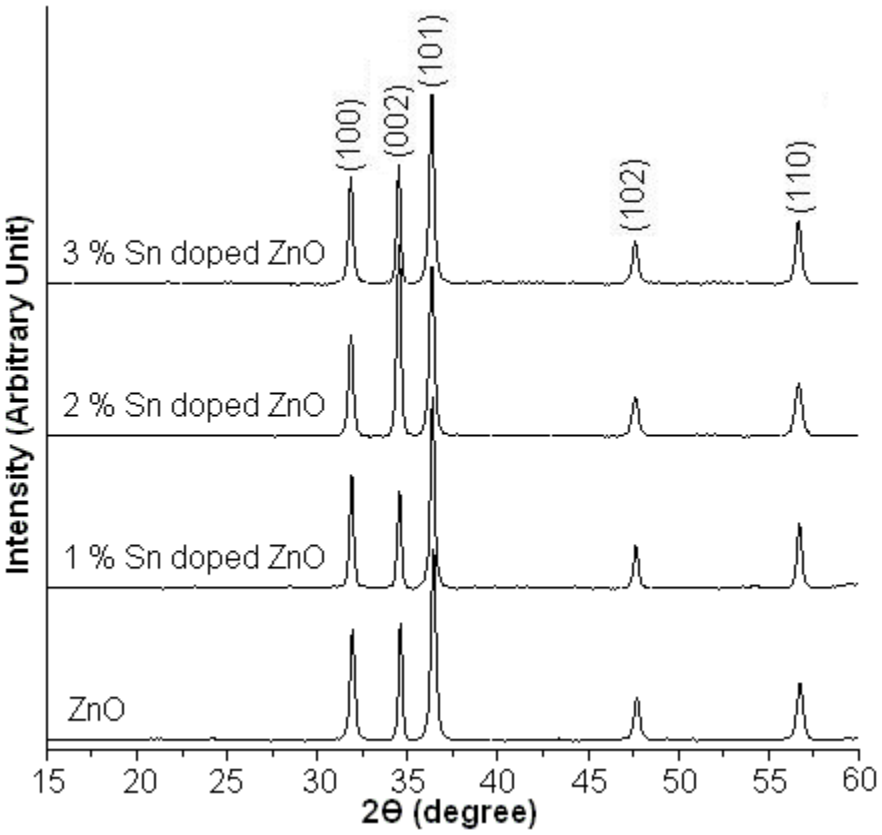

Fig. 1.1 XRD patterns of 0, 1, 2 and 3 wt% Sn-doped ZnO.

All diffraction peaks (Fig. .1.1) were identified to correspond with hexagonal wurtzite structured ZnO (JCPDS No. 36-1451) as the main product [6,14]. Incorporation of Sn in crystalline lattice of ZnO host can play the role in density of the native point defects such as vacancies, interstitials and anti-sited defects; especially, the host with higher concentration of dopant. It should be noted that Sn concentration of the Sn-doped ZnO samples was so low that the elemental Sn was unable to be detected by this XRD analysis.

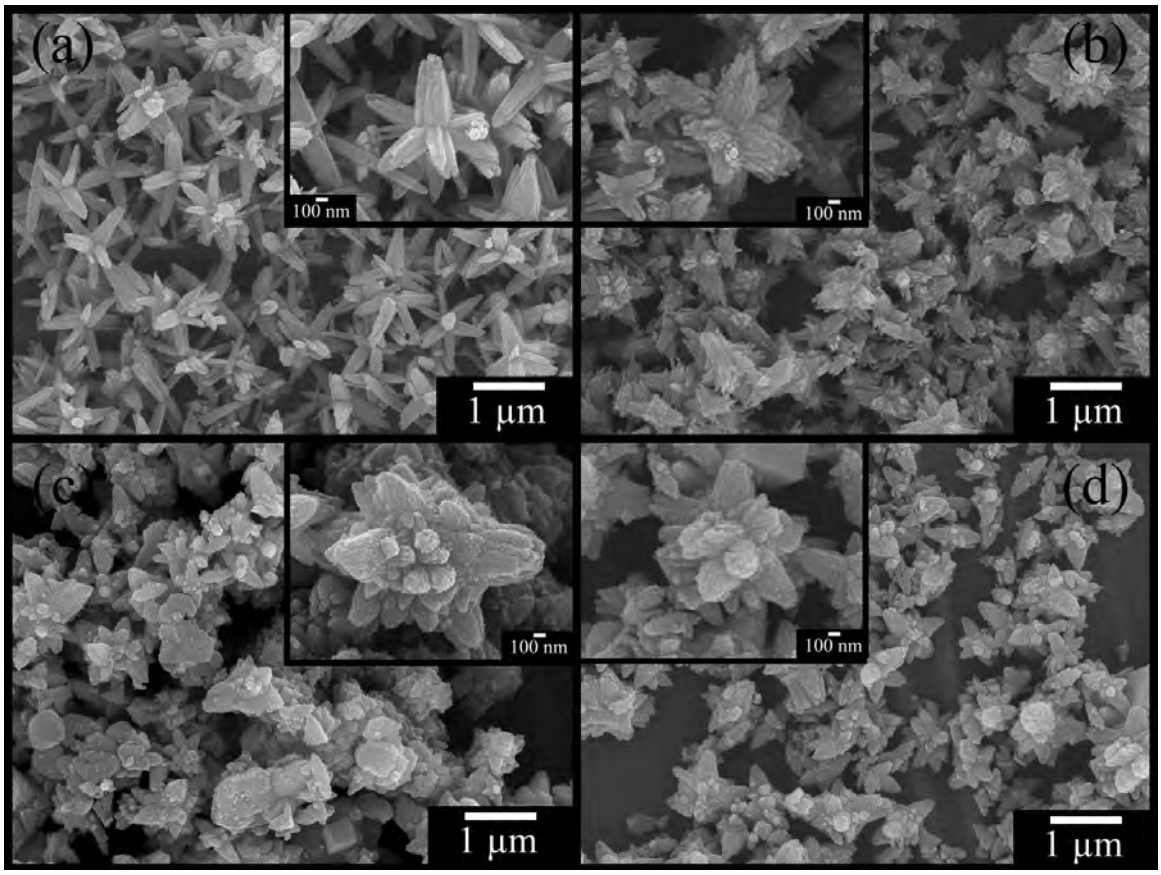

Fig. 1.2 SEM images of (a–d) 0, 1, 2 and 3 wt% Sn-doped ZnO, respectively.

General morphology of the as-synthesized ZnO (Fig. 1.2a) was uniform flower-like nanostructure composed of different oriented petals directly grown out of the bases of central crystalline towers. Diameters of the towers gradually decreased from 400 nm at the bottom to 200 nm at the tip. Each of the petals and towers was composed of several parallel agglomerated ZnO nanorods. Upon doping with different contents of Sn, the product shapes were still flowers for 1 wt% Sn-doped ZnO (Fig. 1.2b), and agglomerates of nanoparticles for 2 and 3 wt% Sn-doped ZnO (Fig. 1.2c and d). The 1 wt% Sn-doped ZnO shows petals and towers composed of multineedles with 20-120 nm long and 20 nm diameter grown from central cores. A number of agglomerated nanoparticles composing the petals were detected in both the 2 and 3 wt% Sn-doped ZnO.

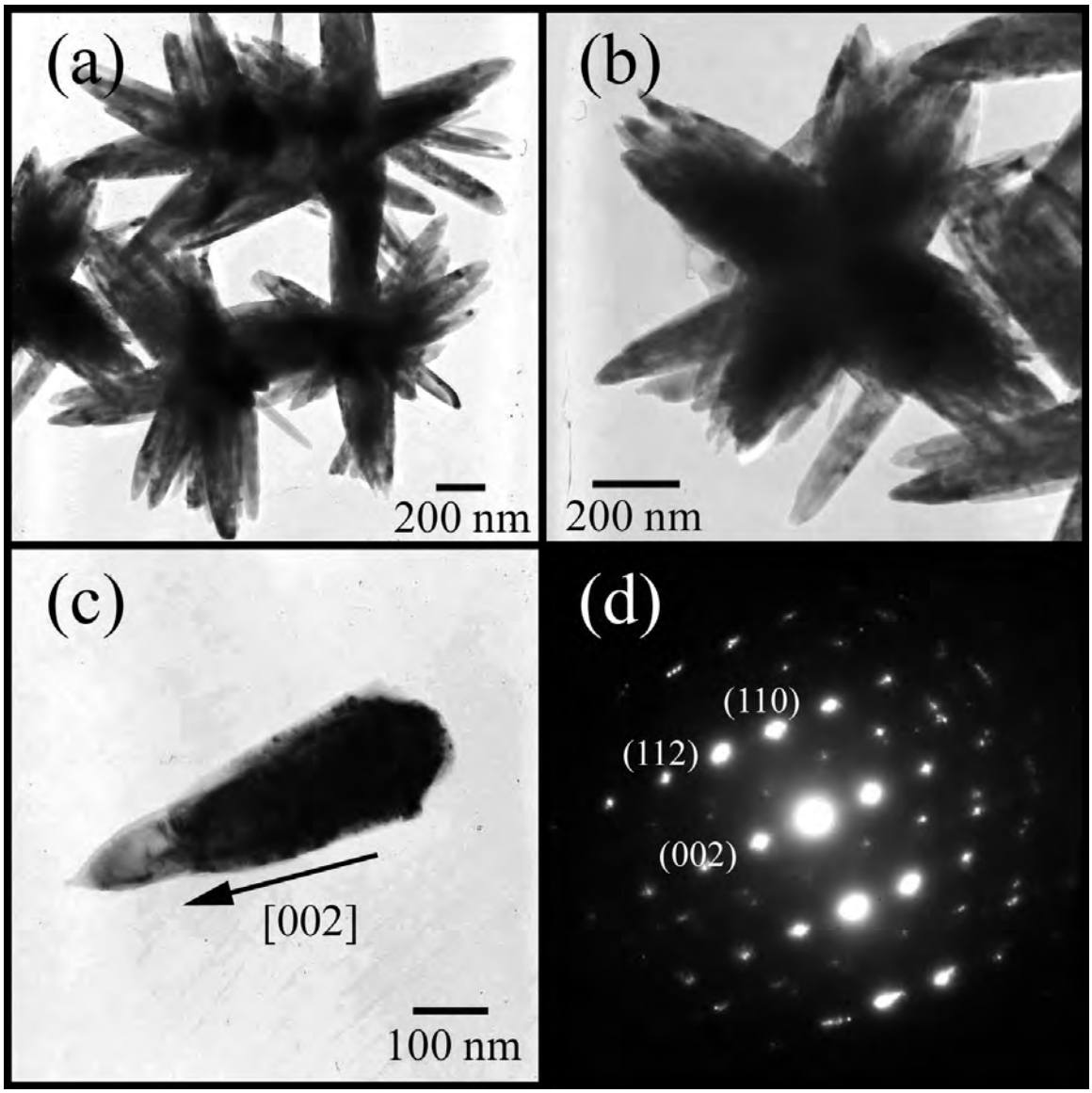

Fig. 1.3 TEM images and SAED pattern of pure ZnO flowers.

The elemental composition of the as-synthesized samples was analyzed by EDX (results not shown). For this analysis, zinc and oxygen with 1:1 atomic ratio were detected for pure ZnO, including the detection of additional Sn for 1, 2 and 3 wt% Sn-doped ZnO. Intense peaks of Cu and Au originated from Cu stubs and sputtered Au were also detected. The EDX mapping of 3 wt% Sn-doped ZnO was mainly composed of uniformly distributive Zn, O and Sn, which revealed the random doping of Sn in the crystal lattice.

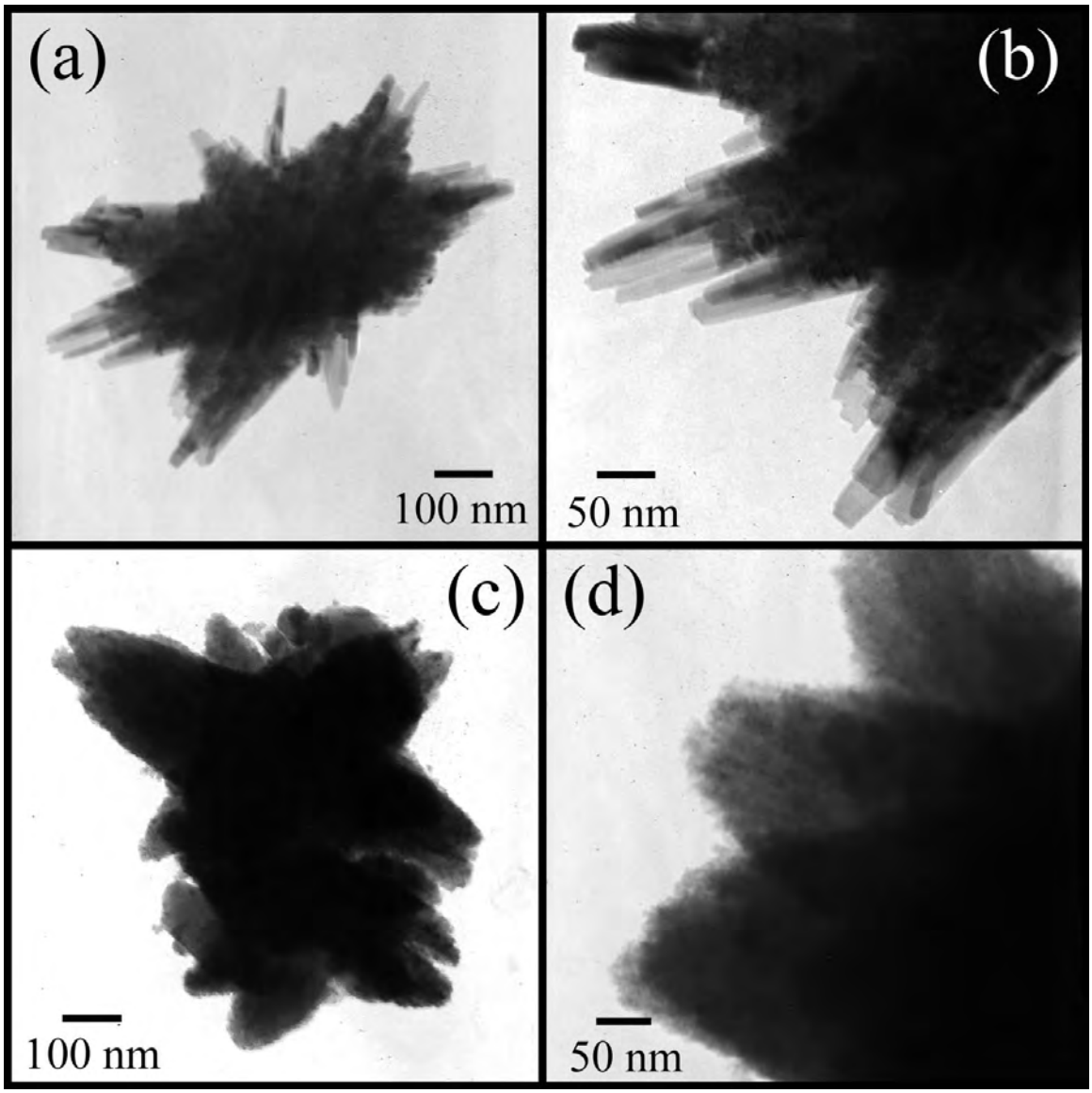

Fig. 1.4 TEM images of (a, b) 1 wt% and (c, d) 3 wt% Sn-doped ZnO.

TEM images of ZnO (Fig. 1.3a and b) present the uniform flower-like ZnO nanostructure, consisted of petals shaped like rods with sharp tips. The rod-like petals with the same size as those characterized by SEM were also detected, and have smooth surfaces. The petal (Fig. 1.3c) has a preferential growth along the c-axis. A SAED pattern (Fig. 1.3d) on a rod-like petal was composed of bright spots with 6-fold symmetry, belonging to hexagonal ZnO single crystal, with the [-110] direction as zone axis.

TEM images of the 1 and 3 wt% Sn-doped ZnO at low and high magnifications are shown in Fig. 1.4. At low magnification, the samples shaped like flowers composed of

multineedle-like petals grown out of cores for the first, and agglomeration of nanoparticles for the second. Close-up observation on them, a number of crystalline needles composed the petals were detected for the 1 wt% Sn-doped ZnO, and different orientations of nanoparticles built up agglomerations for the 3 wt% Sn-doped ZnO.

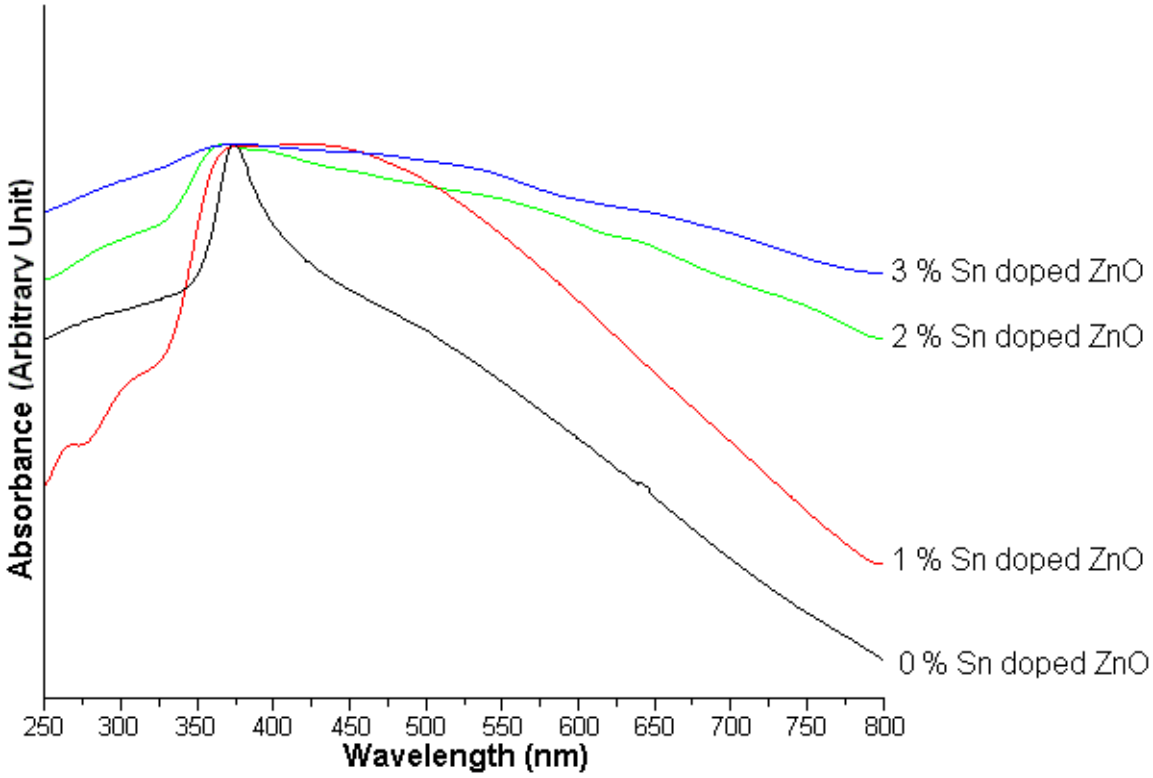

Fig. 1.5 Absorption spectra of 0, 1, 2 and 3 wt% Sn-doped ZnO.

UV-visible spectra (Fig. 1.5) of the as-synthesized 0–3 % Sn-doped ZnO revealed that the Sn dopant can play the role in changing the absorption characteristics of pure ZnO. Strong absorption band in UV region at 373 nm attributed to the band edge absorption of wurtzite hexagonal pure ZnO, blue shift relative to its bulk (380 nm) [15]. Those of the 1, 2 and 3 wt% Sn-doped ZnO were red-shift broad absorption bands from UV to visible regions, caused by the increase of lattice defects by dopant concentration increasing. Generally, the red-shift in absorption wavelength and the increase in absorption intensity were believed to relate with the increase in the electron–hole pair formation rate on the photocatalytic surfaces [8], resulting in the higher photocatalytic activity of Sn-doped ZnO utilizing for sunlight.

1.4 Conclusions

Samples of 0, 1, 2 and 3 wt% Sn-doped ZnO were successfully synthesized by an ultrasonic solution method at 80 ^{o}C for 3 h. In this research, XRD patterns were used to identify the hexagonal wurtzite ZnO phase. Uniform flower-like nanostructures were composed of different oriented petals, each of which was directly grown out of crystalline cores, characterized by electron microscopy. The UV-visible absorption of the 1–3 wt% Sn-doped ZnO exhibited red-shift broad absorption bands from ultraviolet for pure ZnO to visible sunlight by doping element residing in ZnO crystal.

1.5 References

1. Bae SY, Na CW, Kang JH, Park J. J Phys Chem B 2005;109:2526–31.
2. Deng R, Zhang XT, Zhang E, Liang Y, Liu Z, Xu HY, Hark SK. J Phys Chem C 2007;111:13013–5.
3. Qu X, Iü S, Bai L, Meng Q, Jia D. Physica B 2012;407:268–70.
4. Caglar Y, Aksoy S, Ilican S, Caglar M. Superlatt Microst 2009;46:469–75.
5. Sheini FJ, More MA, Jadkar SR, Patil KR, Pillai YK, Joag DS. J Phys Chem C 2010;114:3843–9.
6. Navale SC, Mulla IS. Mater Sci Eng C 2009;29:1317–20.
7. Ye N, Qi J, Qi Z, Zhang X, Yang Y, Liu J, Zhang Y. J Power Sourc 2010;195:5806–9.
8. Sun JH, Dong SY, Feng JL, Yin XJ, Zhao XC. J Mol Catal A 2011;335:145–50.
9. Kim YS, Tai WP. Appl Surf Sci 2007;253:4911–6.
10. Pál E, Hornok V, Oszkó A, Dékány I. Colloid Surf A 2009;340:1–9.
11. Yousefi R, Jamali-Sheini F, Zak AK, Mahmoudian MR. Ceram Inter 2012;38:6295–301.
12. Tsuji T, Terai Y, Kamarudin MHB, Yoshida K, Fujiwara Y. J Lumin 2012;132:3125–8.
13. Sheini FJ, Joag DS, More MA. Thin Solid Films 2010;519:184–9.
14. Powder Diffract. File, JCPDS-ICDD, 12 Campus Boulevard, Newtown Square, PA 19073-3273, USA (2001).
15. Liu JS, Cao JM, Li ZQ, Ji GB, Zheng MB. Mater Lett 2007;61:4409–11.

Chapter 2
Ultrasonic-assisted synthesis, characterization and optical properties of Sb doped ZnO and their photocatalytic activities

2.1 Introduction

Zinc oxide (ZnO) is a n-type II-VI semiconductor with a wide direct band gap of 3.37 eV and large exciton binding energy of 60 meV [1−5], which is more than other semiconductor materials: ZnSe (22 meV) and GaN (25 meV) [6]. It has interesting applications on nanolasers, piezoelectric nanogenerators, solar cells, gas sensors and photocatalyst, due to its unique optical and electrical properties [1, 2, 4, 7]. However, its electrical and optical properties are not able to completely meet the requirements of constructing high performance semiconducting devices, including the increasing needs for applications nowadays [1, 2, 5]. To enhance these properties, ZnO was frequently doped with some dopants [1, 2, 5] such as Sb [6, 8], Sn [9], In [10, 11], Mn [12] and Ce [13]. Sn doped ZnO shows the highest gas response to ethanol vapor and highest photocatalytic activity toward methyl orange (MO) solution [9]. The 2 % Ce doped ZnO shows an effectively oxidation of cyanide to cyanate [13]. Sb doped ZnO nanoparticles have higher resistance and reflectivity than the undoped one [8].

In this research, a facile and environment-friendly low-temperature route was used to synthesize Sb doped ZnO by ultrasonic-assisted solution method. Phase, morphologies, optical properties and photocatalytic properties of Sb doped ZnO were also studied and discussed in this report.

2.2 Experimental

Sb doped ZnO nanostructures were synthesized by the ultrasonic-assisted solution method using zinc nitrate hexahydrate ($Zn(NO_3)_2{\cdot}6H_2O$), antimony chloride ($SbCl_3$) and ammonium hydroxide (NH_4OH) as starting materials. All the chemicals for this synthesis were purchased from Aldrich Chemical Corporation and used without further purification.

For the typical experimental procedure, 0.01 mol of $Zn(NO_3)_2{\cdot}6H_2O$ and 1−5 % by mole of $SbCl_3$ were dissolved in 100 ml of deionized water. Aqueous solution of 28 %

ammonium hydroxide was dropped in precursor solutions until reaching at the pH of 8.5 with continuous stirring to precipitate Zn^{2+} and Sb^{3+} ions into metal hydroxide compound. Subsequently, the resultant solutions were transferred into sonication bath (35 kHz), and sonicated at 80 ^{o}C for 3 h. In the end, the precipitates were filtered and washed with methanol several times to remove ionic impurities, and finally dried at room temperature.

Crystalline phases of the as-synthesized nanostructured materials were analyzed by an X-ray diffractometer (XRD, Philips X'Pert MPD) with Cu-K_{α} radiation in the 2θ = 15^{o}–75^{o} range. The morphology investigation was carried out by field emission scanning electron microscopy (FE-SEM, JEOL JSM-6335F) and transmission electron microscopy (TEM, JEOL JEM-2010) operating at 35 kV and 200 kV, respectively. The optical properties were studied by a *Perkin Elmer*, Lambda 25 UV-visible spectrometer.

Photocatalytic activity was tested by decolorization of methylene blue (MB) in aqueous solution under UV light. The 150 mg pure ZnO and Sb doped ZnO as photocatalysts were suspended in 150 ml 10^{-5} M MB solutions, and were magnetically stirred for 30 min in the dark environment to establish an adsorption/desorption equilibrium of MB on surfaces of the photocatalysts. After UV irradiating, the concentrations of MB were determined by a UV-visible spectrophotometer (Lambda 25, Perkin Elmer) using a wavelength of 664 nm. The decolorization efficiency (%) was calculated as follows

$$\text{Decolorization efficiency (\%)} = \frac{C_o - C}{C_o} \text{x} 100 \qquad (1)$$

where C_o and C were the initial concentration of MB and the concentration of MB after UV irradiation, respectively.

2.3 Results and Discussion

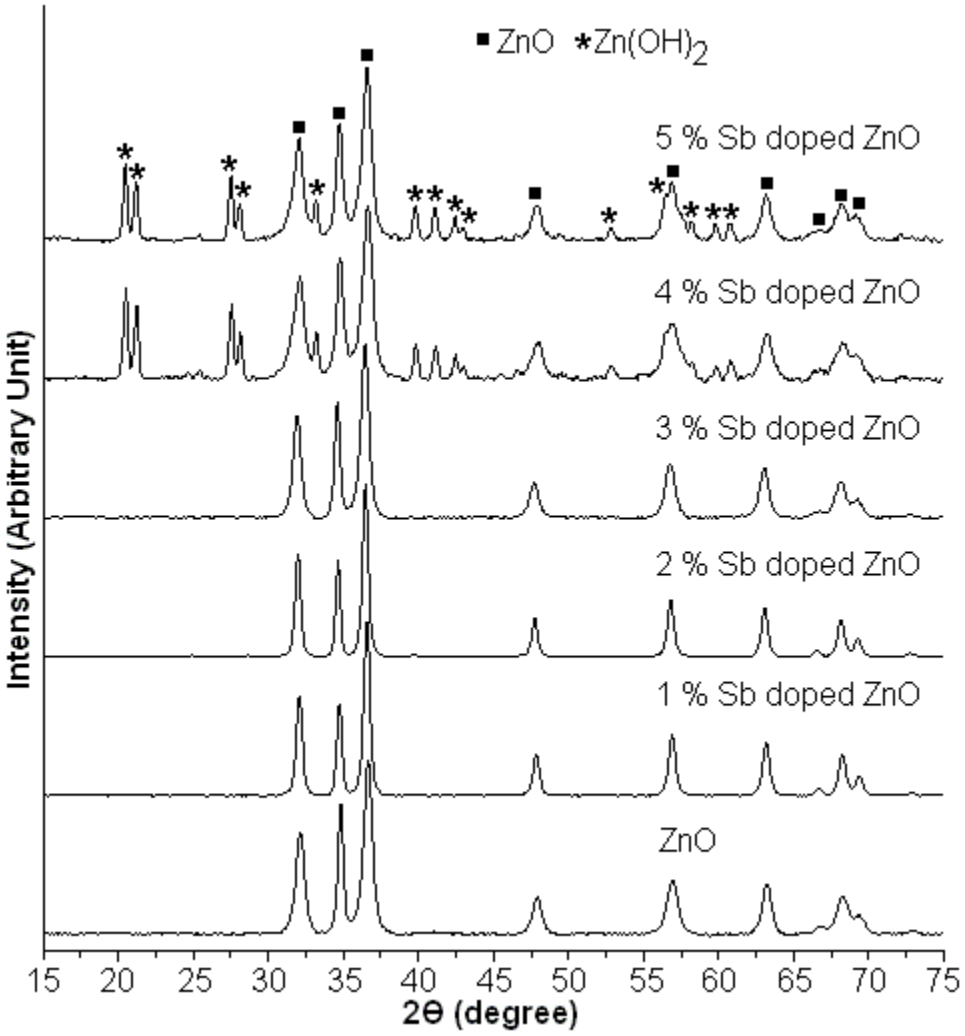

Fig. 2.1. XRD patterns of the products synthesized by ultrasonic-assisted solution method.

The purity and crystalline properties of the as-synthesized ZnO and Sb doped ZnO samples were determined by X-ray diffraction (XRD) as shown in Figure 2.1. The XRD pattern of ZnO without Sb dopant showed diffraction peaks at 2θ = 31.8°, 34.5°, 36.4°, 47.5°, 57.1°, 63.2°, 66.7°, 67.8° and 69.0°, identified to the (100), (002), (101), (102), (110), (103), (200), (112) and (201) planes, respectively of bulk wurtzite hexagonal ZnO structure (JCPDS No. 36-1451) [14]. No observed characteristic peaks corresponding to impurities such as $Zn(OH)_2$ were detected in the pattern, confirming the purity of ZnO

sample. XRD patterns of 1−3 % Sb doped ZnO show the same diffraction pattern as pure wurtzite hexagonal ZnO structure with JCPDS No. 36-1451. No diffraction peaks of impurity phases such as $Zn(OH)_2$, Sb_2O_3 and Sb were detected in these samples, suggesting that Sb^{3+} ions could uniformly substitute into the Zn^{2+} sites or interstitial sites of ZnO lattice by forming $2Sb_{Zn}$ and V_{Zn} [3]. Moreover, the major diffraction peaks shifted slightly towards smaller diffraction angle compared to the pure ZnO phase due to the ionic radius of Sb^{3+} of 0.76 Å [15, 16] > ionic radius of Zn^{2+} of 0.74 Å [16, 17]. Upon increasing the Sb concentration doped in ZnO structure of more than 3 %, mixed phases of $Zn(OH)_2$ and ZnO (JCPDS No. 38-0385 [14] for $Zn(OH)_2$ and No. 36-1451 [14] for ZnO) were detected. The XRD results show that the limited Sb concentration doped in ZnO is 3 wt% in this research.

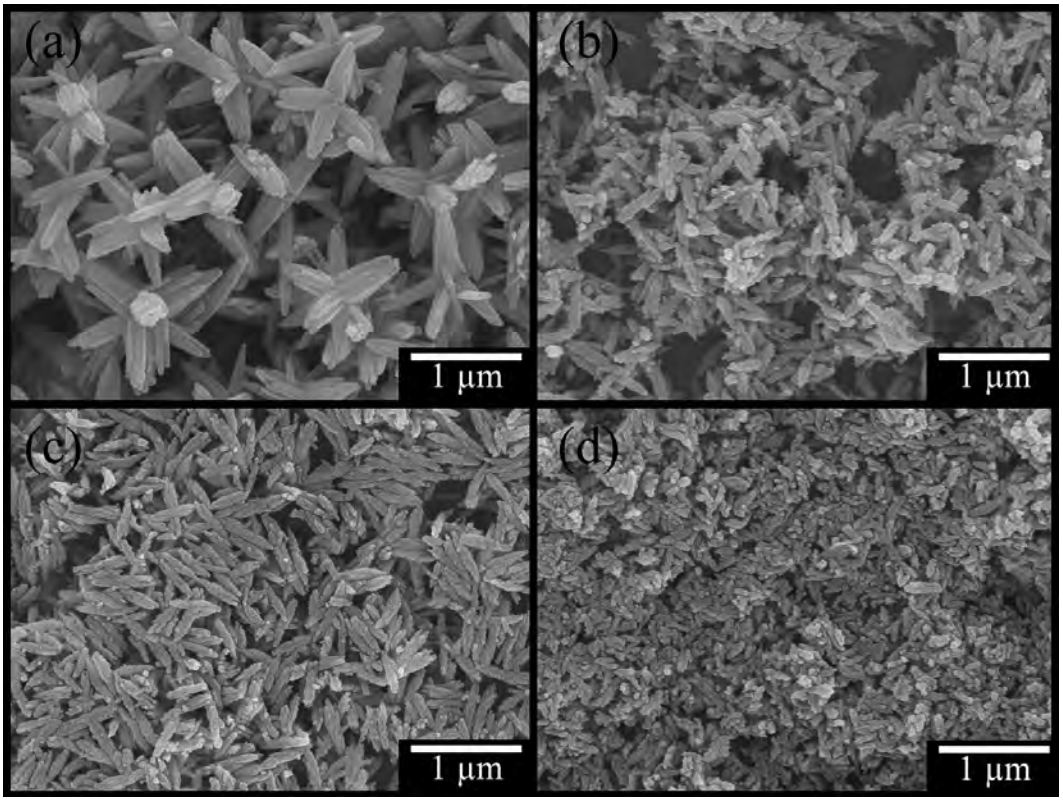

Fig. 2.2. SEM images of (a) pure ZnO, (b) 1 % Sb doped ZnO, (c) 2 % Sb doped ZnO and (d) 3 % Sb doped ZnO samples at low magnification.

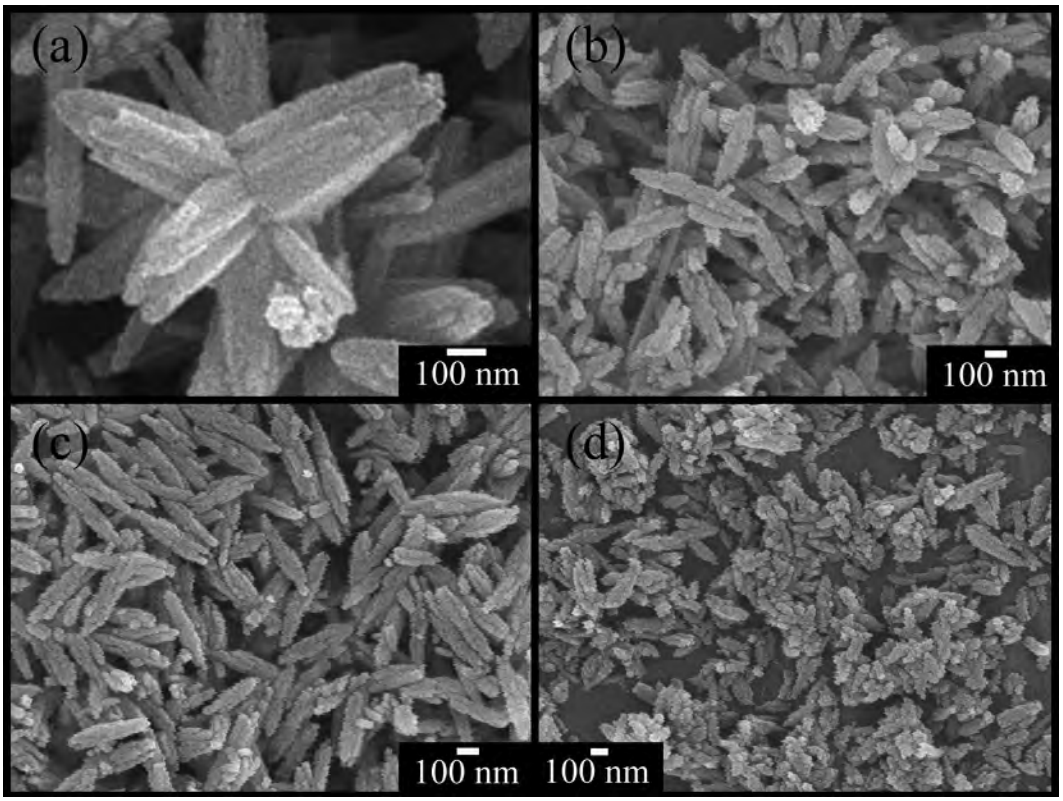

Fig 2.3. SEM images of (a) pure ZnO, (b) 1 % Sb doped ZnO, (c) 2 % Sb doped ZnO and (d) 3 % Sb doped ZnO samples at high magnification.

Figures 2.2 and 2.3 show the FE-SEM images of the as-synthesized 0−3 % Sb doped ZnO products with low and high magnifications. A morphology of pure ZnO as shown in Figure 2.2(a) was well-defined flower-like three-dimension ZnO nanostructures in a large-scale area with diameters in the range of 0.5−1 μm. It should be noted that the flower-like three-dimension ZnO nanostructures were composed of assemblies of nanorods as petals. At high magnification image of the nanorod-built flower-like ZnO nanostructures in Figure 2.3(a), they revealed that each petal was about 300 nm long and 100 nm in diameter. For the SEM images of Sb doped ZnO, the morphologies of rice kernel-like ZnO nanostructures formed instead of flower-like structures. Figures 2.2(b)−(d) and 2.3(b)−(d) show SEM images of 1−3 % Sb doped ZnO prepared by ultrasonic-assisted solution method at low and high magnifications. They show the rice kernel-like ZnO nanorods in the range of 300−400 nm long. However, no flower-like structures were detected in the Sb doped ZnO samples. At high magnification, the

products were composed of assembled nanorods to build rice kernel-like ZnO nanorods. These different morphologies of ZnO and 1−3 % Sb doped ZnO can be explained in terms of a thermodynamic barrier arising from the Sb^{3+} dopant that slowed down the nucleation and inhibited the further growth of Sb doped ZnO crystals [18].

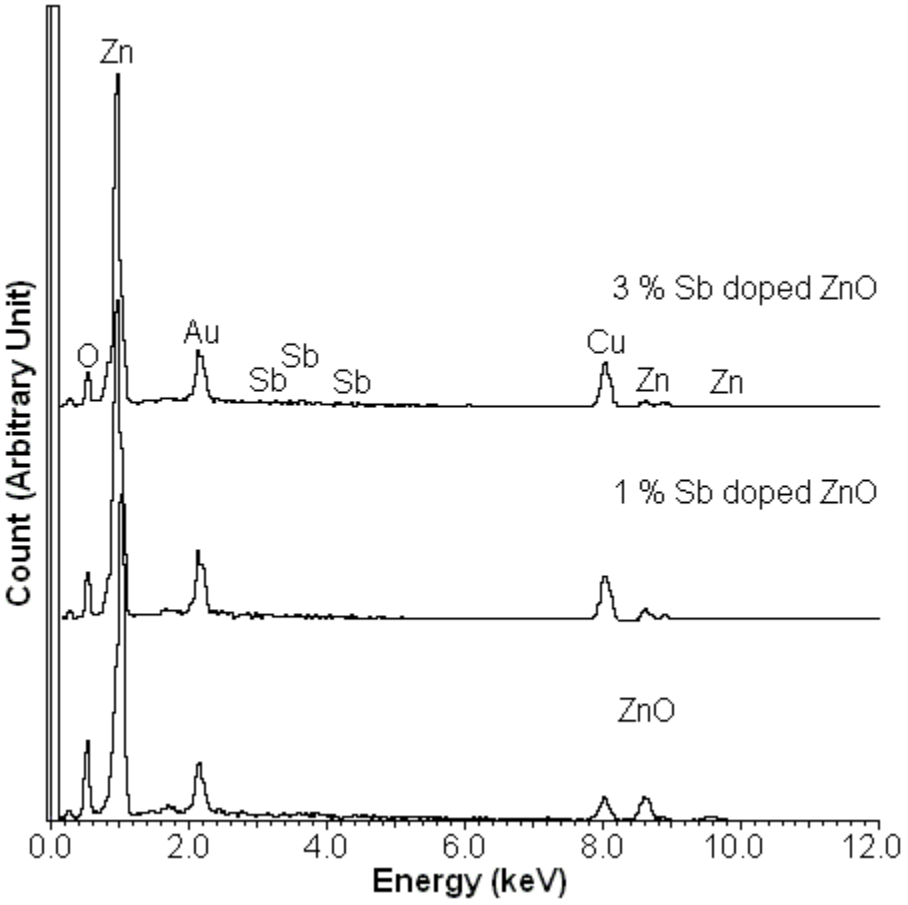

Fig. 2.4. EDX spectra of the products synthesized by ultrasonic-assisted solution method.

Chemical composition of the as-synthesized products was observed using EDX analysis. Figures 2.4 and 2.5 show the typical EDX spectra of 0−3 % Sb doped ZnO and EDX mapping of 3 % Sb doped ZnO. EDX spectra show that the products consisted of zinc and oxygen for pure ZnO; and zinc, oxygen and antimony atoms for 1−3 % Sb doped ZnO. Intense peaks of Cu and Au were also detected in the spectra due to the Cu stubs and sputtered Au. No detection of other impurities in the products, indicating that they were very high purity. Figure 2.5 shows selected area elemental mapping of 3 % Sb

doped ZnO. The mapping was mainly composed of Zn, O and Sb elements. The Sb element was uniformly diffusive in ZnO lattice.

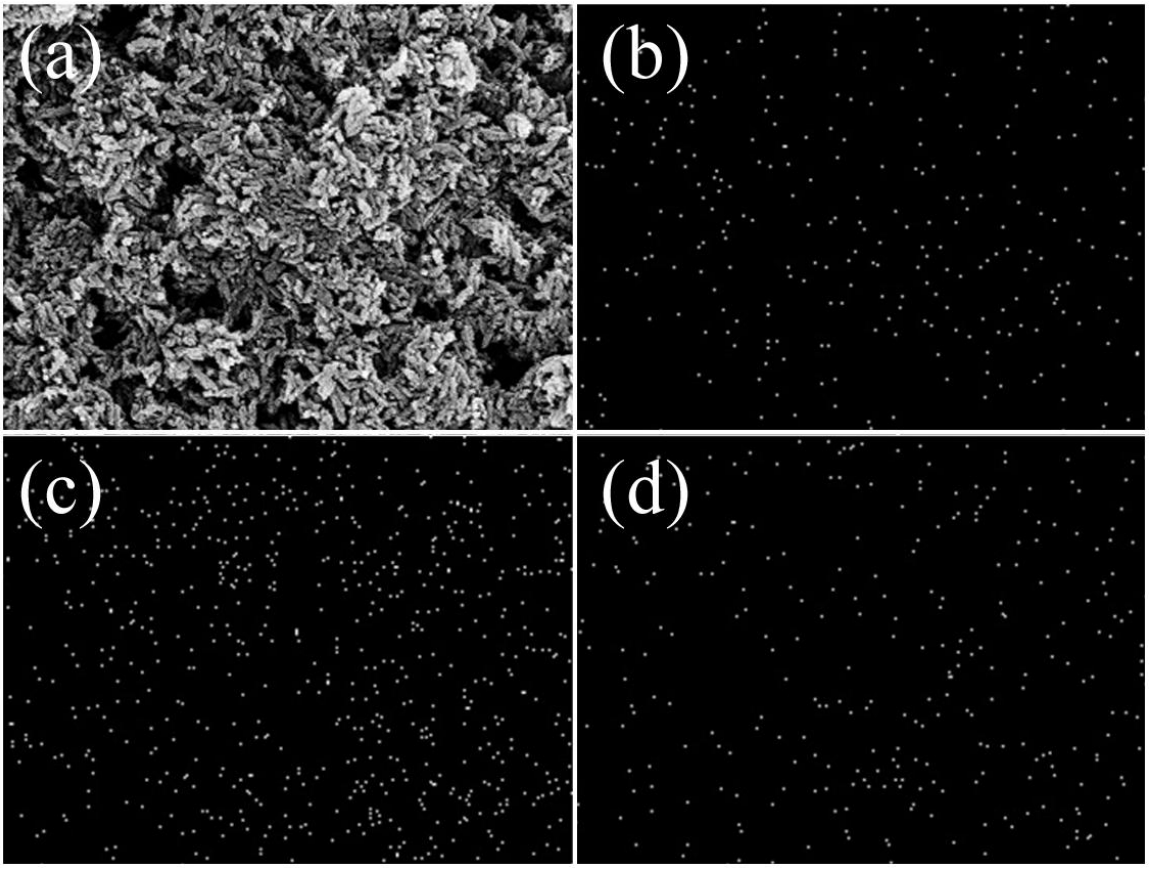

Fig. 2.5. EDX mapping of 3 % Sb doped ZnO sample.

Figure 2.6(a) shows a bright-field TEM image of the as-synthesized ZnO sample. It indicates the detail morphology of the ZnO product with flower-like shape. As shown in Figure 2.6(b), it can be clearly seen that the detail shape of some petals of flower-like ZnO product was composed of many clusters ZnO nanorods. These nanorods were in contact each other as bundles, growing outwardly by forming flower-like structures. The shape of the product appears as flowers with several symmetric petals. It indicated that every bundle was composed of closely packed nanorods with average diameters of around 150 nm. By performing on the individual petal (Figure 2.6(c)), the selected area electron diffraction (SAED) pattern as shown in Figure 2.6(d) indicates that the single

petal is single crystal of hexagonal ZnO phase. The individual petal was also confirmed that the nanorods grow along the [0001] direction.

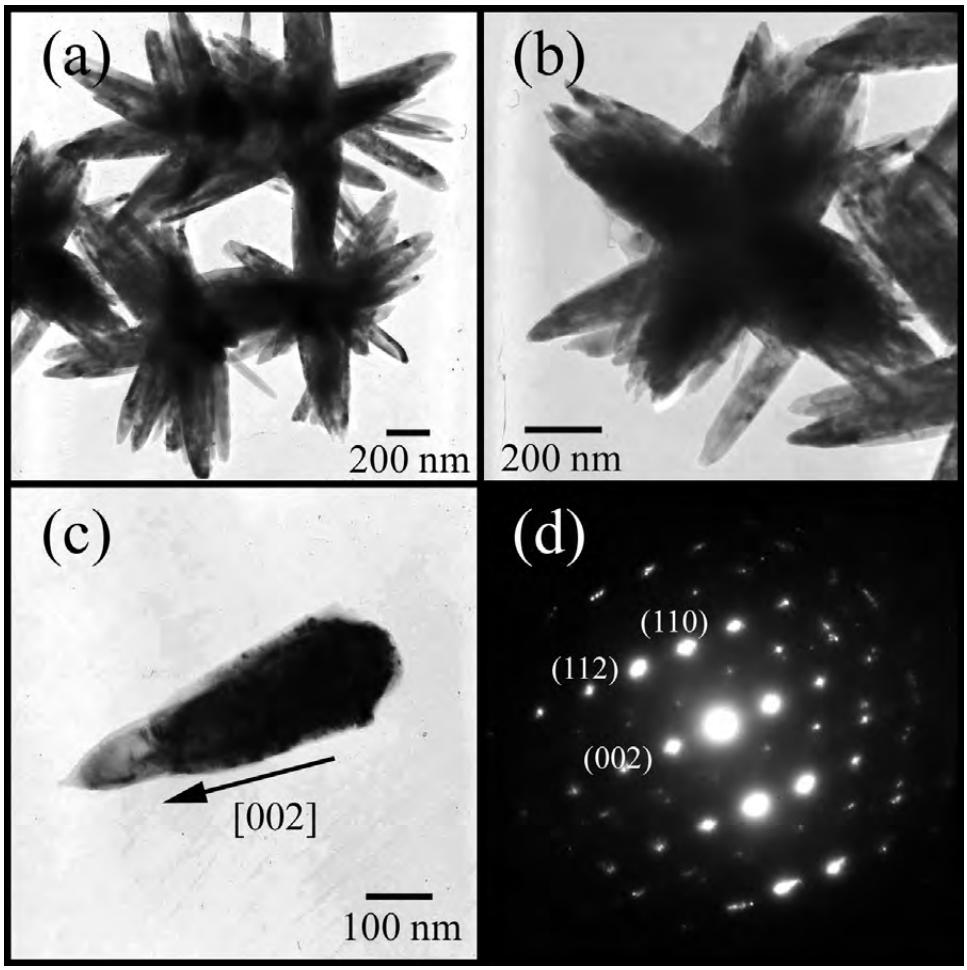

Fig. 2.6. TEM images and SAED pattern of flower-like ZnO structure.

Regarding the formation of flower-like ZnO, it can be explained by manipulating the growth kinetics. In the present case, the contributing growth-driving force for ZnO crystals is the concentration of ZnO_2^{2-} monomers. In the reaction solution containing $Zn(NO_3)_2$ and NH_4OH, the high reactant concentrations led to the burst of initial homogeneous nucleation, and the supersaturated ZnO nuclei aggregated together in groups. As the reaction proceeded, concentration of the ZnO_2^{2-} monomers became lower. Some active sites on the surface of the initially formed ZnO aggregates grew along the oriented direction as the chemical environment constantly provided reactants. The

preferential growth along the [0001] direction due to the intrinsic anisotropy in its growth rate (ν) with ν[0001] > > ν[01-10] > ν[000-1] [7, 19]. The structure of ZnO single crystal can be described as a number of alternating planes of coordinated O^{2-} and Zn^{2+} ions. The oppositely charged ions are made of the positively charged Zn-(0001) and negatively charged O-(0001) polar surfaces. Following the decrease of the concentration of ZnO_2^{2-} monomers due to the initial fast nucleation of ZnO, the absorption of OH^- on the positively charged Zn-(0001) plane dominated the ZnO_2^{2-} growth units. Therefore, the superfluous OH^- ions stabilized the surface charge and the structure of Zn-(0001) face to some degree, allowing the fast growth along the [0001] direction, leading to the formation of flower-like ZnO nanostructure [7, 20−22].

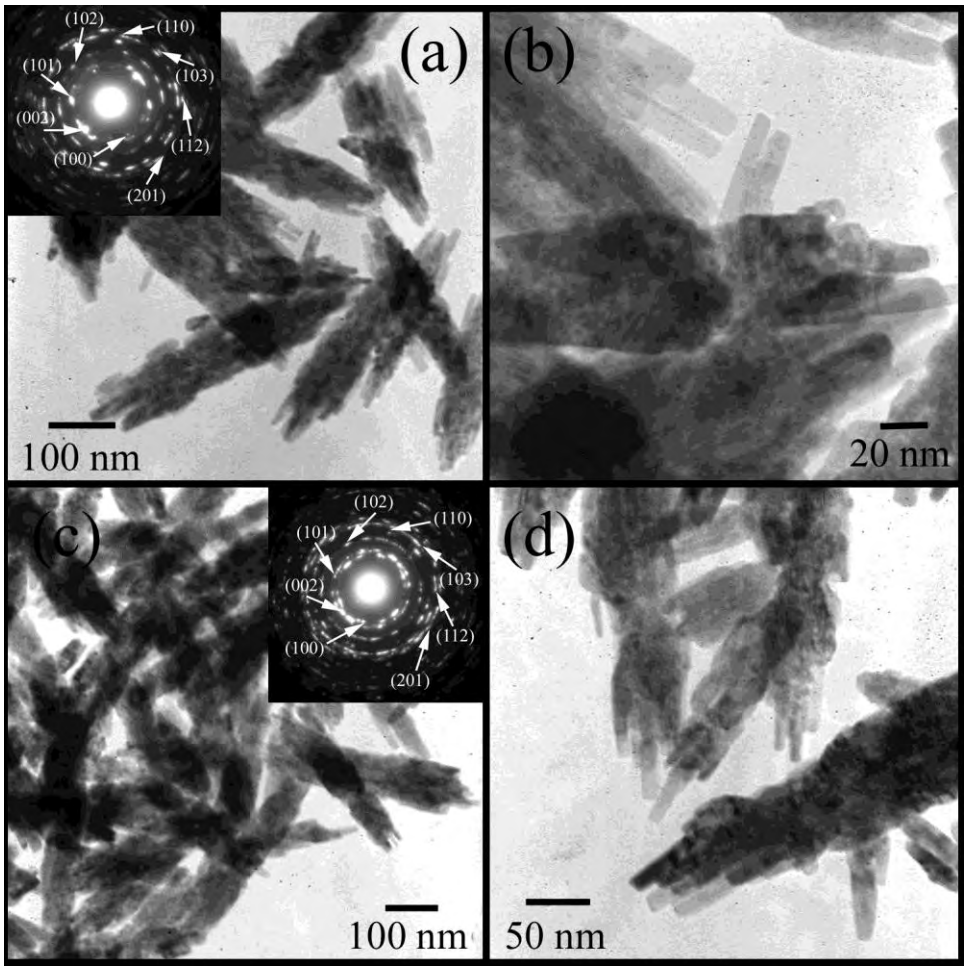

Fig. 2.7. TEM images and SAED patterns of (a and b) 1 % Sb doped ZnO and (c and d) 3 % Sb doped ZnO samples.

Figure 2.7 shows the typical TEM images of 1 % and 3 % Sb doped ZnO nanostructures. It is apparent that 1 % Sb doped ZnO exhibits well-defined rice kernel-like colonies with an average size of 300−400 nm. The nanorods serving as building blocks were tightly packed as colonies of rice kernel-like shaped particles. They can be concluded that the rice kernel-like ZnO colonies formed from the attachment of ZnO nanorods. The magnified TEM image in Figure 2.7(b) shows the detail colonies of rice kernel-like ZnO. The colonies of rice kernels were composed of densely arrayed nanorods with diameter of about 10 nm. While the colonies of the 3 % Sb doped ZnO nanocrystallites as shown in Figure 2.7(c), they present the rice kernel-like colonies of many closely packed nanorods of about 90 nm in diameter and 1.2 μm in length similar to 1 % Sb doped ZnO sample. It also shows that the ends of the nanorods have relatively smaller diameters compared to that of the middle parts. The enlarged TEM image of 3 % Sb doped ZnO sample as shown in Figure 2.7(d) shows the colonies of rice kernel-like ZnO particles with very rough surface. It is noteworthy that the rice kernel-like structure was sufficiently stable, which cannot be destroyed even after ultrasonication for a long time. The insets of Figures 2.7(a) and 2.7(c) show the SAED pattern taken from their corresponding rice kernel-like Sb-doped ZnO samples. The diffraction patterns were composed of a number of bright spots arranged in concentric rings, with the calculated lattice planes obtained from the diameters of the diffraction rings. For the present research, the products were polycrystalline in nature. They were the (100), (002), (101), (102), (110), (103), (112) and (201) planes which were in accordance with those of the JCPDS database for hexagonal ZnO phase.

The optical properties of as-synthesized 0−3 % Sb doped ZnO samples were studied by UV-visible absorption as shown in Figure 2.8. The spectrum of pure phase ZnO sample exhibits a broad absorption band at around 373 nm, blue shift relative to 380 nm of bulk ZnO [23]. However, the spectra of 1 %, 2 % and 3 % Sb doped ZnO samples exhibit sharp bands at 356 nm, 350 nm and 343 nm, respectively. It should be noted that the absorption peaks became sharper. They were blue-shift from 373 nm of pure ZnO sample to 343 nm of 3 % Sb doped ZnO sample. The band gaps were calculated by the equation of $E_g = 1240/\lambda$ [24, 25]. They are 3.32 eV, 3.48 eV, 3.54 eV and 3.61 eV for ZnO, 1 % Sb doped ZnO, 2 % Sb doped ZnO and 3 % Sb doped ZnO, respectively. These

can be explained by the decreasing in size of the particles and consequently the increasing band gap between the valence and conduction bands. A blue shift of the absorption peak in the UV-visible spectra of these samples was successfully and clearly observed.

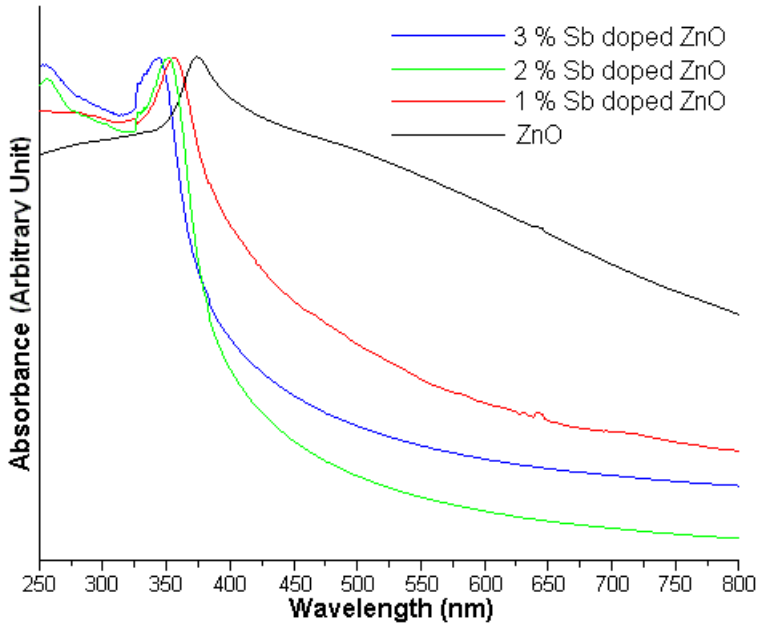

Fig. 2.8. UV-visible spectra of as-synthesized 0−3 % Sb doped ZnO samples.

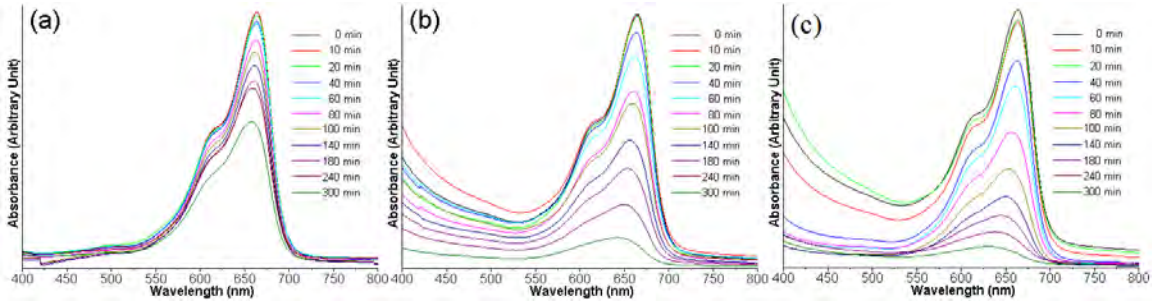

Fig 2.9. UV-visible absorption of MB solutions containing (a) ZnO, (b) 1 % Sb doped ZnO and (c) 3 % Sb doped ZnO.

Upon the illumination of UV light, ZnO can transform the photonic energy into chemical energy, in a similar way for the synthesis or the decomposition of organic materials. Its remarkable oxidation reduction capability, high chemical stability and

harmless characteristics, are most commonly applied in pollutant removal and disinfectants. When the ZnO samples are illuminated by ultraviolet of wavelength less than 400 nm, electrons of the valence band were excited by the photonic energy of the ultraviolet to the conduction band. At the same time, the valence band created electronic holes carrying positive electricity. These holes reacted with the absorbed O_2 or H_2O to create $OH^{\bullet}$ free radicals, which further generated the reaction such as disinfection or deodorization [26]. Figure 2.9(a) shows the UV-visible absorption spectral change of MB during the photocatalytic degradation in the presence of ZnO under UV light over the wavelength range of 400−800 nm. The intensity of main absorption peaks of the MB solutions at approximately 664 nm decreases continuously with the length of UV irradiation time. It indicates that MB molecules could be degraded in the presence of ZnO. The photocatalytic mechanism of ZnO is as follows:

$$ZnO + h\nu \rightarrow ZnO(e_{CB}^{-} + h_{VB}^{+}) \quad (2)$$

$$H_2O + h_{VB}^{+} \rightarrow H^{+} + OH^{\bullet} \quad (3)$$

$$dye + OH^{\bullet} \rightarrow \text{oxidation products} \quad (4)$$

where h_{VB}^{+} and e_{CB}^{-} are the electron vacancies in the valence band and the photogenerated electrons in the conduction band, respectively. The conduction-band electrons and valence-band holes are generated on the surfaces of ZnO nanostructures when they are illuminated by UV light with energy greater than the band gap. Holes react with water molecules adhering to the surfaces of ZnO nanostructures to form highly reactive hydroxyl radicals ($OH^{\bullet}$) which have a powerful oxidation ability to degrade organic dye [7]. Figures 2.9(b) and 2.9(c) show the UV-visible absorption spectra of the aqueous solutions of MB with 1 % Sb doped ZnO and 3 % Sb doped ZnO samples as photocatalysts and illuminated to UV light for different time intervals. The characteristic absorption of MB at 664 nm decreases rapidly with the prolonging time, and almost disappear after about 300 min. Further exposure leads to no absorption peak in the whole spectrum, indicating the almost none of the MB remain. These photocatalysis results clearly demonstrate that Sb doped ZnO exhibited higher photocatalytic activity as compared with ZnO sample.

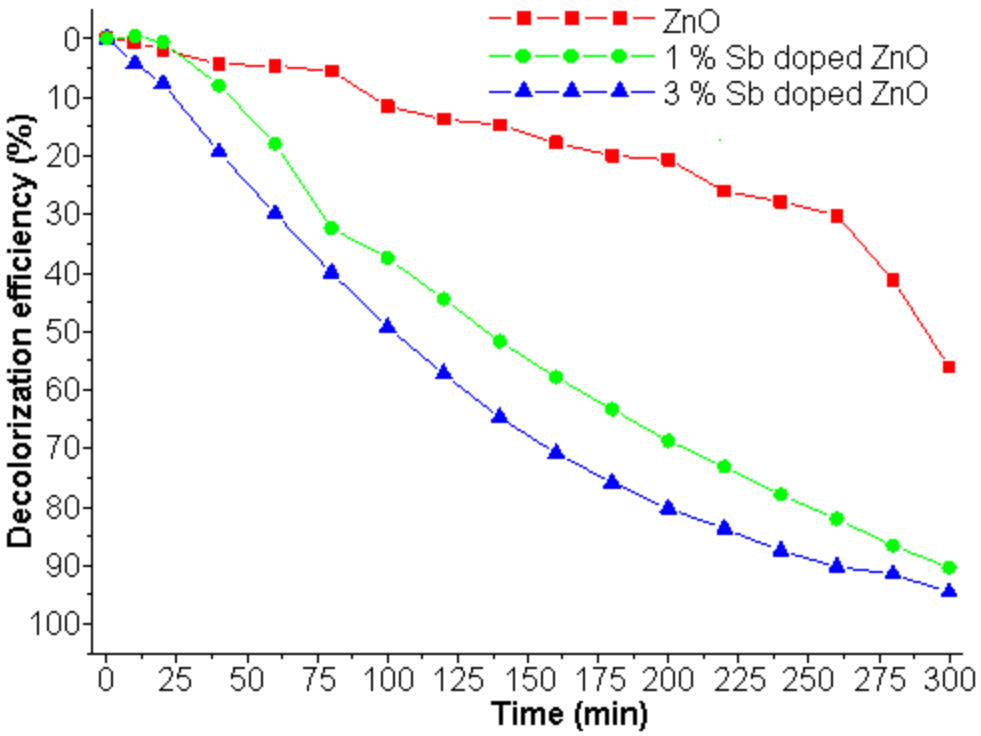

Fig. 2.10. Decolorization efficiencies of ZnO with and without Sb doping.

Figure 2.10 shows MB degradation efficiency of the as-synthesized ZnO and Sb doped ZnO samples. The Sb doped ZnO samples exhibit much higher photocatalytic activities than that of the pure ZnO one. It took only 102 min for 3 % Sb doped ZnO and 134 min for 1 % Sb doped ZnO to decolorize 50% of MB while pure ZnO took more than 275 min to decolorize the same amount of MB. This faster degradation rate of MB under UV irradiation using Sb doped ZnO is attributed to the increase in defect sites caused by Sb^{3+} doping, leading to an enhanced optical absorption in the UV region. After 300 min irradiation, the values of degradation efficiency are 56, 90 and 95 % for pure ZnO, 1 % Sb doped ZnO and 3 % Sb doped ZnO, respectively. This clearly demonstrates that ZnO doped with Sb^{3+} degrades MB more efficiently than undoped ZnO. In this research, the 3 % Sb doped ZnO shows the highest photocatalytic activity. Under illumination with UV light, Sb doped ZnO generates electron–hole pairs at the tail states of conduction and valence bands. The generated electrons diffused to the adsorbed MB molecules on the surface of Sb doped ZnO. The excited electrons from the photocatalyst conduction band migrated into the molecular structure of MB and by forming the conjugated system which

then led to the complete decomposition of MB. Holes at the valence band generated $OH^{\bullet}$ via reaction with water or OH^{-}, might be used for oxidation of other organic compounds.

The photocatalytic properties of as-synthesized photocatalysts were evaluated by measuring the absorption intensity of MB at 664 nm after UV irradiation at different lengths of time. Both of these photodegradation reactions were determined by pseudo-first-order reactions [27−30]. The reaction rate constants of MB degradation were calculated for ZnO, 1 % Sb doped ZnO and 3 % Sb doped ZnO are 1.47×10^{-3}, 6.30×10^{-3} and 8.65×10^{-3} min^{-1}, respectively. This clearly demonstrates that ZnO doped with antimony can be used as a potential photocatalyst illuminated with UV light.

2.4 Conclusions

Ultrasonic-assisted synthesis of Sb doped ZnO at room temperature has been introduced. XRD results showed the formation of wurtzite ZnO and the upper bound of 3 wt% doped Sb. No other phases were detected. The amount of antimony added shows a profound effect on morphology which changed from flower-like of nanorods for ZnO to rice kernel-like for Sb doped ZnO. As-synthesized doped and undoped ZnO crystals were tested and compared for their photocatalytic activities by decolorization of MB under UV light. It was clear that 3 % Sb doped ZnO showed the highest photocatalytic activity toward the MB solution.

2.5 References

1. W.W. Zhong, F.M. Liu, L.G. Cai, X.Q. Liu and Y. Li, Applied Surface Science, 257 (2011) 9318– 9322.
2. D.W. Zeng, C.S. Xie, B.L. Zhu, W.L. Song and A.H. WangMaterials Science and Engineering B, 104 (2003) 68–72.
3. X. Fang, J. Li, D. Zhao, B. Li, Z. Zhang, D. Shen, X. Wang and Z. Wei, Thin Solid Films, 518 (2010) 5687–5689.
4. C.H. Zang, J.F. Su, B. Wang, D.M. Zhang and Y.S. Zhang, , Journal of Luminescence, 131 (2011) 1817–1820.
5. W.W. Zhong, F.M. Liu and W.P. Chen, Journal of Alloys and Compounds, 531 (2012) 59–63.

6. S.H. Kim, A. Umar, Y.K. Park, J.H. Kim, E.W. Lee and Y.B. Hahn, Journal of Alloys and Compounds, 479 (2009) 290–293.
7. B. Li and Y. Wang, Journal of Physical Chemistry C, 114 (2010) 890–896.
8. D.W. Zeng, C.S. Xie, B.L. Zhu, R. Jiang, X. Chen, W.L. Song, J.B. Wang and J. Shi, Journal of Crystal Growth, 266 (2004) 511–518.
9. X. Jia, H. Fan, M. Afzaal, X. Wu and P. ÓBrien, Journal of Hazardous Materials, 193 (2011) 194–199.
10. E. Pál, V. Hornok, A. Oszkó and I. Dékány, Colloids and Surfaces A: Physicochem. Eng. Aspects, 340 (2009) 1–9.
11. B. Wang, M.J. Callahan, C. Xu, L.O. Bouthillette, N.C. Giles and D.F. Bliss, Journal of Crystal Growth, 304 (2007) 73–79.
12. C. Jing, Y. Jiang, W. Bai, J. Chu and A. Liu, Journal of Magnetism and Magnetic Materials, 322 (2010) 2395–2400.
13. C. Karunakaran, P. Gomathisankar and G. Manikandan, Materials Chemistry and Physics, 123 (2010) 585–594.
14. Powder Diffract. File, JCPDS Internat. Centre Diffract. Data, PA 19073–3273, U.S.A. (2001).
15. M. Dondi, F. Matteucci and G. Cruciani, Journal of Solid state Chemistry, 179 (2006) 233−246.
16. O. Lupan, L. Chow, L.K. Ono, B.R. Cuenya, G. Chai, H. Khallaf, S. Park and A. Schulte, Journal of Physical Chemistry C, 114 (2010) 12401–12408.
17. Y. Yang, J. Qi, Q. Liao, Y. Zhang, L. Tang, and Z. Qin, Journal of Physical Chemistry C, 112 (2008) 17916–17919.
18. P. Li, S. Wang, J. Li and Y. Wei, Journal of Luminescence, 132 (2012) 220–225.
19. R.B. Peterson, C.L. Fields and B.A. Gregg, Langmuir, 20 (2004) 5114−5118.
20. Y. Zeng, T. Zhang, L. Wang, and R. Wang, Journal of Physical Chemistry C, 113 (2009) 3442–3448.
21. Z.L. Wang, Journal of Physics: Conference Series, 26 (2006) 1–6.
22. A. Phuruangrat, T. Thongtem, B. Kuntalue and S. Thongtem, Journal of Ovonic Research, 7 (2011) 107−113.

23. J.S. Liu, J.M. Cao, Z.Q. Li, G.B. Ji and M.B. Zheng, Materials Letters, 61 (2007) 4409–4411.
24. Y. Lei, G. Zhao, M. Liu, Z. Zhang, X. Tong and T. Cao, Journal of Physical Chemistry C, 113 (2009) 19067–19076.
25. H. Li, D. Wang, H. Fan, T. Jiang, X. Li and T. Xie, Nano Research, 4 (2011) 460–469.
26. H. Chang and M.H. Tsai, Reviews on Advanced Materials Science, 18 (2008) 734−743.
27. J. Zhao, L. Wang, X. Yan, Y. Yang, Y. Lei, J. Zhou, Y. Huang, Y. Gu and Y. Zhang, Materials Research Bulletin, 46 (2011) 1207–1210.
28. J.H. Zeng, B.B. Jin and Y.F. Wang, Chemical Physics Letters, 472 (2009) 90–95.
29. R. Jain and S. Sikarwar, International Journal of Physical Sciences, 3 (2008) 299−305.
30. J. Chanathaworn, C. Bunyakan, W. Wiyaratn and J. Chungsiriporn, Songklanakarin Journal of Science and Technology, 34 (2012) 203-210.

Chapter 3

Controlling morphologies and growth mechanism of hexagonal prisms with planar and pyramid tips of ZnO microflowers by microwave radiation

3.1 Introduction

Among semiconducting materials, wurtzite hexagonal ZnO with 3.37 eV direct band gap and 60 meV exciton binding energy is an important functional material as short-wavelength optical devices due to its unique piezoelectricity, pyroelectricity and photocatalysis, including light emitting diodes (LEDs), laser diodes (LDs), transparent conducting electrodes for solar cells, surface acoustic filters, UV lasers and chemical/biological sensors [1–6]. Different morphologies of ZnO structures such as nanorods [3, 4, 5], hexagonal cones [6], hollow spheres [7, 8], flowers [2, 9, 10], nanoparticles [11], dendrites [12], hexagonal disks/plates [13–15] and nanotubes [16–19] have been synthesized both by chemical and physical methods such as sol-gel process [1], hydrothermal process [2, 3, 14], thermal evaporation process [4], ultrasonic-assisted synthesis [7–12], carbothermal reduction [15], plasma-assisted molecular beam epitaxy [18, 19], microwave radiation [20] and chemical vapor deposition [21–23].

In case of physical processes, they perform under relatively harsh conditions, requiring high temperature, low pressure (vacuum) and high efficiency instrument with elaborate design. They are quite difficult to apply for large-scale and industrial production. Practically, chemical syntheses in solutions known as solution methods can be enlarged for large-scale production without using catalysts and additives with better crystalline quality, preferably at low growth temperature. The processes are more convenience, inexpensive and challenged nano- and micro- structured products with morphological control and crystalline evolution.

Generally, conventional heating is an energy transferred process from outside to inside of solutions or from the higher to lower temperature by conduction process. There are must be physical contact between internal surfaces of the reaction vessels and the mixtures containing inside. In case of microwave radiation, it is an increasingly popular method used for the synthesis of materials. Microwave radiation is composed of vibrating electric field that can penetrate the reaction vessels. Molecules, ions and dipoles of the

mixtures containing in the vessels rotate and vibrate in accordance with the vibration of the electric field, and cause a rise in the temperature. Heat is directly transferred to nearby mixtures. Temperature distribution of the entire solution mixtures is homogeneous. The main advantages of microwave-assisted synthesis are uniform heating of reactants. The process can generate localized instantaneous hot spots at reaction sites, consume shorter reaction time, selectively form specific morphology, reduce energy consumption and produce high product yield [24, 25].

In this research, a facile synthesis of flower-like ZnO structures composing of petals of hexagonal prisms and hexagonal pyramid tips by microwave radiation is reported. Phase, morphologies and photocatalytic performance of the products were characterized by a series of techniques. These results show that both of the flower-like ZnO products can be used as superior photocatalysts with high efficiency for decomposing of organic dyes.

3.2 Experiment

All chemicals were purchased from Sigma-Aldrich Corporation and used without further purification. To start the procedure, 0.005 mole zinc nitrate hexahydrate ($Zn(NO_3)_2 \cdot 6H_2O$) and 0.010 mole hexamethylenetetramine (HMT) were dissolved in 100 ml de-ionized water under stirring at room temperature. Subsequently, 3 M sodium hydroxide solution was added to each of the 100 ml solutions until reaching at the pH of 9 and 13. The two solutions with the pH 9 and 13 were transferred in a microwave oven and heated at 180 W for 60 min (96 ^{o}C). At the end of microwaving, white precipitates were synthesized, washed with methanol several times and dried at 80 ^{o}C for 24 h to form two powder products.

The as-synthesized products were characterized by Philips X'Pert MPD X-ray powder diffraction (XRD) using a Cu-K_α radiation at 45 kV and 35 mA with a scanning rate of 0.04 deg/s in the 2θ range from 20 to 60 deg. Fourier transform infrared (FTIR) spectra were recorded on a Perkin Elmer RX FTIR spectrophotometer with KBr as a diluting agent and operated in the range of 400–4,000 cm^{-1} with the resolution of 4 cm^{-1}. Raman spectrometer (HORIBA Jobin Yvon T64000) was operated using 50 mW of 514.5 nm wavelength Ar green laser. SEM images were taken through a scanning electron

microscope (SEM, JEOL JSM-6335F) at 20 kV. TEM images of the products were taken using a JEOL JEM-2010 transmission electron microscope (TEM) with an accelerating voltage of 200 kV. UV-visible absorption was carried out through a quartz cell on a Lambda 25 Perkin Elmer spectrophotometer.

Photocatalytic activities of the as-synthesized products were tested by measuring the degradation of rhodamine B (RhB) in aqueous solutions under UV radiation as light source. Each 0.1 g of photocatalyst was suspended in 75 ml of 2.5 mg/l RhB solution, which was magnetically stirred for 30 min in the dark to establish an adsorption/desorption equilibrium of RhB on surface of each photocatalyst. Then the light was turned on to initiate photocatalytic reaction. The solutions were analyzed by a Lambda 25 Perkin Elmer spectrometer using 450 W of Xe-lamp with 554 nm wavelength. The decolorization efficiency (%) was calculated using the equation:

$$\text{Decolorization efficiency (\%)} = \frac{C_o - C}{C_o} \text{x}100 \qquad (1)$$

where C_o and C are the initial and final concentrations of RhB.

3.3 Results and discussion

Phase of the as-synthesized ZnO products was characterized by XRD as shown in Fig. 3.1. All diffraction peaks at 2θ of 31.81^o, 34.47^o, 36.31^o, 47.61^o and 56.65^o were respectively indexed to the (100), (002), (101), (102) and (110) planes of pure hexagonal wurtzite ZnO structure of the JCPDS database no. 36-1451 [26]. No impurities were detected in these products. The characteristic peaks were high in intensity and narrow spectral width, implying that the products were high degree of crystallinity.

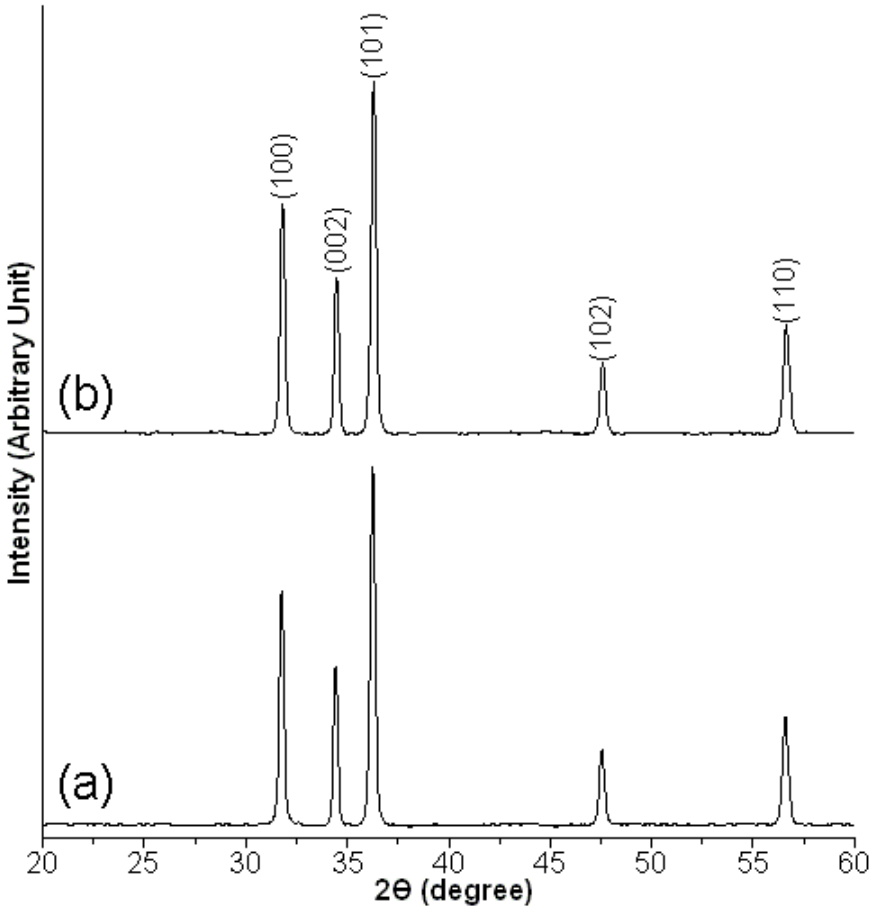

Fig. 3.1 XRD patterns of ZnO synthesized in the solutions containing $Zn(NO_3)_2 \cdot 6H_2O$ and HMT at the pH (a) 9 and (b) 13.

Raman spectra of hexagonal wurtzite ZnO structure belongs to the C_{6v}^4 or $P6_3mc$ space group, with 12 phonon modes and two formula units per primitive cell. Therefore, there are nine optical and three acoustic phonon modes, belonging to three longitudinal-optical (LO), six transverse-optical (TO), one longitudinal-acoustic (LA) and two transverse acoustic (TA) modes. Different symmetries involve the vibrational Raman active appearing in the spectra. Changes in lattice spacing and chemical environment are able to shift their vibrational frequencies. According to group theory prediction, the vibration of optical phonons at the Γ point of Brillouin zone is $\Gamma_{opt} = 1A_1 + 1E_1 + 2E_2$, where A_1 and E_1 are active in both Raman and infrared (IR) and E_2 is active in only Raman. The polar characteristics of the A_1 and E_1 split into LO and TO components due to the macroscopic electric fields associated with optical phonons. Fig. 3.2 shows typical

Raman-scattering spectra with Ar green laser line as the excitation source for the as-synthesized ZnO products at the wavenumber of 200–800 cm^{-1}. Intense peaks at 438 cm^{-1} were specified as the E_{2H} mode, and a very weak peak at 585 cm^{-1} as the E_{1L} mode. The presence of Raman-active optical phonon E_{2H} mode was caused by the wurtzite hexagonal phase of ZnO, and the E_{1L} mode was caused by the structural defects of oxygen vacancies, zinc interstitials, free carriers and impurities. The E_{2L} low frequency mode at approximately 100 cm^{-1} was out of the range of the present analysis. In addition, two very weak peaks at 332 cm^{-1} and 381 cm^{-1} were also detected which indicated as the E_{2H}–E_{2L} multi-phonon and A_{1T} modes, respectively [4, 10, 14, 20, 27].

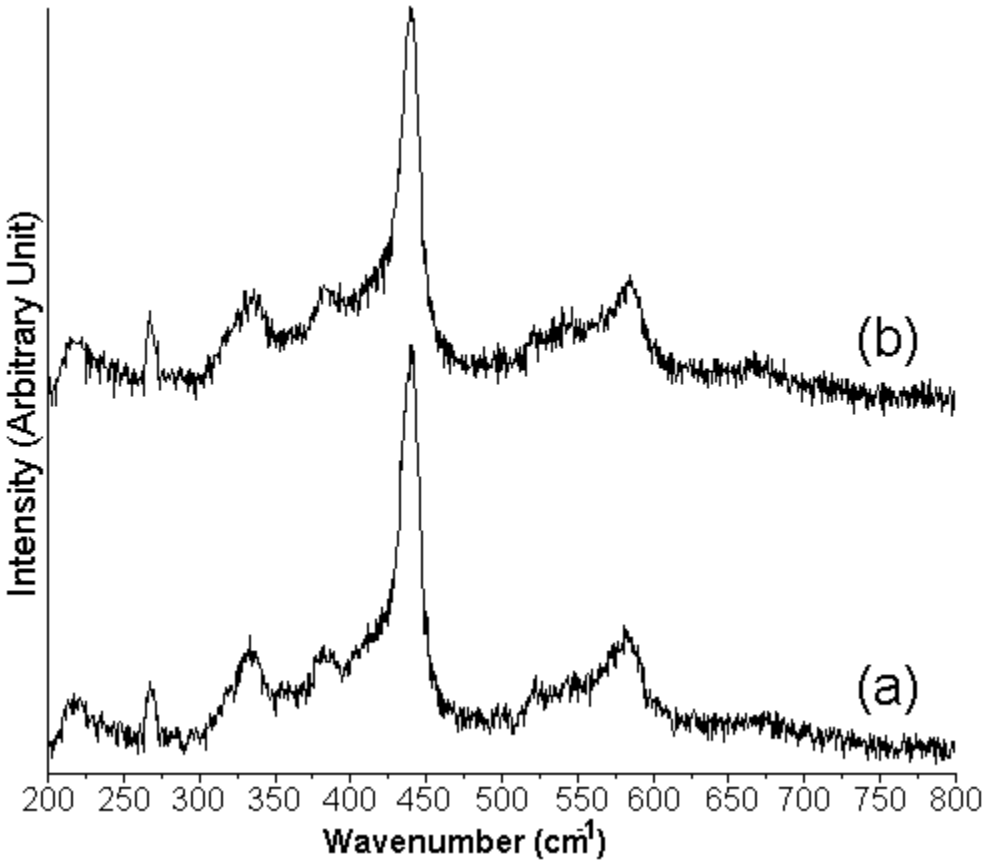

Fig. 3.2 Raman spectra of ZnO synthesized in the solutions containing $Zn(NO_3)_2 \cdot 6H_2O$ and HMT at the pH (a) 9 and (b) 13.

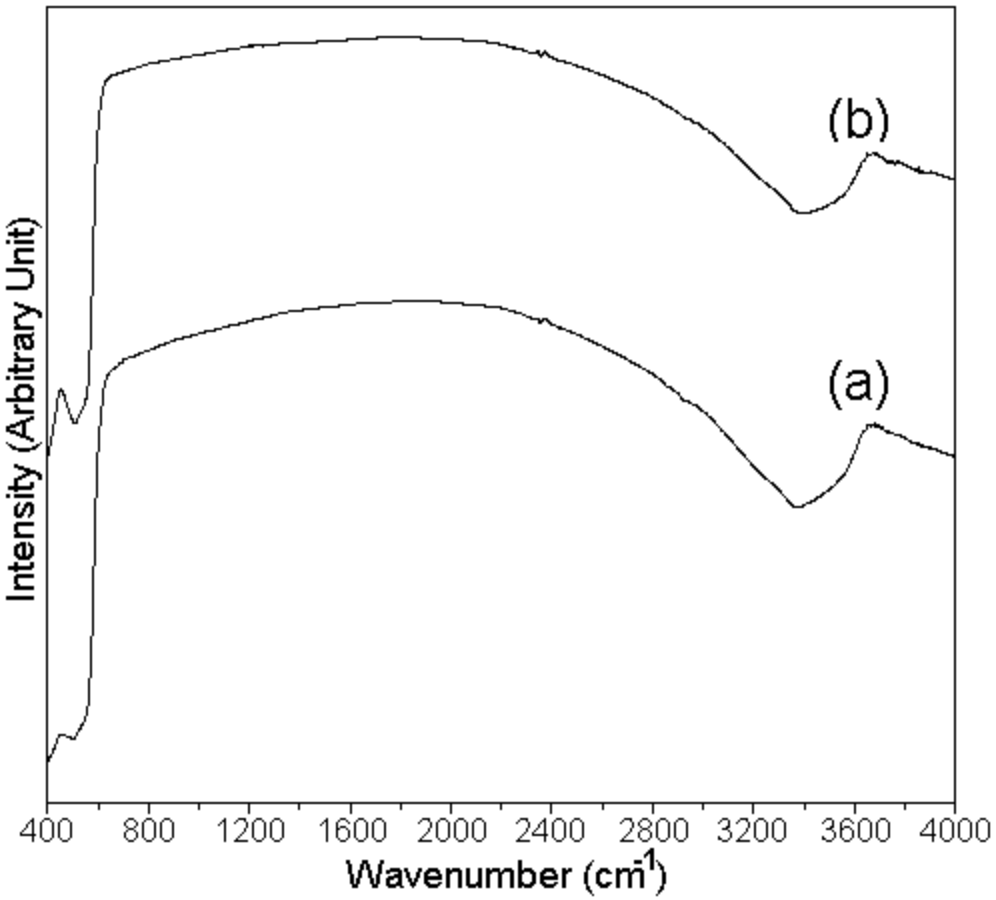

Fig. 3.3 FTIR spectra of ZnO synthesized in the solutions containing $Zn(NO_3)_2 \cdot 6H_2O$ and HMT at the pH (a) 9 and (b) 13.

FTIR spectra of ZnO products diluted by mixing with KBr at the 1:10 ratio for the analysis in range of 400–4,000 cm^{-1} at room temperature are shown in Fig. 3.3. They show absorption band around 521 cm^{-1} and a broad band at 3,200–3,600 cm^{-1}. The absorption at 521 cm^{-1} is a typical characteristic band of wurtzite hexagonal ZnO structure [28, 29]. No other peak was detected, implying that the as-synthesized products were pure ZnO phase. The broad band at 3,200–3,600 cm^{-1} belongs to water absorption on the surface of ZnO products.

ZnO wurtzite crystal structure is able to be described as hexagonal close packing of O and Zn atoms in $P6_3mc$ space group with Zn atoms in tetrahedral sites. There is no center of inversion in the wurtzite structure. Thus an inherent asymmetry along the c-axis is present, which allows the anisotropic growth of the crystal along the [0001] direction.

A typical crystal exhibits a basal polar O (000–1) face and a top tetrahedral corner-exposed polar Zn (0001) face, leading to their difference in reactivity. Zn and O atoms are located in an alternating manner in the (10–10) planes parallel to the c-axis. Structurally, ZnO has three types of rapid growth directions: <2–1–10> (±[2–1–10], ±[–12–10], ±[–1–120]); <01–10> (±[01–10], ±[10–10], ±[1–100]); and ±[0001]. Together with the polar surfaces of atomic termination, ZnO exhibits a wide range of novel structures grown by tuning the growth rate along these directions. One of the most profound factors in determining ZnO morphology involves the relative surface activities of different growth facets under given conditions. Macroscopically, the crystal has different kinetic parameters for different crystalline planes under controlled growth conditions. Following an initial period of nucleation, crystallites will commonly develop into three-dimensional particles with well-defined and low-index crystallographic faces [30–32].

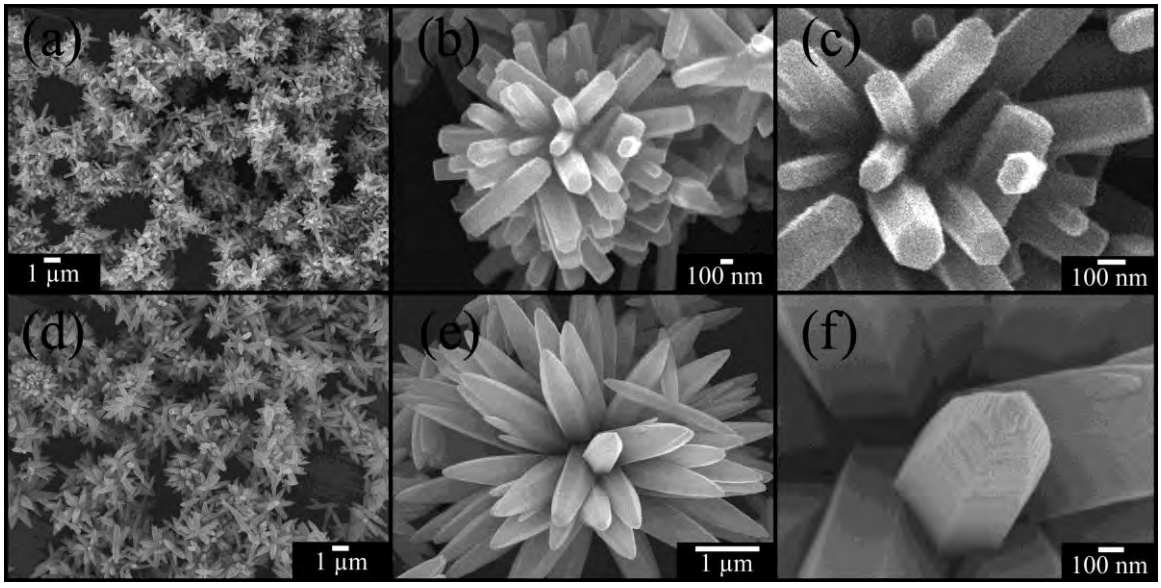

Fig. 3.4 SEM images of ZnO synthesized in the solutions containing $Zn(NO_3)_2 \cdot 6H_2O$ and HMT at the pH (a-c) 9 and (d-f) 13.

The morphologies of the as-synthesized ZnO products were investigated in detail using SEM. At the pH 9, SEM image of Fig. 3.4(a) gives a general view of the product morphology over a large area. The product consists of a large number of microstructured

ZnO flowers with the size of 2–3 μm. For a medium magnification SEM image (Fig. 3.4(b)), the microstructured ZnO flowers were composed of microrods in the shape of hexagonal prisms grown out of ZnO cores. At high magnification, SEM image (Fig. 3.4(c)) reveals that each microrod is a hexagonal-facet prism with smooth planar tip. Each hexagonal prism is 1–2 μm long and 50–130 nm in diameter. Clearly, each microrod formed as solid prism with its tip similar to a hexagon and its six equivalent vertical side walls in the shape of rectangle. Moreover, each of the as-grown microrods contains the (0001) top facet enclosed with six crystallographic planes of (10–10), (01–10), (–1100), (–1010), (0–110) and (1–100) as shown in Fig. 5(a). The exact hexagonal surfaces confirmed the epitaxial growth and therefore the single crystalline nature of the as-grown microrods [31–33]. At the pH of 13, the SEM images are shown in Fig. 3.4(d)–(f). At low magnification, the product is full array of uniform flower-shaped ZnO with the size range of 2–3 μm. For the medium magnification SEM image, the flower-shaped ZnO was composed of a number of petals of perfectly hexagonal prisms with hexagonal pyramid tips. Their lengths and diameters were 1.5 μm and 0.3 μm, respectively. They should be noted that all hexagonal prisms with pyramid tips grew out of the same origin cores to set up flower-shaped morphology. At high magnification, the image shows a hexagonal prism with hexagonal pyramid tip. Each pyramid was composed of six triangles on top forming as the ±{10–11} polar planes, which were able to be inferred from wurtzite ZnO lattice structure. The six ±{10–11} polar planes are (10–11), (1–101), (0–111), (–1011), (–1101) and (01–11) [34]. Assemblies of the microrods were likely to be initiated by long-range electrostatic interaction and short-range chemical bonding, leading to the observed superstructure. The ±{10–11} planes were polar surfaces which could be terminated as zinc or oxygen faces. The electrostatic force can lead to the freestanding microrods with sharp tips on the ±{10–11} planes to be very active [30, 31, 34, 36]. Some microrods attract charged ions such as OH^- in aqueous solution onto the polar pyramid faces and the remains attract others onto the opposite polar planes. In the end, ZnO hexagonal prisms with hexagonal pyramid tips were produced as shown in Fig. 3.5(b).

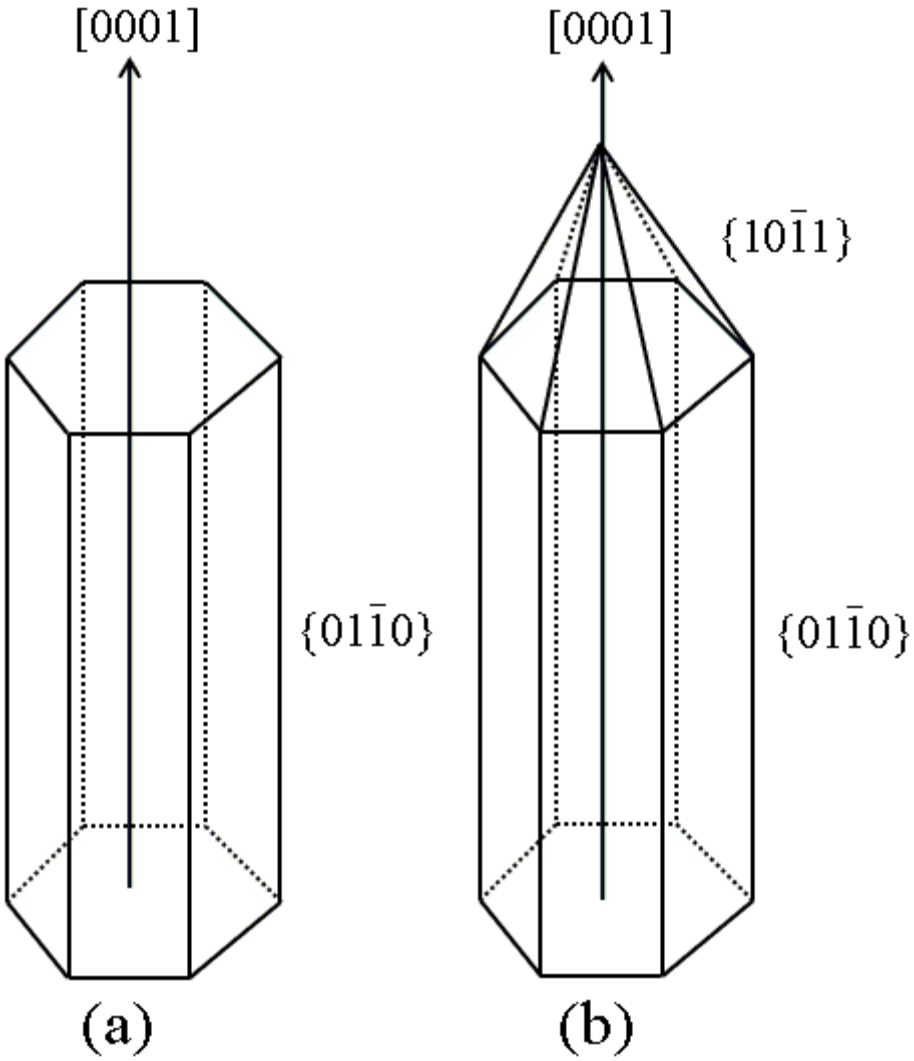

Fig. 3.5 Schematic illustration of the growth models for hexagonal prisms with (a) planar and (b) hexagonal pyramid tips.

Fig. 3.6 shows TEM images and SAED patterns of the as-synthesized hexagonal prism flower-shaped ZnO microstructure. An individual flower-like ZnO microstructure with perfect geometry was the assembly of uniform hexagonal prism microrods. The flower-like ZnO assemblies consist of well-aligned hexagonal prisms of straight and uniform microrods with 100 nm wide and about 600 nm long, growing along the [0001] direction. SAED patterns of broken hexagonal prism ZnO microrods on the areas of 1 and 2 were characterized. The bright diffraction spots of the SAED patterns indicate that the individual hexagonal prisms of flower-like ZnO microstructure were single crystal. Both

SAED patterns were specified as the (11–20), (11–22) and (0002) planes with the [1–100] direction as zone axis of the hexagonal ZnO phase, in accordance with the above XRD analysis.

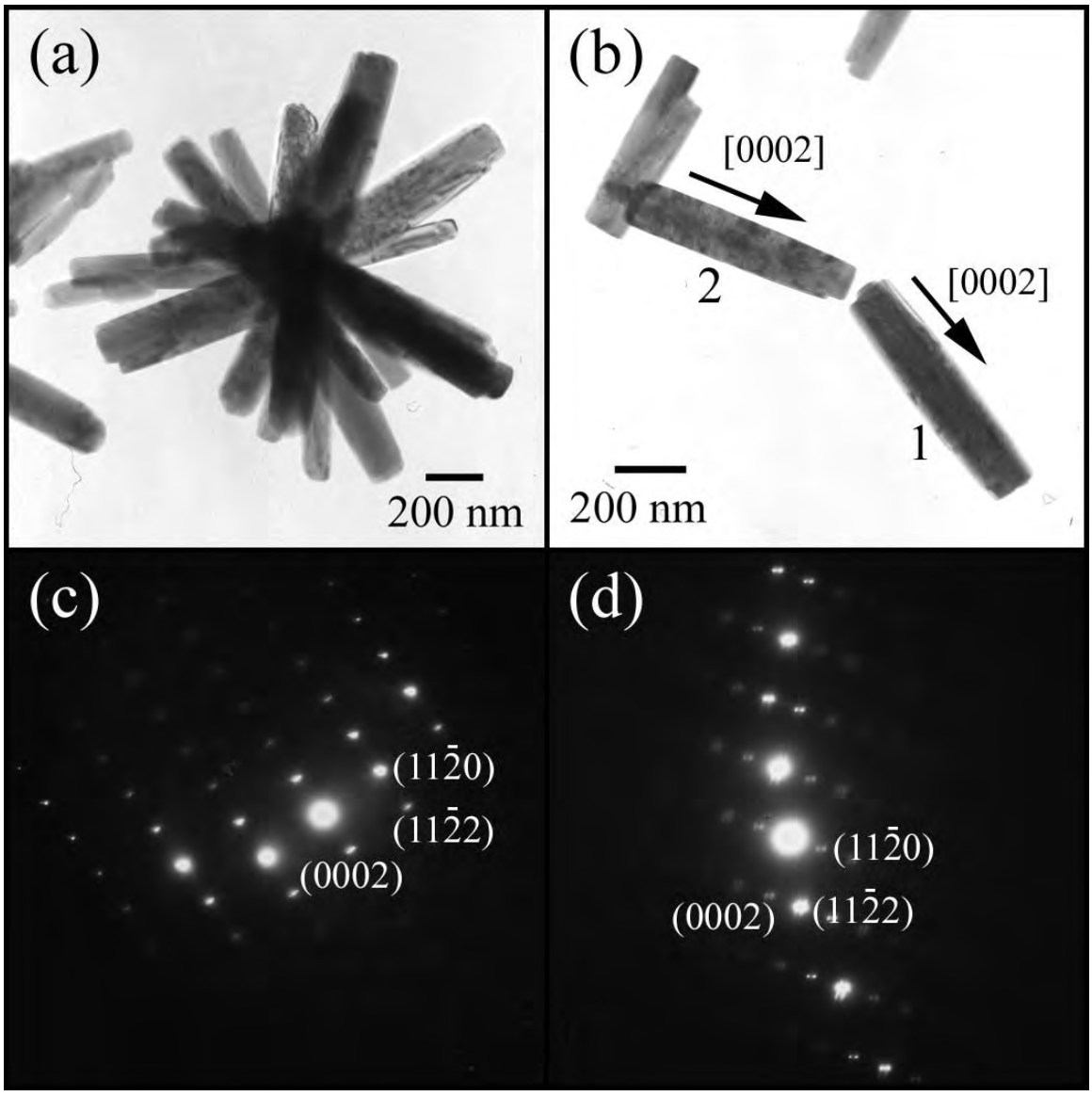

Fig. 3.6 (a, b) TEM images and (c, d) SAED patterns of hexagonal prisms of flower-like ZnO microstructure synthesized in the solution with the pH 9.

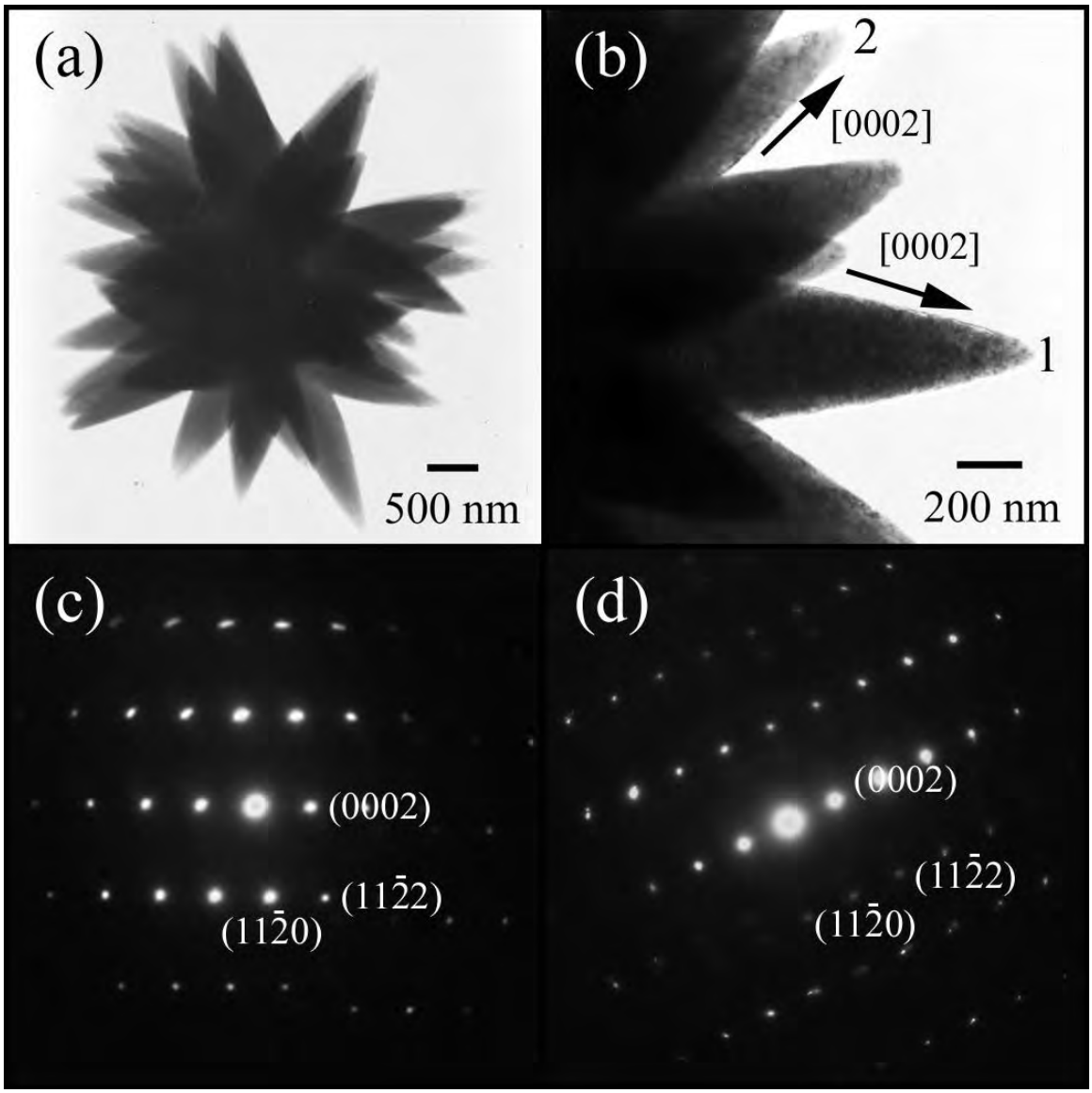

Fig. 3.7 (a, b) TEM images and (c, d) SAED patterns of hexagonal pyramids of flower-like ZnO microstructure synthesized in the solution with the pH 13.

Fig. 3.7 shows TEM images of the hexagonal prisms with sharp tips of ZnO microstructure, in accordance with the above SEM characterization. It should be noted that the flower-shaped ZnO was composed a number of perfectly hexagonal prisms with sharp tips grown out of the same origin core to set up ZnO flower-shaped morphology with its petals of hexagonal prisms with sharp tips. At high magnification, the hexagonal pyramid flower-shaped ZnO microstructure was composed of smooth and clean surfaces of microrod petals with different orientated tips directing in the [0001] direction. Single

crystalline ZnO microrods were also characterized by SAED at the areas of 1 and 2, which show patterns of the symmetrical stripes of bright spots rather than bright spots in circles of the same center. Both patterns were indexed to be hexagonal ZnO with the [−1100] direction as zone axis.

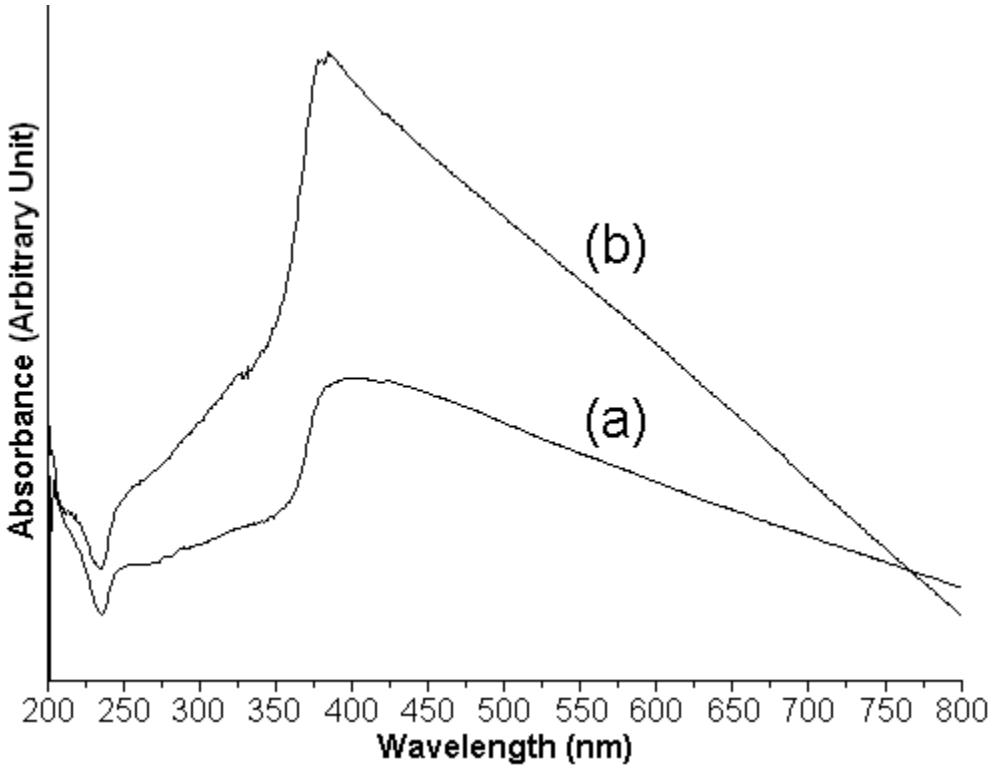

Fig. 3.8 UV-visible absorption of (a) hexagonal prisms and (b) hexagonal pyramids of flower-like ZnO microstructures.

The formation of ZnO microflowers which are composed of petals in the shapes of hexagonal prisms with planar and pyramid tips can be explained by the following. The precipitation of ZnO particles in aqueous solution is rather complex. Generally, the size and morphology of ZnO particles are controlled by the chemical state of Zn^{2+} ions in the solution. Thermodynamic and kinetic factors can play different roles in the precipitation process. The chemical state of Zn^{2+} ions is strongly controlled by the pH of solution and anionic type. By gradual adding of NaOH solution to Zn(II)-salt solution, $Zn(OH)_4^{2-}$ complexes originated at the pH of 9. Precipitation of ZnO from $Zn(OH)_4^{2-}$ complexes can be written by the following reaction

$$Zn^{2+} + 4OH^{-} \rightarrow Zn(OH)_4^{2-} \quad (2)$$

$$Zn(OH)_4^{2-} \rightarrow ZnO + H_2O + 2OH^{-} \quad (3)$$

Due to the fewer nuclei and a large number of growth units, $[Zn(OH)_4]^{2-}$ complexes are able to easily adsorb on different sites of ZnO nanorods (seeds). The positively charged Zn-(0001) surfaces are the most reactive. Thus OH^- ions may stabilize the positive charge of the Zn-(0001) surfaces to some extent, allowing rapid growth along the [0001] direction, leading to the formation of ZnO hexagonal prisms with rod-like crystal. Comparing with ZnO microflowers of hexagonal pyramid tips, $Zn(NO_3)_2 \cdot 6H_2O$ produced predominant aqueous species at higher concentration of NaOH solution with the pH of 13 such as $Zn(OH)_3^{1-}$, $Zn(OH)_4^{2-}$ and ZnO_2^{2-} zincate ions. At high pH, these species are very stable, leading to promote the dissolution of $Zn(OH)_2$ and ZnO at room temperature. The stability of these complexes decreases with increasing in the temperature during microwaving, resulting in the formation of ZnO solid. Growth mechanism of ZnO microflowers with the petals of hexagonal pyramids is able to be understood on the basis of the following reactions and crystalline characteristics of wurtzite ZnO. The structure of ZnO single crystal can be described as a number of alternating surfaces of coordinated O^{2-} and Zn^{2+} with oppositely charged ions, made of Zn rich positive surfaces and oxygen rich negative surfaces, which can attract new ZnO and opposite charged species. Due to the crystalline characteristics of ZnO, growth rates (R) of different surfaces are in sequence as follows: R(0001) > R(−101−1) > R(−1010) > R(−1011) > R(000−1). For the formation of ZnO microflowers with petals of hexagonal pyramids, the polar (0001) and six {10−11} surfaces make up hexagonal pyramids. The bases of hexagonal pyramids consist of end surfaces of O terminated (000−1) and side surfaces of O terminated (10−11), which are all polar surfaces. For wurtzite ZnO crystal, the O terminated (000−1) polar surfaces are generally thought to be inert comparing with the Zn terminated (0001) polar surfaces. During crystalline growth, the polar surfaces with the lowest energy (atoms/ions prefer to reside on the lowest energy level) are the most rapid growth and will be faded away. Thus, growth of the hexagonal pyramids is along the [0001] direction or Zn polarized direction. Possibly, surface energies of polar surfaces are raised up or passivated by oppositely charged ions. At high pH value, a strong electrostatic interaction between the ions and polar surfaces is created, leading to the increase of surface energies

of the (0001) and (10−11) polar surfaces in comparison with those of other crystalline surfaces. Thus, growth rates of these polar surfaces are slow down and the polar surfaces appear as external surfaces on sharp tips of the hexagonal prisms with pyramid tips [28, 36-41].

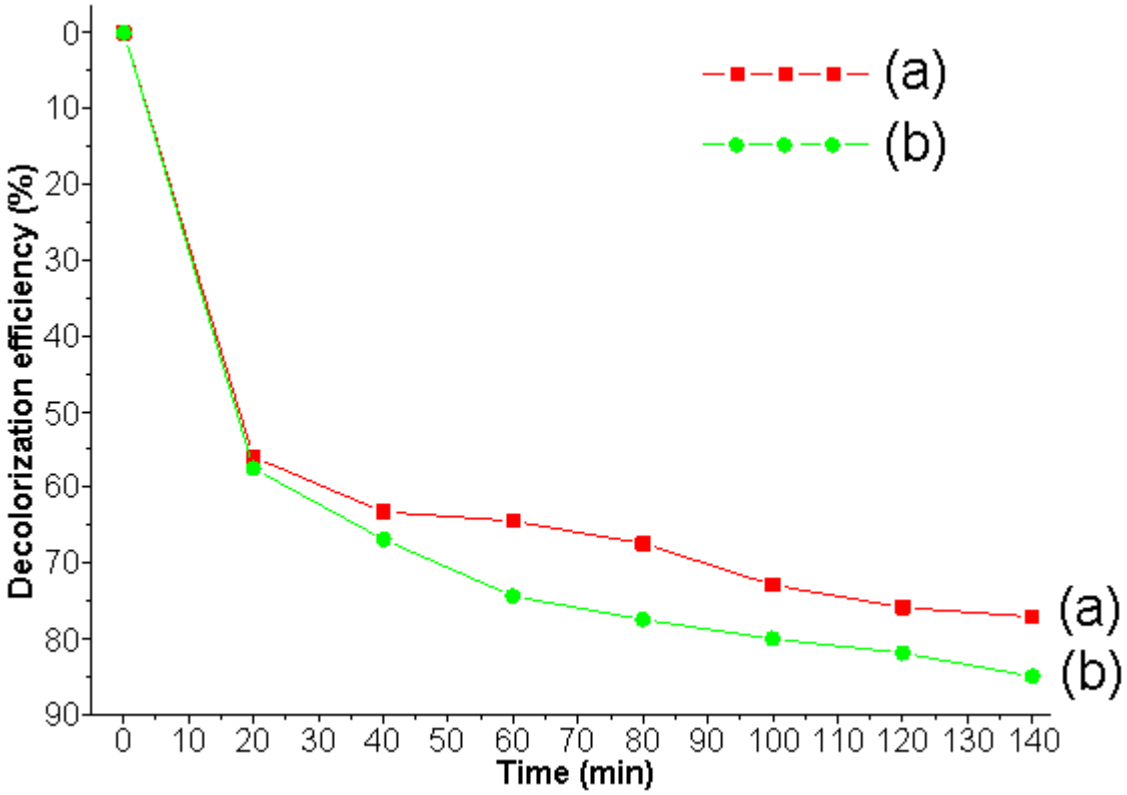

Fig. 3.9 Decolorization efficiency of RhB by (a) hexagonal prisms and (b) hexagonal pyramids of flower-like ZnO microstructures.

ZnO powders were dispersed in an analytical grade ethanol for optical studying. Optical properties of the as-synthesized products were investigated through UV-visible absorption at room temperature as shown in Fig. 3.8. Their absorption spectra are broad over the range of 300–500 nm for flower-like ZnO microstructures of hexagonal prisms with planar tips and strong absorption band in the range of 350–550 nm for flower-like ZnO microstructures of hexagonal pyramids. They are excitonic characters with the absorption peaks at 397 nm with calculated band-gap of 3.12 eV for hexagonal prisms, and 384 nm with calculated band-gap of 3.23 eV for hexagonal pyramids, attributed to

band edge absorption of the wurtzite hexagonal pure ZnO products [35, 36, 42]. These calculated band gaps were a little difference from that of their bulk with E_g = 3.37 eV [43].

In this research, the photocatalytic degradation efficiency of 75 ml of 2.5 mg/l RhB solutions was used to evaluate the photocatalytic activities under UV radiation of Hg lamp. Fig. 3.9 shows the decolorization efficiency of two ZnO microstructures under UV illumination for 140 min. They show that ZnO microstrures were able to decolorize RhB to about 55 % within 18 min. When the time was lengthened to 140 min, the decolorization efficiency of RhB by hexagonal pyramids of flower-like ZnO was 87 % and by hexagonal prisms of flower-like ZnO was 77 %. These results show that the hexagonal pyramids of flower-like ZnO exhibited the highest photocatalytic efficiency which might be attributed to the unique structure to absorb large fraction of UV light. Contrarily, the hexagonal prisms of flower-like ZnO with relatively less surface area could decrease the UV light utilization rate and reduce the photocatalytic activity, resulting in lowering the decolorization efficiency of RhB. These imply that the photocatalysis is highly dependent on UV light radiation. When photon energy of the light source is greater than or equal to the band gap of ZnO, the photocatalysis will be activated. ZnO microstructures generate electron–hole pairs at the tail states of conduction and valence bands. The photogenerated electrons diffused to the adsorbed RhB molecules on the photocatalytic surfaces. The excited electrons from the photocatalytic conduction bands entered into the molecular structure of RhB and disrupted its conjugated system, leading to the complete degradation of RhB. Holes in the valence bands reacted with water to generate $OH^{\bullet}$ and could be used for oxidation of the organic dye [44–46].

$$ZnO + h\nu \rightarrow ZnO\ (e_{CB}^{-} + h_{VB}^{+}) \quad (4)$$

$$H_2O + h_{VB}^{+} \rightarrow H^{+} + OH^{\bullet} \quad (5)$$

$$\text{dye} + OH^{\bullet} \rightarrow \text{oxidation products} \quad (6)$$

Reaction rate of photo-degradation of RhB by ZnO under UV-visible light was calculated using the normalized concentration. The $\ln C_o/C$ vs reaction time was plotted and apparent rate constant (k_a) values were determined from their slopes. The linearity of the plots with correlation coefficient $R^2 \rightarrow 1$ suggests that the decolorization reaction of

RhB follows pseudo-first-order kinetics [43, 45, 47]. The reaction rate constants of RhB degradation of hexagonal prisms and hexagonal pyramids of flower-like ZnO microstructures are 5.44 x 10^{-3} and 8.68 x 10^{-3} min^{-1}, respectively. Clearly, hexagonal pyramids of the flower-like ZnO microstructure is the most appropriate for using as a potential photocatalyst under UV light irradiation.

3.4 Conclusions

In summary, hexagonal prisms and hexagonal pyramids of flower-like ZnO microstructures were successfully synthesized by a microwave-assisted radiation process. The phase, molecular vibration, morphology and optical properties of the as-synthesized ZnO products were characterized by XRD, Raman spectrosocpy, FTIR, EM and UV-visible spectroscopy. In this research, the as-synthesized products were pure wurtzite hexagonal ZnO structure: hexagonal prisms of flower shape at the pH of 9 and hexagonal pyramids of flower shape at the pH of 13. The products show absorption peaks at 397 nm (3.12 eV) for hexagonal prism ZnO microstructure and 384 nm (3.23) eV for hexagonal pyramid ZnO microstructure, which were almost consistent with that of their bulk. In this research, hexagonal pyramid flower-like ZnO exhibited the best photocatalytic activity for photodegradation of RhB with the reaction rate constant of 8.68 x 10^{-3} min^{-1}.

3.5 References

1. S. Suwanboon, R. Tanattha, R. Tanakorn, Songklanakarin J. Sci. Technol. 30 (2008) 65–69.
2. R. Yi, N. Zhang, H. Zhou, R. Shi, G. Qiu, X. Liu, Mater. Sci. Engin. B 153 (2008) 25–30.
3. S.J. Kim, H.H. Kim, J.B. Kwon, J.G. Lee, B.H. O, S.G. Lee, E.H. Lee, S.G. Park, Microelectron. Engin. 87(2010) 1534–1536.
4. A. Umar, S.H. Kim, J.H. Kim, Y.B. Hahn, Mater. Lett. 62 (2008) 167–171.
5. J. Zhao, Z.G. Jin, X.X. Liu, Z.F. Liu, J. EU Ceram. Soc. 26 (2008) 3745–3752.
6. X. Ren, D. Han, D. Chen, F. Tang, Mater. Res. Bull. 42 (2007) 807–813.
7. C. Deng, H. Hu, G. Shao, C. Han, Mater. Lett. 64 (2010) 852–855.
8. X. Jia, H. Fan, F. Zhang, L. Qin, Ultrason. Sonochem. 17 (2010) 284–287.

9. M. Mazloumi, S. Zanganeh, A. Kajbafvala, P. Ghariniyat, S. Taghavi, A. Lak, M. Mohajerani, S.K. Sadrnezhaad, Ultrason. Sonochem. 16 (2009) 11–14.
10. T. Thongtem, A. Phuruangrat, S. Thongtem, Curr. Appl. Phys. 9 (2009) S197–S200.
11. A.E. Kandjani, M.F. Tabriz, B. Pourabbas, Mater. Res. Bull. 43 (2008) 645–654.
12. X. Hou, F. Zhou, Y. Sun, W. Liu, Mater. Lett. 61 (2207) 1789–1792.
13. K. Ada, M. Gökgöz, M. Önal, Y. Sarıkaya, Powder Technol. 181 (2008) 285–291.
14. J. Lee, J. Chae, K. Nahm, M. Kang, J. Industr. Engin. Chem. 15 (2009) 645–648.
15. P.F. Lin, C.Y. Ko, W.T. Lin, C.T. Lee, Mater. Lett. 61 (2207) 1767–1770.
16. Z. Liu, C. Liu, J. Ya, E. Lei, Renew. Energy 36 (2011) 1177–1181.
17. Y.J. Chen, C.L. Zhu, G. Xiao, Sens. Actuat. B 129 (2008) 639–642.
18. J.F. Yan, Y.M. Lu, H.W. Liang, Y.C. Liu, B.H. Li, X.W. Fan, J.M. Zhou, J. Cryst. Growth 280 (2005) 206–211.
19. H.W. Liang, Y.M. Lu, D.Z. Shen, B.H. Li, Z.Z. Zhang, C.X. Shan, J.Y. Zhang, X.W. Fan, G.T. Du, Solid State Commun. 137 (2006) 182–186.
20. T. Thongtem, A. Phuruangrat, S. Thongtem, Ceram. Internat. 36 (2010) 257–262.
21. K. Haga, M. Kamidaira, Y. Kashiwaba, T. Sekiguchi, H. Watanabe, J. Cryst. Growth 214-215 (2010) 77–80.
22. Y. Kashiwaba, F. Katahira, K. Haga, T. Sekiguchi, H. Watanabe, J. Cryst. Growth 221 (2000) 431–434.
23. T.L. Phan, S.C. Yu, R. Vincent, N.H. Dan, W.S. Shi, J. Luminesc. 130 (2010) 1142–1146.
24. Y. Köseoğlu, Ceram. Internat. 40 (2014) 4673–4679.
25. D. Li, J. Wang, X. Wu, C. Feng, X. Li, Ultrason. Sonochem., 20 (2013) 133–136
26. Powder Diffract. File, JCPDS-ICDD, 12 Campus Boulevard, Newtown Square, PA 19073-3273, U.S.A., (2001).
27. H.M. Cheng, K.F. Lin, H.C. Hsu, C.J. Lin, L.J. Lin, W.F. Hsieh, J. Phys. Chem. B 109 (2005) 18385–18390.
28. O. Yayapao, T. Thongtem, A. Phuruangrat, S. Thongtem, J. Alloys Compd. 576 (2013) 72–79.

29. O. Yayapao, S. Thongtem, A. Phuruangrat, T. Thongtem, Ceram. Internat. 39 (2013) S563–S568.
30. S. Baruah, J. Dutta, Sci. Technol. Adv. Mater. 10 (2009) 013001.
31. Z.L. Wang, Mater. Sci. Engin. R 64 (2009) 33–71.
32. X.L. Hu, Y.J. Zhu, S.W. Wang, Mater. Chem. Phys. 88 (2004) 421–426 (2004).
33. A. Umar, M.M. Rahman, A. Al-Hajry, Y.B. Hahn, Talanta 78 (2009) 284–289.
34. Y.J. Gao, W.C. Zhang, X.L. Wu, Y. Xia, G.S. Huang, L.L. Xu, J.C. Shen, G.G. Siu, P.K. Chu, Appl. Surf. Sci. 255 (2006) 1982–1987.
35. R.B. Kale, Y.J. Hsu, Y.F. Lin, S.Y. Lu, Solid State Commun. 142 (2007) 302–305.
36. T. Ghoshal, S. Kar, J. Ghatak, S. Chaudhuri, Mater. Res. Bull. 43 (2008) 2228–2238.
37. S. Musić, Đ. Dragčevič, S. Popovič, J. Alloys Compd. 429 (2007) 242–249.
38. Y. Zhang, J. Mu, Nanotechnology, 18 (2007) 075606.
39. P. Li, H. Liu, Y.F. Zhang, Y. Wei, X.K. Wang, Mater. Chem. Phys., 106 (2007) 63–69.
40. S.C. Padmanabhan, D. Ledwith, S.C. Pillai, D.E. McCormack, J.M. Kelly, J. Mater. Chem., 19 (2009) 9250–9259.
41. P. Li, Y. Wei, H. Liu, X. Wang, J. Solid State Chem., 178 (2005) 855–860.
42. Q. Xie, Z. Dai, J. Liang, L. Xu, W. Yu, Y. Qian, Solid State Commun. 136 (2005) 304–307.
43. J. Xie, H. Wang, M. Duan, L. Zhang, Appl. Surf. Sci. 257 (2011) 6358–6363.
44. X. Li, Y. Cheng, S. Kang, J. Mu, Appl. Surf. Sci. 256 (2010) 6705–6709.
45. S. Ma, R. Li, C. Lv, W. Xu, X. Gou, J. Hazard. Mater. 192 (2011) 730–740.
46. J. Yang, J. Wang, X. Li, J. Lang, F. Liu, L. Yang, H. Zhai, M. Gao, X. Zhao, J. Alloys Compd. 528 (2012) 28–33.
47. Y. Lai, M. Meng, Y. Yu, X. Wang, T. Ding, Appl. Catal. B 105 (2011) 335–345.

Appendix

Materials Letters 91 (2013) 179–182

Contents lists available at SciVerse ScienceDirect

Materials Letters

journal homepage: www.elsevier.com/locate/matlet

Ultrasound-assisted synthesis, characterization and optical property of 0–3 wt% Sn-doped ZnO

Anukorn Phuruangrat [a,*], Sumittra Kongnuanyai [a], Titipun Thongtem [b], Somchai Thongtem [c,**]

[a] Department of Materials Science and Technology, Faculty of Science, Prince of Songkla University, Hat Yai, Songkhla 90112, Thailand
[b] Department of Chemistry, Faculty of Science, Chiang Mai University, Chiang Mai 50200, Thailand
[c] Department of Physics and Materials Science, Faculty of Science, Chiang Mai University, Chiang Mai 50200, Thailand

ARTICLE INFO

Article history:
Received 7 July 2012
Accepted 25 September 2012
Available online 5 October 2012

Keywords:
Electron microscopy
Optical materials and properties
X-ray techniques

ABSTRACT

Sn-doped ZnO samples were successfully synthesized by an ultrasonic solution method, and characterized by X-ray diffraction and electron microscopy. All samples were specified as hexagonal wurtzite ZnO with flower-like structure for pure ZnO and 1 wt% Sn-doped ZnO, and with agglomerates of nanoparticles for 2 and 3 wt% Sn-doped ZnO. Room temperature UV–visible spectra exhibited 373 nm band edge absorption for wurtzite hexagonal pure ZnO, and were red-shift broad absorption bands from ultraviolet for pure ZnO to visible region for 1, 2 and 3 wt% Sn-doped ZnO. The improvement of visible absorption in the Sn-doped ZnO samples was suggested to be the result of lattice defects caused by Sn dopant.

1. Introduction

ZnO (3.37 eV wide band gap at room temperature and 60 meV large exciton binding energy) is one of the most promising semiconductors used for short wavelength optoelectronic devices operating in the blue and ultraviolet region. It has been investigated as transparent conductors and piezoelectric materials for solar cells, transparent electrodes and gas sensors. To enhance the electrical/optical properties, ZnO was doped with group III, IV and V elements due to its superior conducting properties based on oxygen vacancies [1–6]. Recently, ZnO doped with Al, Ga, In, Sn and Sb were reported to have high potential applications for gas sensors, dye-sensitized solar cells and photocatalysis [6–8]. In particular, ZnO film doped with 1–2 at% Al exhibited low resistivity and was regarded as an alternative potential candidate for indium-tin-oxide [1,9]. In-doped ZnO films showed excellent conductive property and high transparency [10]. ZnO was able to emit shorter wavelengths by doping with In [11] and red spectrum by doping with Eu^{3+} ions [12]. The main reason of choosing tin-doped ZnO is to enhance the electrical conductivity. When ZnO is doped with Sn^{4+}, the ions substitute for Zn^{2+} sites in ZnO crystal, leading to two more negative charges to enhance the electrical conductivity. Furthermore, Zn^{2+} ions can be easily substituted by Sn^{4+} ions without large lattice distortion, because they are almost the same size (radii: Zn^{2+} = 0.074 nm, Sn^{4+} = 0.071 nm) [2–4,13].

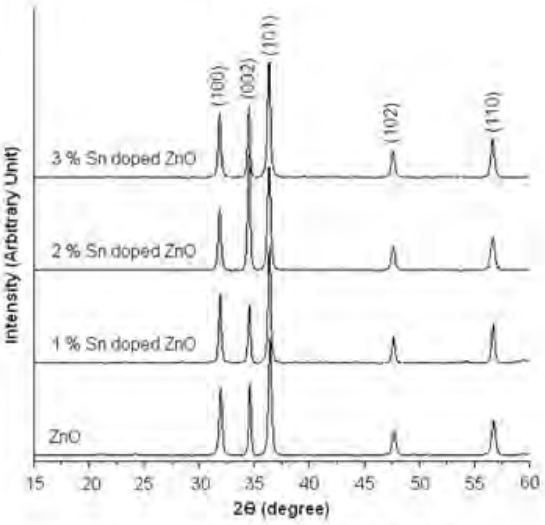

Fig. 1. XRD patterns of 0, 1, 2 and 3 wt% Sn-doped ZnO.

* Corresponding author. Tel.: +66 74288374; fax: +66 74288395.
** Corresponding author. Tel.: +66 53941924; fax: +66 53943445.
E-mail addresses: phuruangrat@hotmail.com (A. Phuruangrat), schthongtem@yahoo.com (S. Thongtem).

0167-577X/$ - see front matter © 2012 Elsevier B.V. All rights reserved.
http://dx.doi.org/10.1016/j.matlet.2012.09.091

In this research, the synthesis of crystalline ZnO doped with different contents of Sn^{4+} via ultrasonic chemical method is reported. The ultimate goal is to improve the optical property of the crystals to utilize for visible sunlight.

2. Experiment

Typically, 0.01 mol zinc nitrate hexahydrate and 0–3 wt% Sn^{4+} of tin chloride were dissolved in 100 ml deionized water, into

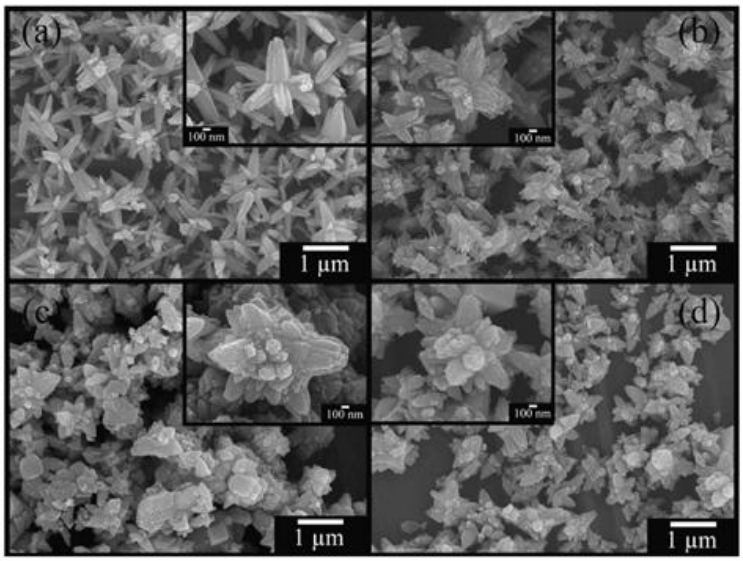

Fig. 2. SEM images of (a–d) 0, 1, 2 and 3 wt% Sn-doped ZnO, respectively.

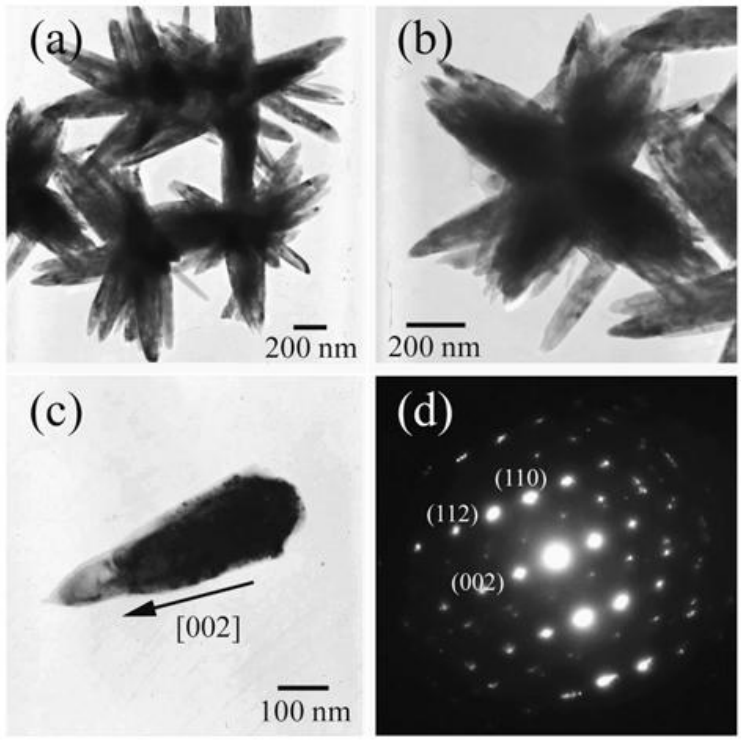

Fig. 3. TEM images and SAED pattern of pure ZnO flowers.

which a 28% ammonium hydroxide solution was continuously dropped and stirred until the solution pH reaching at 8.5. Upon irradiation with 35 kHz ultrasound at 80 °C for 3 h, the precipitates were synthesized, filtered, washed with methanol several times and dried at 80 °C for 12 h. The products were characterized by X-ray diffraction, electron microscopy and UV–visible spectrometry.

3. Results and discussion

All diffraction peaks (Fig. 1) were identified to correspond with hexagonal wurtzite structured ZnO (JCPDS no. 36-1451) as the main product [6,14]. Incorporation of Sn in crystalline lattice of ZnO host can play the role in density of the native point defects such as vacancies, interstitials and anti-sited defects; especially, the host with higher concentration of dopant. It should be noted that Sn concentration of the Sn-doped ZnO samples was so low that the elemental Sn was unable to be detected by this XRD analysis.

General morphology of the as-synthesized ZnO (Fig. 2a) was uniform flower-like nanostructure composed of different oriented petals directly grown out of the bases of central crystalline towers. Diameters of the towers gradually decreased from 400 nm at the bottom to 200 nm at the tip. Each of the petals and towers was composed of several parallel agglomerated ZnO nanorods. Upon doping with different contents of Sn, the product shapes were still flowers for 1 wt% Sn-doped ZnO (Fig. 2b), and agglomerates of nanoparticles for 2 and 3 wt% Sn-doped ZnO (Fig. 2c and d). The 1 wt% Sn-doped ZnO shows petals and towers composed of multineedles with 20–120 nm long and 20 nm diameter grown from central cores. A number of agglomerated nanoparticles composing the petals were detected in both the 2 and 3 wt% Sn-doped ZnO.

The elemental composition of the as-synthesized samples was analyzed by EDX (results not shown). For this analysis, zinc and oxygen with 1:1 atomic ratio were detected for pure ZnO, including the detection of additional Sn for 1, 2 and 3 wt% Sn-doped ZnO. Intense peaks of Cu and Au originated from Cu stubs and sputtered Au were also detected. The EDX mapping of 3 wt%

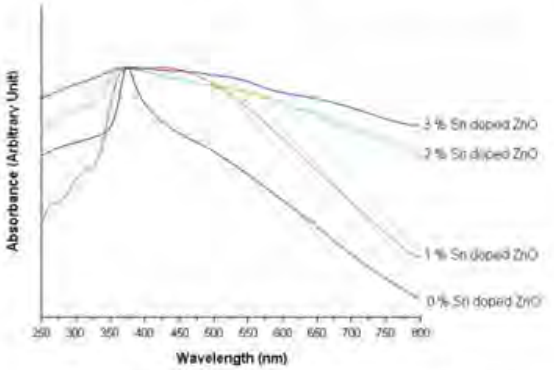

Fig. 5. Absorption spectra of 0, 1, 2 and 3 wt% Sn-doped ZnO.

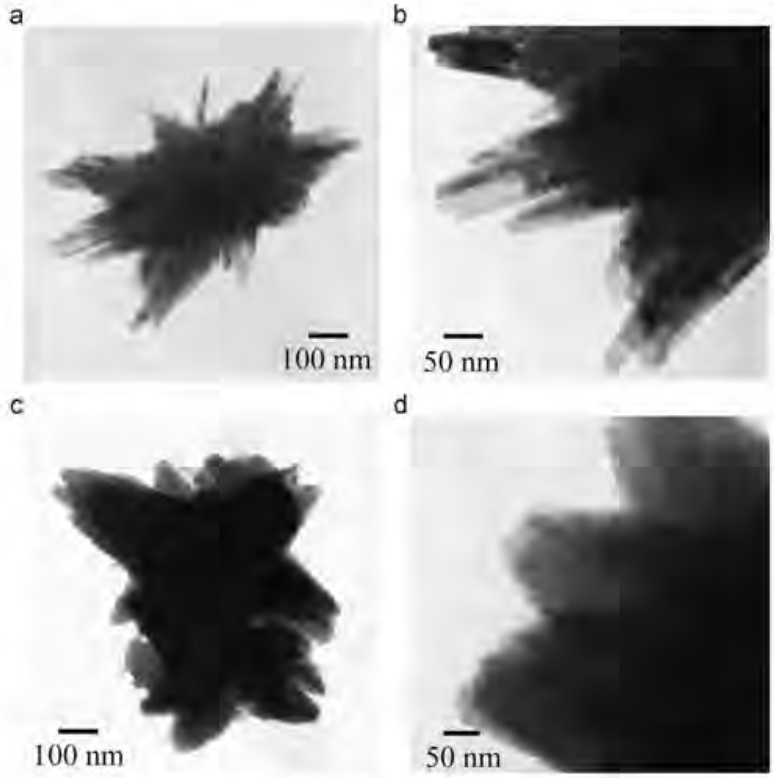

Fig. 4. TEM images of (a, b) 1 wt% and (c, d) 3 wt% Sn-doped ZnO.

Sn-doped ZnO was mainly composed of uniformly distributive Zn, O and Sn, which revealed the random doping of Sn in the crystal lattice.

TEM images of ZnO (Fig. 3a and b) present the uniform flower-like ZnO nanostructure, consisted of petals shaped like rods with sharp tips. The rod-like petals with the same size as those characterized by SEM were also detected, and have smooth surfaces. The petal (Fig. 3c) has a preferential growth along the *c*-axis. A SAED pattern (Fig. 3d) on a rod-like petal was composed of bright spots with 6-fold symmetry, belonging to hexagonal ZnO single crystal, with the [−110] direction as zone axis.

TEM images of the 1 and 3 wt% Sn-doped ZnO at low and high magnifications are shown in Fig. 4. At low magnification, the samples shaped like flowers composed of multineedle-like petals grown out of cores for the first, and agglomeration of nanoparticles for the second. Close-up observation on them, a number of crystalline needles composed the petals were detected for the 1 wt% Sn-doped ZnO, and different orientations of nanoparticles built up agglomerations for the 3 wt% Sn-doped ZnO.

UV–visible spectra (Fig. 5) of the as-synthesized 0–3% Sn-doped ZnO revealed that the Sn dopant can play the role in changing the absorption characteristics of pure ZnO. Strong absorption band in UV region at 373 nm attributed to the band edge absorption of wurtzite hexagonal pure ZnO, blue shift relative to its bulk (380 nm) [15]. Those of the 1, 2 and 3 wt% Sn-doped ZnO were red-shift broad absorption bands from UV to visible regions, caused by the increase of lattice defects by dopant concentration increasing. Generally, the red-shift in absorption wavelength and the increase in absorption intensity were believed to relate with the increase in the electron-hole pair formation rate on the photocatalytic surfaces [8], resulting in the higher photocatalytic activity of Sn-doped ZnO utilizing for sunlight.

4. Conclusions

Samples of 0, 1, 2 and 3 wt% Sn-doped ZnO were successfully synthesized by an ultrasonic solution method at 80 °C for 3 h. In this research, XRD patterns were used to identify the hexagonal wurtzite ZnO phase. Uniform flower-like nanostructures were composed of different oriented petals, each of which was directly grown out of crystalline cores, characterized by electron microscopy. The UV–visible absorption of the 1–3 wt% Sn-doped ZnO exhibited red-shift broad absorption bands from ultraviolet for pure ZnO to visible sunlight by doping element residing in ZnO crystal.

Acknowledgment

We wish to thank the Thailand Research Fund (TRF) for providing financial support through the TRF research contract MRG5580112.

References

[1] Bae SY, Na CW, Kang JH, Park J. J Phys Chem B 2005;109:2526–31.
[2] Deng R, Zhang XT, Zhang E, Liang Y, Liu Z, Xu HY, et al. J Phys Chem C 2007;111:13013–5.
[3] Qu X, I S, Bai L, Meng Q, Jia D. Physica B 2012;407:268–70.
[4] Caglar Y, Aksoy S, Ilican S, Caglar M. Superlatt Microst 2009;46:469–75.
[5] Sheini FJ, More MA, Jadkar SR, Patil KR, Pillai VK, Joag DS. J Phys Chem C 2010;114:3843–9.
[6] Navale SC, Mulla IS. Mater Sci Eng C 2009;29:1317–20.
[7] Ye N, Qi J, Qi Z, Zhang X, Yang Y, Liu J, et al. J Power Sourc 2010;195:5806–9.
[8] Sun JH, Dong SY, Feng JL, Yin XJ, Zhao XC. J Mol Catal A 2011;335:145–50.
[9] Kim YS, Tai WP, Appl Surf Sci 2007;253:4911–6.
[10] Pál E, Hornok V, Oszkó A, Dékány I, Colloid Surf A 2009;340:1–9.
[11] Youseft R, Jamali-Sheini F, Zak AK, Mahmoudian MR. Ceram Inter 2012;38:6295–301.
[12] Tsuji T, Terai Y, Kamarudin MHB, Yoshida K, Fujiwara Y. J Lumin 2012;132:3125–8.
[13] Sheini FJ, Joag DS, More MA. Thin Solid Films 2010;519:184–9.
[14] Powder Diffract. File, JCPDS-ICDD, 12 Campus Boulevard, Newtown Square, PA 19073-3273, USA, 2001.
[15] Liu JS, Cao JM, Li ZQ, Ji GB, Zheng MB. Mater Lett 2007;61:4409–11.

Hindawi Publishing Corporation
Journal of Nanomaterials
Volume 2014, Article ID 725817, 10 pages
http://dx.doi.org/10.1155/2014/725817

Hindawi

Research Article

Ultrasonic-Assisted Synthesis, Characterization, and Optical Properties of Sb Doped ZnO and Their Photocatalytic Activities

Anukorn Phuruangrat,[1] Waipawan Kongpet,[1] Oranuch Yayapao,[2] Budsabong Kuntalue,[3] Somchai Thongtem,[2,4] and Titipun Thongtem[4,5]

[1] *Department of Materials Science and Technology, Faculty of Science, Prince of Songkla University, Hat Yai, Songkhla 90112, Thailand*
[2] *Department of Physics and Materials Science, Faculty of Science, Chiang Mai University, Chiang Mai 50200, Thailand*
[3] *Electron Microscopy Research and Service Center, Faculty of Science, Chiang Mai University, Chiang Mai 50200, Thailand*
[4] *Materials Science Research Center, Faculty of Science, Chiang Mai University, Chiang Mai 50200, Thailand*
[5] *Department of Chemistry, Faculty of Science, Chiang Mai University, Chiang Mai 50200, Thailand*

Correspondence should be addressed to Anukorn Phuruangrat; phuruangrat@hotmail.com and Somchai Thongtem; schthongtem@yahoo.com

Received 3 September 2013; Revised 21 November 2013; Accepted 4 December 2013; Published 5 February 2014

Academic Editor: Zhenhui Kang

Sb doped ZnO nanostructures were synthesized by an ultrasonic-assisted method. Effect of Sb dopant on the structure, morphology, and composition of as-synthesized Sb doped ZnO nanostructures was investigated by X-ray diffraction (XRD), scanning electron microscopy (SEM), energy dispersive X-ray (EDX) spectroscopy, and transmission electron microscopy (TEM). All samples were identified to wurtzite hexagonal ZnO structure. UV-visible spectra of the as-synthesized 3% Sb doped ZnO sample exhibit broad absorption bands at around 343 nm which is blue shift of 373 nm of pure ZnO. The photocatalytic activity was tested by decolorization of methylene blue (MB) solution under UV light. After 300 min irradiation, the degradation efficiencies were 56, 90, and 95% for ZnO, 1% Sb doped ZnO, and 3% Sb doped ZnO, respectively. The 3% Sb doped ZnO shows the highest photocatalytic activity than any other samples.

1. Introduction

Zinc oxide (ZnO) is a n-type II–VI semiconductor with a wide direct band gap of 3.37 eV and large exciton binding energy of 60 meV [1–5], which is more than other semiconductor materials: ZnSe (22 meV) and GaN (25 meV) [6]. It has interesting applications on nanolasers, piezoelectric nanogenerators, solar cells, gas sensors, and photocatalyst, due to its unique optical and electrical properties [1, 2, 4, 7]. However, its electrical and optical properties are not able to completely meet the requirements of constructing high performance semiconducting devices, including the increasing needs for applications nowadays [1, 2, 5]. To enhance these properties, ZnO was frequently doped with some dopants [1, 2, 5] such as Sb [6, 8], Sn [9], In [10, 11], Mn [12], and Ce [13]. Sn doped ZnO shows the highest gas response to ethanol vapor and highest photocatalytic activity toward methyl orange (MO) solution [9]. The 2% Ce doped ZnO shows an effective oxidation of cyanide to cyanate [13]. Sb doped ZnO nanoparticles have higher resistance and reflectivity than the undoped ones [8].

In this research, a facile and environment-friendly low-temperature route was used to synthesize Sb doped ZnO by ultrasonic-assisted solution method. Phase, morphologies, optical properties, and photocatalytic properties of Sb doped ZnO were also studied and discussed in this report.

2. Experimental Procedures

Sb doped ZnO nanostructures were synthesized by the ultrasonic-assisted solution method using zinc nitrate hexahydrate ($Zn(NO_3)_2{\cdot}6H_2O$), antimony chloride ($SbCl_3$), and ammonium hydroxide (NH_4OH) as starting materials. All

the chemicals for this synthesis were purchased from Aldrich Chemical Corporation and used without further purification.

For the typical experimental procedure, 0.01 mol of $Zn(NO_3)_2{\cdot}6H_2O$ and 1–5% by mole of $SbCl_3$ were dissolved in 100 mL of deionized water. Aqueous solution of 28% ammonium hydroxide was dropped in precursor solutions until reaching the pH of 8.5 with continuous stirring to precipitate Zn^{2+} and Sb^{3+} ions into metal hydroxide compound. Subsequently, the resultant solutions were transferred into sonication bath (35 kHz) and sonicated at 80°C for 3 h. In the end, the precipitates were filtered and washed with methanol several times to remove ionic impurities and finally dried at room temperature.

Crystalline phases of the as-synthesized nanostructured materials were analyzed by an X-ray diffractometer (XRD, Philips X'Pert MPD) with Cu-K_α radiation in the 2θ = 15°–75° range. The morphology investigation was carried out by field emission scanning electron microscopy (FE-SEM, JEOL JSM-6335F) and transmission electron microscopy (TEM, JEOL JEM-2010) operating at 35 kV and 200 kV, respectively. The optical properties were studied by a Perkin Elmer, Lambda 25 UV-visible spectrometer.

Photocatalytic activity was tested by decolorization of methylene blue (MB) in aqueous solution under UV light. The 150 mg pure ZnO and Sb doped ZnO as photocatalysts were suspended in 150 mL 10^{-5} M MB solutions and were magnetically stirred for 30 min in the dark environment to establish an adsorption/desorption equilibrium of MB on surfaces of the photocatalysts. After UV irradiating, the concentrations of MB were determined by a UV-visible spectrophotometer (Lambda 25, Perkin Elmer) using a wavelength of 664 nm. The decolorization efficiency (%) was calculated as follows:

$$\text{decolorization efficiency (\%)} = \frac{C_o - C}{C_o} \times 100 \quad (1)$$

where C_o and C were the initial concentration of MB and the concentration of MB after UV irradiation, respectively.

3. Results and Discussion

The purity and crystalline properties of the as-synthesized ZnO and Sb doped ZnO samples were determined by X-ray diffraction (XRD) as shown in **Figure 1**. The XRD pattern of ZnO without Sb dopant showed diffraction peaks at 2θ = 31.8°, 34.5°, 36.4°, 47.5°, 57.1°, 63.2°, 66.7°, 67.8°, and 69.0°, identified to the (100), (002), (101), (102), (110), (103), (200), (112), and (201) planes, respectively, of bulk wurtzite hexagonal ZnO structure (JCPDS no. 36-1451) [14]. No observed characteristic peaks corresponding to impurities such as $Zn(OH)_2$ were detected in the pattern, confirming the purity of ZnO sample. XRD patterns of 1–3% Sb doped ZnO show the same diffraction pattern as pure wurtzite hexagonal ZnO structure with JCPDS no. 36-1451. no diffraction peaks of impurity phases such as $Zn(OH)_2$, Sb_2O_3, and Sb were detected in these samples, suggesting that Sb^{3+} ions could uniformly substitute into the Zn^{2+} sites or interstitial sites of ZnO lattice by forming $2Sb_{Zn}$ and V_{Zn} [3]. Moreover,

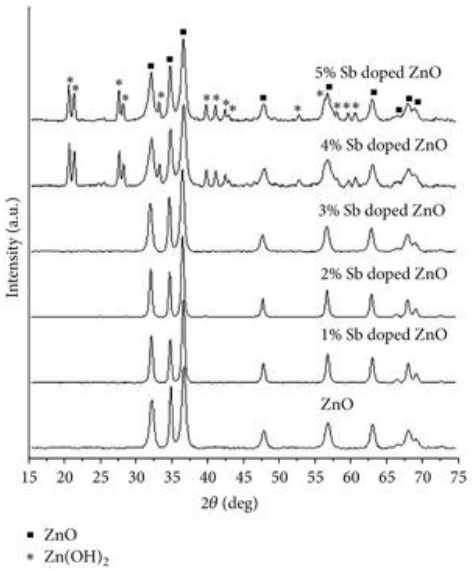

Figure 1: XRD patterns of the products synthesized by ultrasonic-assisted solution method.

the major diffraction peaks shifted slightly towards smaller diffraction angle compared to the pure ZnO phase due to the ionic radius of Sb^{3+} of 0.76 Å [15, 16] >ionic radius of Zn^{2+} of 0.74 Å [16, 17]. Upon increasing the Sb concentration doped in ZnO structure of more than 3%, mixed phases of $Zn(OH)_2$ and ZnO (JCPDS no. 38-0385 [14] for $Zn(OH)_2$ and no. 36-1451 [14] for ZnO) were detected. The XRD results show that the limited Sb concentration doped in ZnO is 3 wt% in this research.

Figures 2 and 3 show the FE-SEM images of the as-synthesized 0–3% Sb doped ZnO products with low and high magnifications. A morphology of pure ZnO as shown in Figure 2(a) was well-defined flower-like three-dimensional ZnO nanostructures in a large-scale area with diameters in the range of 0.5–1 μm. It should be noted that the flower-like three-dimensional ZnO nanostructures were composed of assemblies of nanorods as petals. At high magnification image of the nanorod-built flower-like ZnO nanostructures in Figure 3(a), they revealed that each petal was about 300 nm long and 100 nm in diameter. For the SEM images of Sb doped ZnO, the morphologies of rice kernel-like ZnO nanostructures formed instead of flower-like structures. Figures 2(b), 2(c), and 2(d) and Figures 3(b), 3(c), and 3(d) show SEM images of 1–3% Sb doped ZnO prepared by ultrasonic-assisted solution method at low and high magnifications. They show the rice kernel-like ZnO nanorods in the range of 300–400 nm long. However, no flower-like structures were detected in the Sb doped ZnO samples. At high magnification, the products were composed of assembled nanorods to build rice kernel-like ZnO nanorods. These different morphologies of ZnO and 1–3% Sb doped ZnO can

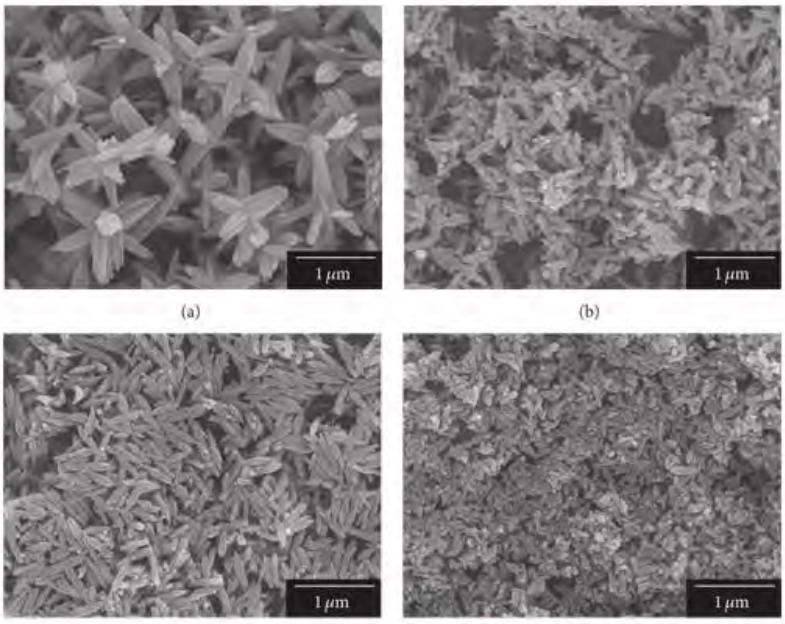

FIGURE 2: SEM images of (a) pure ZnO, (b) 1% Sb doped ZnO, (c) 2% Sb doped ZnO, and (d) 3% Sb doped ZnO samples at low magnification.

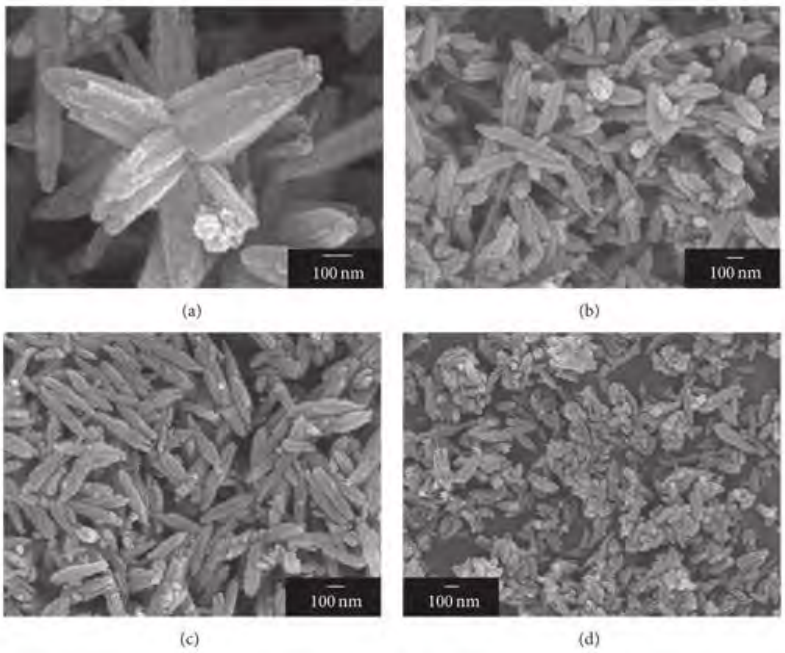

FIGURE 3: SEM images of (a) pure ZnO, (b) 1% Sb doped ZnO, (c) 2% Sb doped ZnO, and (d) 3% Sb doped ZnO samples at high magnification.

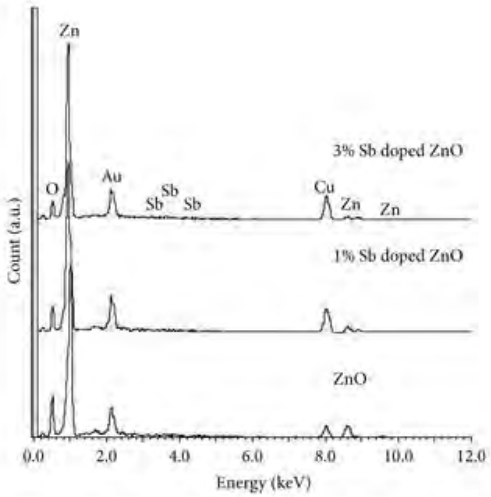

FIGURE 4: EDX spectra of the products synthesized by ultrasonic-assisted solution method.

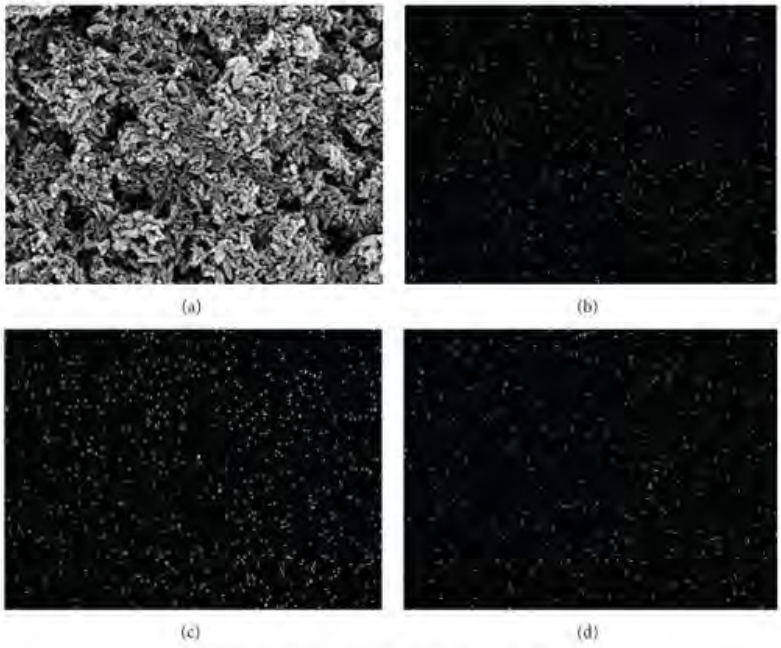

FIGURE 5: EDX mapping of 3% Sb doped ZnO sample.

be explained in terms of a thermodynamic barrier arising from the Sb^{3+} dopant that slowed down the nucleation and inhibited the further growth of Sb doped ZnO crystals [18].

Chemical composition of the as-synthesized products was observed using EDX analysis. Figures 4 and 5 show the typical EDX spectra of 0–3% Sb doped ZnO and EDX mapping of 3% Sb doped ZnO. EDX spectra show that the products consisted of zinc and oxygen for pure ZnO and zinc, oxygen, and antimony atoms for 1–3% Sb doped ZnO. Intense peaks of Cu and Au were also detected in the spectra due to the Cu stubs and sputtered Au. There was no detection of other impurities in the products, indicating that they had very high purity. Figure 5 shows selected area elemental mapping of 3% Sb doped ZnO. The mapping was

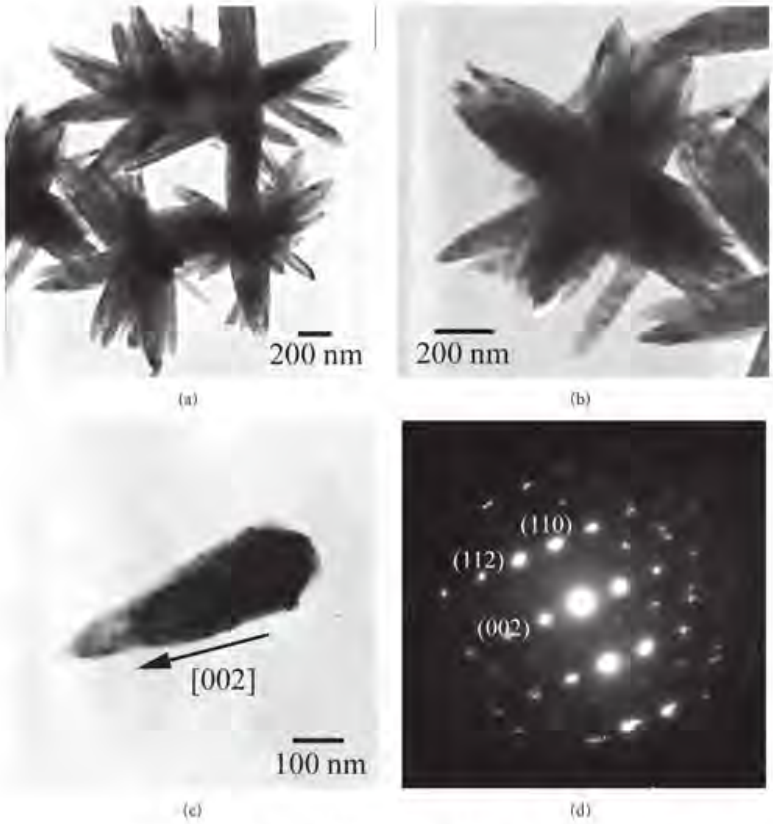

FIGURE 6: TEM images and SAED pattern of flower-like ZnO structure.

mainly composed of Zn, O, and Sb elements. The Sb element was uniformly diffusive in ZnO lattice.

Figure 6(a) shows a bright-field TEM image of the as-synthesized ZnO sample. It indicates the detailed morphology of the ZnO product with flower-like shape. As shown in Figure 6(b), it can be clearly seen that the detailed shape of some petals of flower-like ZnO product was composed of many clusters ZnO nanorods. These nanorods were in contact with each other as bundles, growing outwardly by forming flower-like structures. The shape of the product appears as flowers with several symmetric petals. It indicated that every bundle was composed of closely packed nanorods with average diameters of around 150 nm. By performing on the individual petal (Figure 6(c)), the selected area electron diffraction (SAED) pattern, as shown in Figure 6(d), indicates that the single petal is single crystal of hexagonal ZnO phase. The individual petal was also confirmed that the nanorods grow along the [0001] direction.

Regarding the formation of flower-like ZnO, it can be explained by manipulating the growth kinetics. In the present case, the contributing growth-driving force for ZnO crystals is the concentration of ZnO_2^{2-} monomers. In the reaction solution containing $Zn(NO_3)_2$ and NH_4OH, the high reactant concentrations led to the burst of initial homogeneous nucleation, and the supersaturated ZnO nuclei aggregated together in groups. As the reaction proceeded, concentration of the ZnO_2^{2-} monomers became lower. Some active sites on the surface of the initially formed ZnO aggregates grew along the oriented direction as the chemical environment constantly provided reactants. Due to the intrinsic anisotropy in its growth rate (v) with $v[0001] \gg v[01\text{-}10] > v[000\text{-}1]$, the preferential growth of the product is along the [0001] direction [7, 19]. The structure of ZnO single crystal can be described as a number of alternating planes of coordinated O^{2-} and Zn^{2+} ions. The oppositely charged ions are made of the positively charged Zn-(0001) and negatively charged O-(0001) polar surfaces. Following the decrease of the concentration of ZnO_2^{2-} monomers due to the initial fast nucleation of ZnO, the absorption of OH^- on the positively charged Zn-(0001) plane dominated the ZnO_2^{2-} growth units. Therefore, the superfluous OH^- ions stabilized the surface charge and the structure of Zn-(0001) face to some degree, allowing

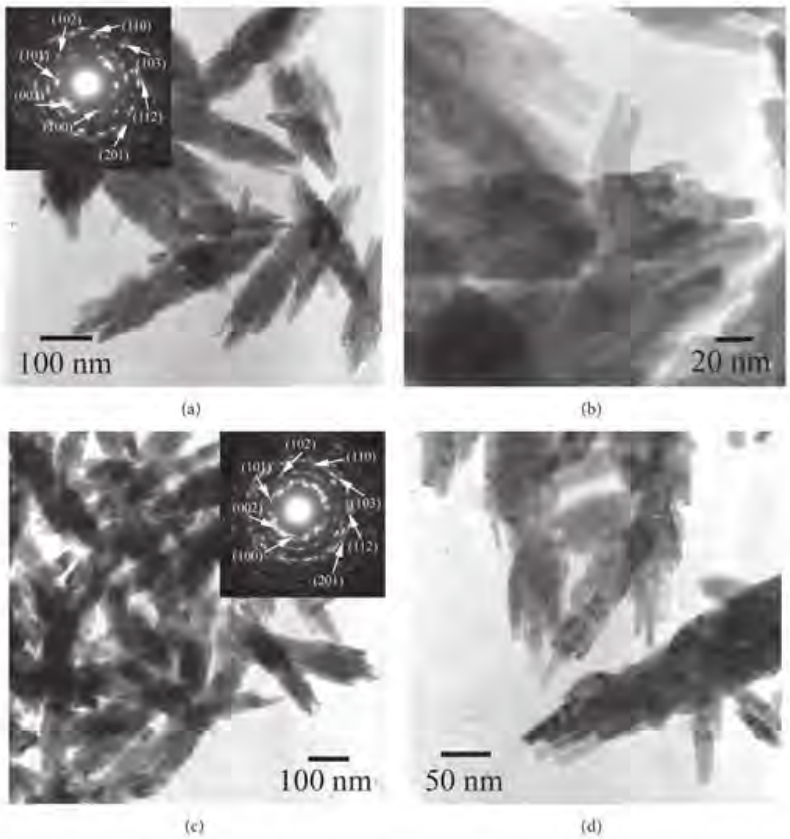

FIGURE 7: TEM images and SAED patterns of (a) and (b) 1% Sb doped ZnO, and (c) and (d) 3% Sb doped ZnO samples.

the fast growth along the [0001] direction, leading to the formation of flower-like ZnO nanostructure [7, 20–22].

Figure 7 shows the typical TEM images of 1% and 3% Sb doped ZnO nanostructures. It is apparent that 1% Sb doped ZnO exhibits well-defined rice kernel-like colonies with an average size of 300–400 nm. The nanorods serving as building blocks were tightly packed as colonies of rice kernel-like shaped particles. It can be concluded that the rice kernel-like ZnO colonies formed from the attachment of ZnO nanorods. The magnified TEM image in Figure 7(b) shows the detailed colonies of rice kernel-like ZnO. The colonies of rice kernels were composed of densely arrayed nanorods with diameter of about 10 nm. While the colonies of the 3% Sb doped ZnO nanocrystallites as shown in Figure 7(c) present the rice kernel-like colonies of many closely packed nanorods of about 90 nm in diameter and 1.2 μm in length similar to 1% Sb doped ZnO sample. It also shows that the ends of the nanorods have relatively smaller diameters compared to those of the middle parts. The enlarged TEM image of 3% Sb doped ZnO sample as shown in Figure 7(d) shows the colonies of rice kernel-like ZnO particles with very rough surface. It is noteworthy that the rice kernel-like structure was sufficiently stable, which cannot be destroyed even after ultrasonication for a long time. The insets of Figures 7(a) and 7(c) show the SAED pattern taken from their corresponding rice kernel-like Sb-doped ZnO samples. The diffraction patterns were composed of a number of bright spots arranged in concentric rings, with the calculated lattice planes obtained from the diameters of the diffraction rings. For the present research, the products were polycrystalline in nature. They were the (100), (002), (101), (102), (110), (103), (112), and (201) planes which were in accordance with those of the JCPDS database for hexagonal ZnO phase.

The optical properties of as-synthesized 0–3% Sb doped ZnO samples were studied by UV-visible absorption as shown in Figure 8. The spectrum of pure phase ZnO sample exhibits a broad absorption band at around 373 nm, blue shift relative to 380 nm of bulk ZnO [23]. However, the spectra of 1%, 2%, and 3% Sb doped ZnO samples exhibit sharp bands at 356 nm, 350 nm, and 343 nm, respectively. It should be noted that the absorption peaks became sharper. They were blue-shift from 373 nm of pure ZnO sample to 343 nm of

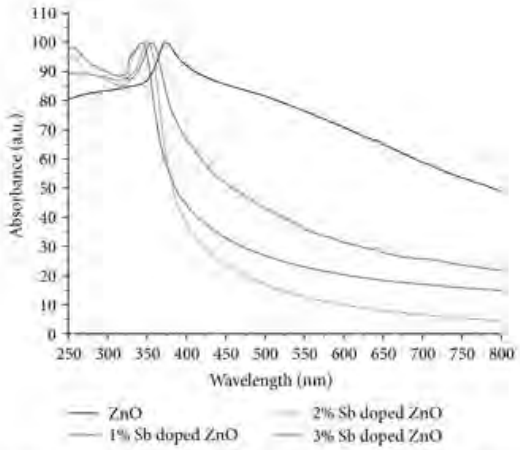

FIGURE 8: UV-visible spectra of as-synthesized 0–3% Sb doped ZnO samples.

3% Sb doped ZnO sample. The band gaps were calculated by the equation of $E_g = 1240/\lambda$ [24, 25]. They are 3.32 eV, 3.48 eV, 3.54 eV, and 3.61 eV for ZnO, 1% Sb doped ZnO, 2% Sb doped ZnO, and 3% Sb doped ZnO, respectively. These can be explained by the decreasing in size of the particles and consequently the increasing band gap between the valence and conduction bands. A blue shift of the absorption peak in the UV-visible spectra of these samples was successfully and clearly observed.

Upon the illumination of UV light, ZnO can transform the photonic energy into chemical energy, in a similar way for the synthesis or the decomposition of organic materials. Its remarkable oxidation reduction capability, high chemical stability, and harmless characteristics are most commonly applied in pollutant removal and disinfectants. When the ZnO samples are illuminated by ultraviolet of wavelength less than 400 nm, electrons of the valence band were excited by the photonic energy of the ultraviolet to the conduction band. At the same time, the valence band created electronic holes carrying positive electricity. These holes reacted with the absorbed O_2 or H_2O to create OH^* free radicals, which further generated the reaction such as disinfection or deodorization [26]. Figure 9(a) shows the UV-visible absorption spectral change of MB during the photocatalytic degradation in the presence of ZnO under UV light over the wavelength range of 400–800 nm. The intensity of main absorption peaks of the MB solutions at approximately 664 nm decreases continuously with the length of UV irradiation time. It indicates that MB molecules could be degraded in the presence of ZnO. The photocatalytic mechanism of ZnO is as follows:

$$\begin{aligned} \mathrm{ZnO} + h\nu &\longrightarrow \mathrm{ZnO}\left(e_{CB}^{-} + h_{VB}^{+}\right) \\ \mathrm{H_2O} + h_{VB}^{+} &\longrightarrow \mathrm{H^{+}} + \mathrm{OH^{*}} \\ \mathrm{dye} + \mathrm{OH^{*}} &\longrightarrow \text{oxidation products} \end{aligned} \tag{2}$$

where h_{VB}^{+} and e_{CB}^{-} are the electron vacancies in the valence band and the photogenerated electrons in the conduction band, respectively. The conduction-band electrons and valence-band holes are generated on the surfaces of ZnO nanostructures when they are illuminated by UV light with energy greater than the band gap. Holes react with water molecules adhering to the surfaces of ZnO nanostructures to form highly reactive hydroxyl radicals (OH^*) which have a powerful oxidation ability to degrade organic dye [7]. Figures 9(b) and 9(c) show the UV-visible absorption spectra of the aqueous solutions of MB with 1% Sb doped ZnO and 3% Sb doped ZnO samples as photocatalysts and illuminated to UV light for different time intervals. The characteristic absorption of MB at 664 nm decreases rapidly with the prolonging time and almost disappears after about 300 min. Further exposure leads to no absorption peak in the whole spectrum, indicating that almost none of the MB remain. These photocatalysis results clearly demonstrate that Sb doped ZnO exhibited higher photocatalytic activity as compared with ZnO sample.

Figure 10 shows MB degradation efficiency of the as-synthesized ZnO and Sb doped ZnO samples. The Sb doped ZnO samples exhibit much higher photocatalytic activities than that of the pure ZnO one. It took only 102 min for 3% Sb doped ZnO and 134 min for 1% Sb doped ZnO to decolorize 50% of MB while pure ZnO took more than 275 min to decolorize the same amount of MB. This faster degradation rate of MB under UV irradiation using Sb doped ZnO is attributed to the increase in defect sites caused by Sb^{3+} doping, leading to an enhanced optical absorption in the UV region. After 300 min of irradiation, the values of degradation efficiency are 56, 90, and 95% for pure ZnO, 1% Sb doped ZnO, and 3% Sb doped ZnO, respectively. This clearly demonstrates that ZnO doped with Sb^{3+} degrades MB more efficiently than undoped ZnO. In this research, the 3% Sb doped ZnO shows the highest photocatalytic activity. Under illumination with UV light, Sb doped ZnO generates electron-hole pairs at the tail states of conduction and valence bands. The generated

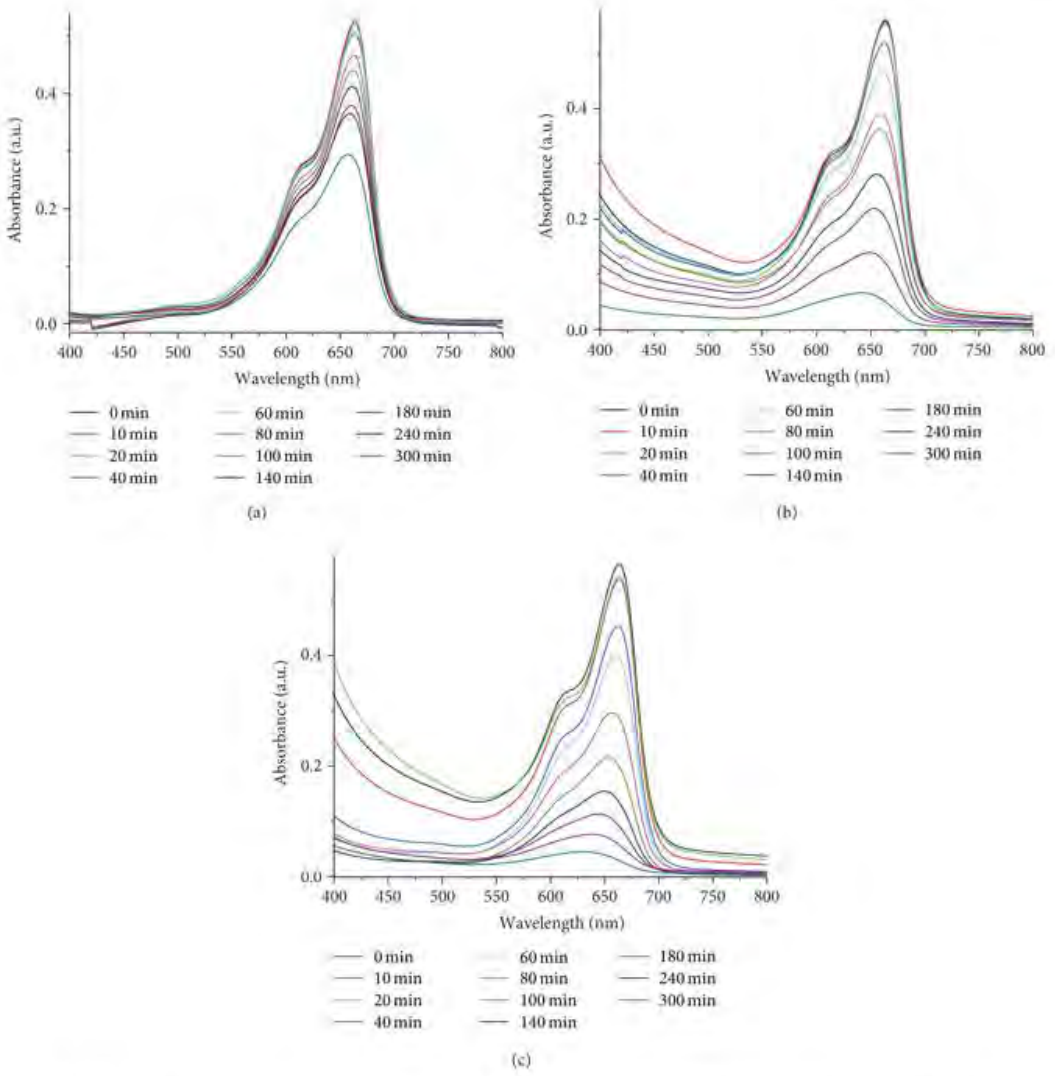

FIGURE 9: UV-visible absorption of MB solutions containing (a) ZnO, (b) 1% Sb doped ZnO and (c) 3% Sb doped ZnO.

electrons diffused to the adsorbed MB molecules on the surface of Sb doped ZnO. The excited electrons from the photocatalyst conduction band migrated into the molecular structure of MB and by forming the conjugated system which then led to the complete decomposition of MB. Holes at the valence band generated $OH^{\bullet}$ via reaction with water or OH^{-} might be used for oxidation of other organic compounds.

The photocatalytic properties of as-synthesized photocatalysts were evaluated by measuring the absorption intensity of MB at 664 nm after UV irradiation at different lengths of time. Both of these photodegradation reactions were determined by pseudo-first-order reactions [27–30]. The reaction rate constants of MB degradation calculated for ZnO, 1% Sb doped ZnO, and 3% Sb doped ZnO are 1.47×10^{-3}, 6.30×10^{-3}, and 8.65×10^{-3} min^{-1}, respectively. This clearly demonstrates that ZnO doped with antimony can be used as a potential photocatalyst illuminated with UV light.

4. Conclusions

Ultrasonic-assisted synthesis of Sb doped ZnO at room temperature has been introduced. XRD results showed the formation of wurtzite ZnO and the upper bound of 3 wt% doped Sb. No other phases were detected. The amount of

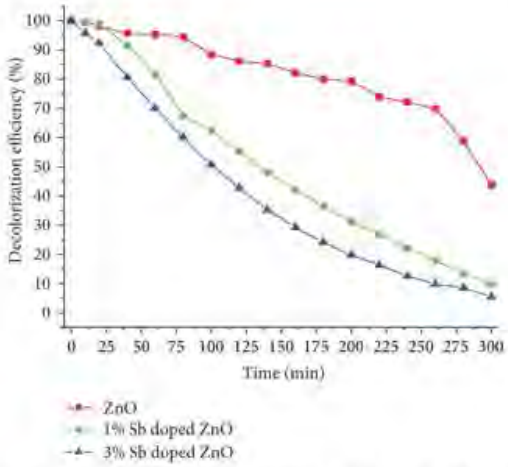

FIGURE 10: Decolorization efficiencies of ZnO with and without Sb doping.

antimony added shows a profound effect on morphology which changed from flower-like structure of nanorods for ZnO to rice kernel-like structure for Sb doped ZnO. As-synthesized doped and undoped ZnO crystals were tested and compared for their photocatalytic activities by decolorization of MB under UV light. It was clear that 3% Sb doped ZnO showed the highest photocatalytic activity toward the MB solution.

Conflict of Interests

The authors declare that there is no conflict of interests regarding the publication of this paper.

Acknowledgment

The authors wish to thank the Thailand Research Fund (TRF) for providing financial support through the TRF research Contract MRG5580112.

References

[1] W.-W. Zhong, F.-M. Liu, L.-G. Cai, X.-Q. Liu, and Y. Li, "Effect of growth time on the structure, Raman shift and photoluminescence of Al and Sb codoped ZnO nanorod ordered array thin films," *Applied Surface Science*, vol. 257, no. 22, pp. 9318–9322, 2011.

[2] D. W. Zeng, C. S. Xie, B. L. Zhu, W. L. Song, and A. H. Wang, "Synthesis and characteristics of Sb-doped ZnO nanoparticles," *Materials Science and Engineering B*, vol. 104, no. 1-2, pp. 68–72, 2003.

[3] X. Fang, J. Li, D. Zhao et al., "Structural and photoluminescence properties of aligned Sb-doped ZnO nanocolumns synthesized by the hydrothermal method," *Thin Solid Films*, vol. 518, no. 20, pp. 5687–5689, 2010.

[4] C. H. Zang, J. E. Su, B. Wang, D. M. Zhang, and Y. S. Zhang, "Photoluminescence of ZnO:Sb nanobelts fabricated by thermal evaporation method," *Journal of Luminescence*, vol. 131, no. 8, pp. 1817–1820, 2011.

[5] W.-W. Zhong, F.-M. Liu, and W.-P. Chen, "Effect of ammonia/zinc nitrate molar ratio on structural and optical properties of Al and Sb codoped ZnO nanorod ordered array thin films," *Journal of Alloys and Compounds*, vol. 531, pp. 59–63, 2012.

[6] S. H. Kim, A. Umar, Y. K. Park, J.-H. Kim, E. W. Lee, and Y. B. Hahn, "Non-catalytic growth of high-aspect-ratio Sb-doped ZnO nanowires by simple thermal evaporation process: structural and optical properties," *Journal of Alloys and Compounds*, vol. 479, no. 1-2, pp. 290–293, 2009.

[7] B. Li and Y. Wang, "Facile synthesis and enhanced photocatalytic performance of flower-like ZnO hierarchical microstructures," *Journal of Physical Chemistry C*, vol. 114, no. 2, pp. 890–896, 2010.

[8] D. W. Zeng, C. S. Xie, B. L. Zhu et al., "Controlled growth of ZnO nanomaterials via doping Sb," *Journal of Crystal Growth*, vol. 266, no. 4, pp. 511–518, 2004.

[9] X. Jia, H. Fan, M. Afzaal, X. Wu, and P. O'brien, "Solid state synthesis of tin-doped ZnO at room temperature: characterization and its enhanced gas sensing and photocatalytic properties," *Journal of Hazardous Materials*, vol. 193, pp. 194–199, 2011.

[10] E. Pál, V. Hornok, A. Oszkó, and I. Dékány, "Hydrothermal synthesis of prism-like and flower-like ZnO and indium-doped ZnO structures," *Colloids and Surfaces A*, vol. 340, no. 1–3, pp. 1–9, 2009.

[11] B. Wang, M. J. Callahan, C. Xu, L. O. Bouthillette, N. C. Giles, and D. F. Bliss, "Hydrothermal growth and characterization of indium-doped-conducting ZnO crystals," *Journal of Crystal Growth*, vol. 304, no. 1, pp. 73–79, 2007.

[12] C. Jing, Y. Jiang, W. Bai, J. Chu, and A. Liu, "Synthesis of Mn-doped ZnO diluted magnetic semiconductors in the presence of ethyl acetoacetate under solvothermal conditions," *Journal of Magnetism and Magnetic Materials*, vol. 322, no. 16, pp. 2395–2400, 2010.

[13] C. Karunakaran, P. Gomathisankar, and G. Manikandan, "Preparation and characterization of antimicrobial Ce-doped ZnO nanoparticles for photocatalytic detoxification of cyanide," *Materials Chemistry and Physics*, vol. 123, no. 2-3, pp. 585–594, 2010.

[14] Powder Diffract. File, JCPDS Internat. Centre Diffract. Data, PA 19073–3273, U.S.A., 2001.

[15] M. Dondi, F. Matteucci, and G. Cruciani, "Zirconium titanate ceramic pigments: crystal structure, optical spectroscopy and technological properties," *Journal of Solid State Chemistry*, vol. 179, no. 1, pp. 233–246, 2006.

[16] O. Lupan, L. Chow, L. K. Ono et al., "Synthesis and characterization of ag- or sb-doped zno nanorods by a facile hydrothermal route," *Journal of Physical Chemistry C*, vol. 114, no. 29, pp. 12401–12408, 2010.

[17] Y. Yang, J. Qi, Q. Liao, Y. Zhang, L. Tang, and Z. Qin, "Synthesis and characterization of Sb-doped ZnO nanobelts with single-side zigzag boundaries," *Journal of Physical Chemistry C*, vol. 112, no. 46, pp. 17916–17919, 2008.

[18] P. Li, S. Wang, J. Li, and Y. Wei, "Structural and optical properties of Co-doped ZnO nanocrystallites prepared by a one-step solution route," *Journal of Luminescence*, vol. 132, no. 1, pp. 220–225, 2012.

[19] R. B. Peterson, C. L. Fields, and B. A. Gregg, "Epitaxial chemical deposition of ZnO nanocolumns from NaOH solutions," *Langmuir*, vol. 20, no. 12, pp. 5114–5118, 2004.

[20] Y. Zeng, T. Zhang, L. Wang, and R. Wang, "Synthesis and ethanol sensing properties of self-assembled monocrystalline ZnO nanorod bundles by poly(ethylene glycol)-assisted hydrothermal process," *Journal of Physical Chemistry C*, vol. 113, no. 9, pp. 3442–3448, 2009.

[21] Z. L. Wang, "Novel zinc oxide nanostructures discovery by electron microscopy," *Journal of Physics*, vol. 26, no. 1, pp. 1–6, 2006.

[22] A. Phuruangrat, T. Thongtem, B. Kuntalue, and S. Thongtem, "Microwave-assisted synthesis and characterization of rose-like and flower-like zinc oxide nanostructures," *Journal of Ovonic Research*, vol. 7, pp. 107–113, 2011.

[23] J.-S. Liu, J.-M. Cao, Z.-Q. Li, G.-B. Ji, and M.-B. Zheng, "A simple microwave-assisted decomposing route for synthesis of ZnO nanorods in the presence of PEG400," *Materials Letters*, vol. 61, no. 22, pp. 4409–4411, 2007.

[24] Y. Lei, G. Zhao, M. Liu, Z. Zhang, X. Tong, and T. Cao, "Fabrication, characterization, and photoelectrocatalytic application of ZnO nanorods grafted on vertically aligned TiO_2 nanotubes," *Journal of Physical Chemistry C*, vol. 113, no. 44, pp. 19067–19076, 2009.

[25] H. Li, D. Wang, H. Fan, T. Jiang, X. Li, and T. Xie, "Synthesis of ordered multivalent Mn-TiO_2 nanospheres with tunable size: a high performance visible-light photocatalyst," *Nano Research*, vol. 4, no. 5, pp. 460–469, 2011.

[26] H. Chang and M.-H. Tsai, "Synthesis and characterization of ZnO nanoparticles having prism shape by a novel gas condensation process," *Reviews on Advanced Materials Science*, vol. 18, no. 8, pp. 734–743, 2008.

[27] J. Zhao, L. Wang, X. Yan et al., "Structure and photocatalytic activity of Ni-doped ZnO nanorods," *Materials Research Bulletin*, vol. 46, no. 8, pp. 1207–1210, 2011.

[28] J. H. Zeng, B. B. Jin, and Y. F. Wang, "Facet enhanced photocatalytic effect with uniform single-crystalline zinc oxide nanodisks," *Chemical Physics Letters*, vol. 472, no. 1–3, pp. 90–95, 2009.

[29] R. Jain and S. Sikarwar, "Photodestruction and COD removal of toxic dye erioglaucine by TiO_2-UV process: influence of operational parameters," *International Journal of Physical Sciences*, vol. 3, no. 12, pp. 299–305, 2008.

[30] J. Chanathaworn, C. Bunyakan, W. Wiyaratn, and J. Chungsiriporn, "Photocatalytic decolorization of basic dye by TiO_2 nanoparticle in photoreactor," *Songklanakarin Journal of Science and Technology*, pp. 203–210, 2012.

Available online at www.sciencedirect.com

ScienceDirect

Ceramics International 40 (2014) 9069–9076

CERAMICS INTERNATIONAL

www.elsevier.com/locate/ceramint

Controlling morphologies and growth mechanism of hexagonal prisms with planar and pyramid tips of ZnO microflowers by microwave radiation

Anukorn Phuruangrat[a,*], Titipun Thongtem[b], Somchai Thongtem[c,d,**]

[a]Department of Materials Science and Technology, Faculty of Science, Prince of Songkla University, Hat Yai, Songkhla 90112, Thailand
[b]Department of Chemistry, Faculty of Science, Chiang Mai University, Chiang Mai 50200, Thailand
[c]Department of Physics and Materials Science, Faculty of Science, Chiang Mai University, Chiang Mai 50200, Thailand
[d]Materials Science Research Center, Faculty of Science, Chiang Mai University, Chiang Mai 50200, Thailand

Received 6 December 2013; received in revised form 20 January 2014; accepted 26 January 2014
Available online 31 January 2014

Abstract

Flower-like ZnO microstructures of hexagonal prisms with planar and hexagonal pyramid tips were successfully synthesized by a microwave radiation method. The precursor solutions were synthesized from zinc nitrate hexahydrate ($Zn(NO_3)_2 \cdot 6H_2O$) and hexamethylenetetramine (HMT) at pH 9 and 13. The as-synthesized products were pure hexagonal wurtzite ZnO microstructured flowers of hexagonal prisms with planar tips at pH 9 and of hexagonal prisms with hexagonal pyramid tips at pH 13. Sharp and strong optical phonon Raman-active mode of E_{2H} was detected at 438 cm^{-1}. The excitonic characters of the absorption peaks were also detected at 397 nm for the first product and 384 nm for the second one, and the decolorization efficiency of RhB by Hg-lamp irradiation for 140 min was 77% and 87%, respectively.

Keywords: Flower-like hexagonal ZnO microstructure; Hexagonal prisms; Hexagonal pyramids; Microwave radiation

1. Introduction

Among semiconducting materials, wurtzite hexagonal ZnO with 3.37 eV direct band gap and 60 meV exciton binding energy is an important functional material as a short-wavelength optical device due to its unique piezoelectricity, pyroelectricity and photocatalysis, including light emitting diodes (LEDs), laser diodes (LDs), transparent conducting electrodes for solar cells, surface acoustic filters, UV lasers and chemical/biological sensors [1–6]. Different morphologies of ZnO structures such as nanorods [3–5], hexagonal cones [6], hollow spheres [7,8], flowers [2,9,10], nanoparticles [11], dendrites [12], hexagonal disks/plates [13–15] and nanotubes [16–19] have been synthesized both by chemical and physical methods such as sol–gel process [1], hydrothermal process [2,3,14], thermal evaporation process [4], ultrasonic-assisted synthesis [7–12], carbothermal reduction [15], plasma-assisted molecular beam epitaxy [18,19], microwave radiation [20] and chemical vapor deposition [21–23].

In case of physical processes, they perform under relatively harsh conditions, requiring high temperature, low pressure (vacuum) and a high efficiency instrument with elaborate design. They are quite difficult to apply for large-scale and industrial production. Practically, chemical syntheses in solutions known as solution methods can be enlarged for large-scale production without using catalysts and additives with better crystalline quality, preferably at low growth temperature. The processes are more convenient, inexpensive and challenge nano- and micro-structured products with morphological control and crystalline evolution.

Generally, conventional heating is an energy transferred process from outside to inside of solutions or from the higher to lower temperature by conduction process. There must be physical contact between internal surfaces of the reaction vessels and the mixtures inside. In case of microwave radiation, it is an increasingly popular method used for the synthesis of materials. Microwave radiation is composed of vibrating electric field that can penetrate the reaction vessels. Molecules, ions and dipoles of the mixtures contained in the

*Corresponding author. Tel.: +66 74 288374; fax +66 74 288395.
**Corresponding author at: Materials Science Research Center, Faculty of Science, Chiang Mai University, Chiang Mai 50200, Thailand. Tel.: +66 53 941924; fax +66 53 943445.
E-mail addresses: phuruangrat@hotmail.com (A. Phuruangrat), schthongtem@yahoo.com (S. Thongtem).

0272-8842/$ - see front matter © 2014 Elsevier Ltd and Techna Group S.r.l. All rights reserved.
http://dx.doi.org/10.1016/j.ceramint.2014.01.120

vessels rotate and vibrate in accordance with the vibration of the electric field, and cause a rise in the temperature. Heat is directly transferred to nearby mixtures. Temperature distribution of the entire solution mixtures is homogeneous. The main advantage of microwave-assisted synthesis is the uniform heating of reactants. The process can generate localized instantaneous hot spots at reaction sites, consume shorter reaction time, selectively form specific morphology, reduce energy consumption and produce high product yield [24,25].

In this research, a facile synthesis of flower-like ZnO structures comprising petals of hexagonal prisms and hexagonal pyramid tips by microwave radiation is reported. Phase, morphologies and photocatalytic performance of the products were characterized by a series of techniques. These results show that both the flower-like ZnO products can be used as superior photocatalysts with high efficiency for decomposing organic dyes.

2. Experiment

All chemicals were purchased from Sigma-Aldrich Corporation and used without further purification. To start the procedure, 0.005 mol zinc nitrate hexahydrate ($Zn(NO_3)_2 \cdot 6H_2O$) and 0.010 mol hexamethylenetetramine (HMT) were dissolved in 100 ml de-ionized water under stirring at room temperature. Subsequently, 3 M sodium hydroxide solution was added to each of the 100 ml solutions until reaching the pH values of 9 and 13. The two solutions with the pH 9 and 13 were transferred into a microwave oven and heated at 180 W for 60 min (96 °C). At the end of microwaving, white precipitates were synthesized, washed with methanol several times and dried at 80 °C for 24 h to form two powder products.

The as-synthesized products were characterized by Philips X'Pert MPD X-ray powder diffraction (XRD) using a Cu Kα radiation at 45 kV and 35 mA with a scanning rate of 0.04 deg/s in the 2θ range from 20° to 60°. Fourier transform infrared (FTIR) spectra were recorded on a PerkinElmer RX FTIR spectrophotometer with KBr as a diluting agent and operated in the range of 400–4000 cm^{-1} with the resolution of 4 cm^{-1}. A Raman spectrometer (HORIBA Jobin Yvon T64000) was operated using 50 mW of 514.5 nm wavelength Ar green laser. SEM images were taken through a scanning electron microscope (SEM, JEOL JSM-6335F) at 20 kV. TEM images of the products were taken using a JEOL JEM-2010 transmission electron microscope (TEM) with an accelerating voltage of 200 kV. UV–visible absorption was carried out through a quartz cell on a Lambda 25 PerkinElmer spectrophotometer.

Photocatalytic activities of the as-synthesized products were tested by measuring the degradation of rhodamine B (RhB) in aqueous solutions under UV radiation as the light source. Each 0.1 g of photocatalyst was suspended in 75 ml of 2.5 mg/l RhB solution, which was magnetically stirred for 30 min in dark to establish an adsorption/desorption equilibrium of RhB on the surface of each photocatalyst. Then light was turned on to initiate photocatalytic reaction. The solutions were analyzed by a Lambda 25 PerkinElmer spectrometer using a 450 W Xe-lamp with 554 nm wavelength. The decolorization efficiency (%) was calculated using the following equation:

$$\text{Decolorization efficiency (\%)} = \frac{C_0 - C}{C_0} \times 100 \quad (1)$$

where C_0 and C are the initial and final concentrations of RhB.

3. Results and discussion

Phase of the as-synthesized ZnO products was characterized by the XRD as shown in Fig. 1. All the diffraction peaks at 2θ of 31.81°, 34.47°, 36.31°, 47.61° and 56.65° were respectively indexed to the (100), (002), (101), (102) and (110) planes of pure hexagonal wurtzite ZnO structure of the JCPDS database no. 36-1451 [26]. No impurities were detected in these products. The characteristic peaks were high in intensity and narrow in spectral width, implying that the products were at high degrees of crystallinity.

Raman spectra of hexagonal wurtzite ZnO structure belong to the C_{6v}^4 or $P6_3mc$ space group, with 12 phonon modes and two formula units per primitive cell. Therefore, there are nine optical and three acoustic phonon modes, belonging to three longitudinal-optical (LO), six transverse-optical (TO), one longitudinal-acoustic (LA) and two transverse -acoustic (TA) modes. Different symmetries involve the vibrational Raman active appearing in the spectra. Changes in lattice spacing and chemical environment are able to shift their vibrational frequencies. According to group theory prediction, the vibration of optical phonons at the Γ point of Brillouin zone is $\Gamma_{opt} = 1A_1 + 1E_1 + 2E_2$, where A_1 and E_1 are active in both Raman and infrared (IR) and E_2 is active in only Raman. The polar characteristics of the A_1 and E_1 are split into LO and TO components due to the macroscopic electric fields associated with optical phonons. Fig. 2 shows typical Raman-scattering

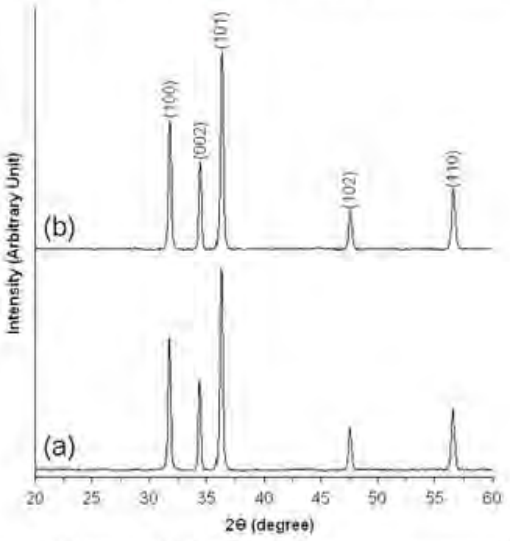

Fig. 1. XRD patterns of ZnO synthesized in the solutions containing $Zn(NO_3)_2 \cdot 6H_2O$ and HMT at pH (a) 9 and (b) 13.

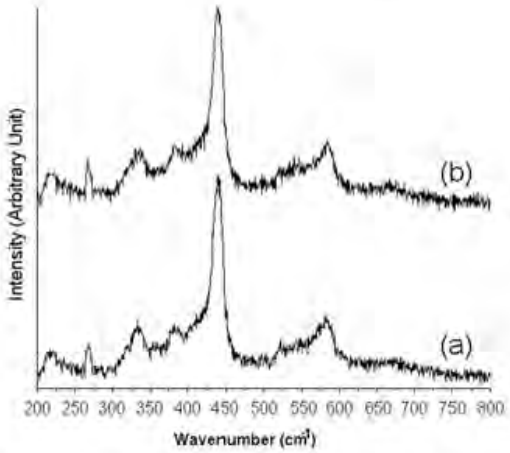

Fig. 2. Raman spectra of ZnO synthesized in the solutions containing Zn $(NO_3)_2 \cdot 6H_2O$ and HMT at pH (a) 9 and (b) 13.

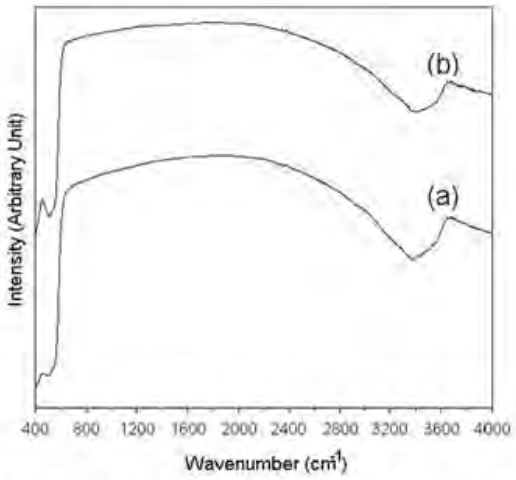

Fig. 3. FTIR spectra of ZnO synthesized in the solutions containing Zn $(NO_3)_2 \cdot 6H_2O$ and HMT at pH (a) 9 and (b) 13.

spectra with Ar green laser line as the excitation source for the as-synthesized ZnO products at the wavenumber range of 200–800 cm^{-1}. Intense peaks at 438 cm^{-1} were specified as the E_{2H} mode, and a very weak peak at 585 cm^{-1} as the E_{1L} mode. The presence of Raman-active optical phonon E_{2H} mode was caused by the wurtzite hexagonal phase of ZnO, and the E_{1L} mode was caused by the structural defects of oxygen vacancies, zinc interstitials, free carriers and impurities. The E_{2L} low frequency mode at approximately 100 cm^{-1} was out of the range of the present analysis. In addition, two very weak peaks at 332 cm^{-1} and 381 cm^{-1} were also detected which was indicated as the E_{2H}–E_{2L} multi-phonon and A_{1T} modes, respectively [4,10,14,20,27].

FTIR spectra of ZnO products diluted by mixing with KBr at the 1:10 ratio for the analysis in the range of 400–4000 cm^{-1} at room temperature are shown in Fig. 3. They show absorption band at around 521 cm^{-1} and a broad band at 3200–3600 cm^{-1}. The absorption at 521 cm^{-1} is a typical characteristic band of wurtzite hexagonal ZnO structure [28,29]. No other peak was detected, implying that the as-synthesized products were of pure ZnO phase. The broad band at 3200–3600 cm^{-1} belongs to water absorption on the surface of ZnO products.

ZnO wurtzite crystal structure can be described as hexagonal close packing of O and Zn atoms in $P6_3mc$ space group with Zn atoms in tetrahedral sites. There is no center of inversion in the wurtzite structure. Thus an inherent asymmetry along the *c*-axis is present, which allows the anisotropic growth of the crystal along the [0001] direction. A typical crystal exhibits a basal polar O $(000\bar{1})$ face and a top tetrahedral corner-exposed polar Zn (0001) face, leading to their difference in reactivity. Zn and O atoms are located in an alternating manner in the $(10\bar{1}0)$ planes parallel to the *c*-axis. Structurally, ZnO has three types of rapid growth directions: $\langle 2\bar{1}\,\bar{1}0\rangle$ ($\pm[2\bar{1}\,\bar{1}0]$, $\pm[\bar{1}2\bar{1}0]$, $\pm[\bar{1}\,\bar{1}20]$); $\langle[01\bar{1}0]\rangle$, ($\pm[01\bar{1}0]$, $\pm[10\bar{1}0]$, $\pm[1\bar{1}00]$); and $\pm[0001]$. Together with the polar surfaces of atomic termination, ZnO exhibits a wide range of novel structures grown by tuning the growth rate along these directions. One of the most profound factors in determining ZnO morphology involves the relative surface activities of different growth facets under given conditions. Macroscopically, the crystal has different kinetic parameters for different crystalline planes under controlled growth conditions. Following an initial period of nucleation, crystallites will commonly develop into three-dimensional particles with well-defined and low-index crystallographic faces [30–32].

The morphologies of the as-synthesized ZnO products were investigated in detail using SEM. At pH 9, SEM image of Fig. 4 (a) gives a general view of the product morphology over a large area. The product consists of a large number of microstructured ZnO flowers with the size of 2–3 μm. For a medium magnification SEM image (Fig. 4(b)), the microstructured ZnO flowers were composed of microrods in the shape of hexagonal prisms grown out of ZnO cores. At high magnification, SEM image (Fig. 4(c)) reveals that each microrod is a hexagonal-facet prism with a smooth planar tip. Each hexagonal prism is 1–2 μm long and 50–130 nm in diameter. Clearly, each microrod formed is a solid prism with its tip similar to a hexagon and its six equivalent vertical side walls in the shape of rectangle. Moreover, each of the as-grown microrods contains the (0001) top facet enclosed with six crystallographic planes of $(10\bar{1}0)$, $(01\bar{1}0)$, $(\bar{1}100)$, $(\bar{1}010)$, $(0\bar{1}10)$ and $(1\bar{1}00)$ as shown in Fig. 5(a). The exact hexagonal surfaces confirmed the epitaxial growth and therefore the single crystalline nature of the as-grown microrods [31–33]. At pH 13, the SEM images are shown in Fig. 4(d)–(f). At low magnification, the product is a full array of uniform flower-shaped ZnO with the size range of 2–3 μm. For the medium magnification SEM image, the flower-shaped ZnO was composed of a number of petals of perfectly hexagonal prisms with hexagonal pyramid tips. Their length and diameter were 1.5 μm and 0.3 μm, respectively. It should be noted that all hexagonal prisms with pyramid tips grew out of the same origin cores to set

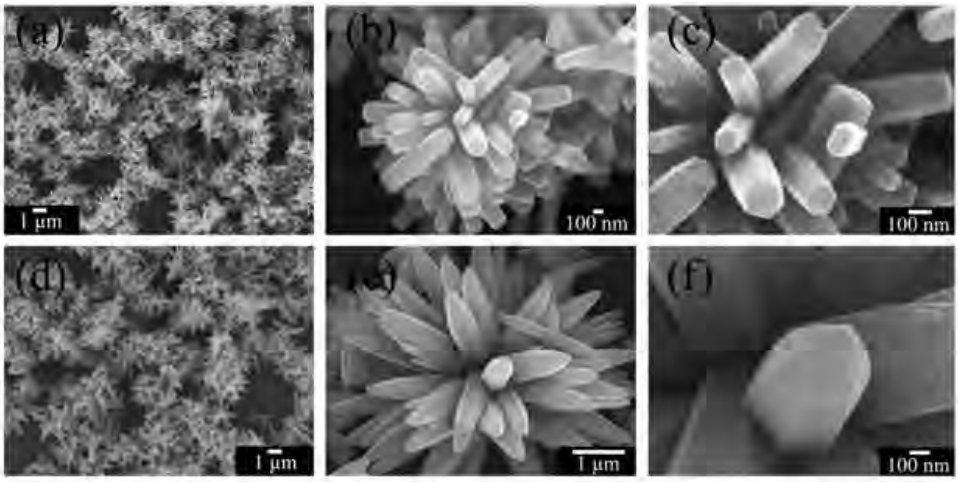

Fig. 4. SEM images of ZnO synthesized in the solutions containing $Zn(NO_3)_2 \cdot 6H_2O$ and HMT at pH (a–c) 9 and (d–f) 13.

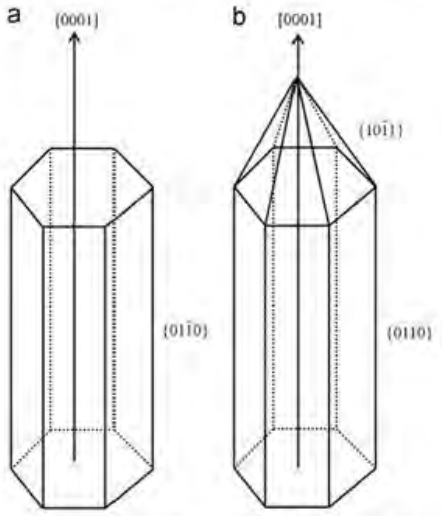

Fig. 5. Schematic illustration of the growth models for hexagonal prisms with (a) planar and (b) hexagonal pyramid tips.

up a flower-shaped morphology. At high magnification, the image shows a hexagonal prism with hexagonal pyramid tip. Each pyramid was composed of six triangles on top forming as the $\pm\{10\bar{1}1\}$ polar planes, which were inferred from wurtzite ZnO lattice structure. The six $\pm\{10\bar{1}1\}$ polar planes are $(10\bar{1}1)$, $(1\bar{1}01)$, $(01\bar{1}1)$, $(\bar{1}011)$, $(\bar{1}101)$ and $(01\bar{1}1)$ [34]. Assemblies of the microrods were likely to be initiated by long-range electrostatic interaction and short-range chemical bonding, leading to the observed superstructure. The $\pm\{10\bar{1}1\}$ planes were polar surfaces which could be terminated as zinc or oxygen faces. The electrostatic force can lead to the freestanding microrods with sharp tips on the $\pm\{10\bar{1}1\}$ planes to be very active [30,31,34,36]. Some microrods attract charged ions such as OH^- in aqueous solution onto the polar pyramid faces and the remains attract others onto the opposite polar planes. In the end, ZnO hexagonal prisms with hexagonal pyramid tips were produced as shown in Fig. 5(b).

Fig. 6 shows TEM images and SAED patterns of the as-synthesized hexagonal prism flower-shaped ZnO microstructure. An individual flower-like ZnO microstructure with perfect geometry was the assembly of uniform hexagonal prism microrods. The flower-like ZnO assemblies consist of well-aligned hexagonal prisms of straight and uniform microrods with 100 nm wide and about 600 nm long, growing along the [0001] direction. SAED patterns of broken hexagonal prism ZnO microrods on the areas of 1 and 2 were characterized. The bright diffraction spots of the SAED patterns indicate that the individual hexagonal prisms of flower-like ZnO microstructure were single crystal. Both SAED patterns were specified as the $(11\bar{2}0)$, $(11\bar{2}2)$ and (0002) planes with the $[1\bar{1}00]$ direction as zone axis of the hexagonal ZnO phase, in accordance with the above XRD analysis.

Fig. 7 shows TEM images of the hexagonal prisms with sharp tips of ZnO microstructure, in accordance with the above SEM characterization. It should be noted that the flower-shaped ZnO was composed of a number of perfectly hexagonal prisms with sharp tips grown out of the same origin core to set up ZnO flower-shaped morphology with its petals of hexagonal prisms with sharp tips. At high magnification, the hexagonal pyramid flower-shaped ZnO microstructure was composed of smooth and clean surfaces of microrod petals with different orientated tips directing in the [0001] direction. Single crystalline ZnO microrods were also characterized by SAED at the areas of 1 and 2, which show patterns of the symmetrical stripes of bright spots rather than bright spots in circles of the same center. Both patterns were indexed to be hexagonal ZnO with the $[\bar{1}100]$ direction as zone axis.

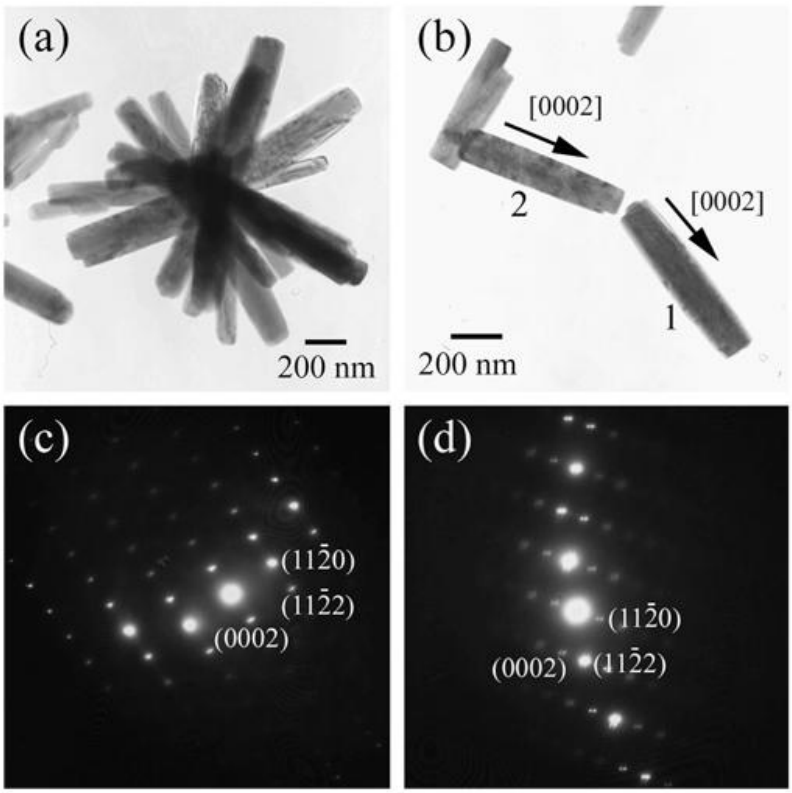

Fig. 6. (a, b) TEM images and (c, d) SAED patterns of hexagonal prisms of flower-like ZnO microstructure synthesized in the solution with pH 9.

The formation of ZnO microflowers which are composed of petals in the shapes of hexagonal prisms with planar and pyramid tips can be explained by the following. The precipitation of ZnO particles in aqueous solution is rather complex. Generally, the size and morphology of ZnO particles are controlled by the chemical state of Zn^{2+} ions in the solution. Thermodynamic and kinetic factors can play different roles in the precipitation process. The chemical state of Zn^{2+} ions is strongly controlled by the pH of solution and anionic type. By gradually adding NaOH solution to Zn(II)-salt solution, $Zn(OH)_4^{2-}$ complexes originated at pH 9. Precipitation of ZnO from $Zn(OH)_4^{2-}$ complexes can be written by the following reaction:

$$Zn^{2+} + 4OH^- \rightarrow Zn(OH)_4^{2-} \quad (2)$$

$$Zn(OH)_4^{2-} \rightarrow ZnO + H_2O + 2OH^- \quad (3)$$

Due to the fewer nuclei and a large number of growth units, $[Zn(OH)_4]^{2-}$ complexes are able to easily adsorb on different sites of ZnO nanorods (seeds). The positively charged Zn-(0001) surfaces are the most reactive. Thus OH^- ions may stabilize the positive charge of the Zn-(0001) surfaces to some extent, allowing rapid growth along the [0001] direction, leading to the formation of ZnO hexagonal prisms with rod-like crystal. Comparing with ZnO microflowers of hexagonal pyramid tips, $Zn(NO_3)_2 \cdot 6H_2O$ produced predominant aqueous species at higher concentration of NaOH solution with pH 13 such as $Zn(OH)_3^{1-}$, $Zn(OH)_4^{2-}$ and ZnO_2^{2-} zincate ions. At high pH, these species are very stable, leading to increase in the dissolution of $Zn(OH)_2$ and ZnO at room temperature. The stability of these complexes decreases with increase in the temperature during microwaving, resulting in the formation of ZnO solid. Growth mechanism of ZnO microflowers with the petals of hexagonal pyramids can be understood on the basis of the following reactions and crystalline characteristics of wurtzite ZnO. The structure of ZnO single crystal can be described as a number of alternating surfaces of coordinated O^{2-} and Zn^{2+} with oppositely charged ions, made of Zn rich positive surfaces and oxygen rich negative surfaces, which can attract new ZnO and opposite charged species. Due to the crystalline characteristics of ZnO, growth rates (R) of different surfaces are in sequence as follows: $R(0001) > R(\bar{1}01\bar{1}) > R(\bar{1}010) > R(\bar{1}011) > R(000\bar{1})$. For the formation of ZnO microflowers with petals of hexagonal pyramids, the polar (0001) and six $(10\bar{1}1)$ surfaces make up hexagonal pyramids. The bases of hexagonal pyramids consist of end surfaces of O terminated $(000\bar{1})$ and side surfaces of O terminated $(10\bar{1}1)$, which are all polar surfaces. For wurtzite ZnO crystal, the O terminated $(000\bar{1})$ polar surfaces are

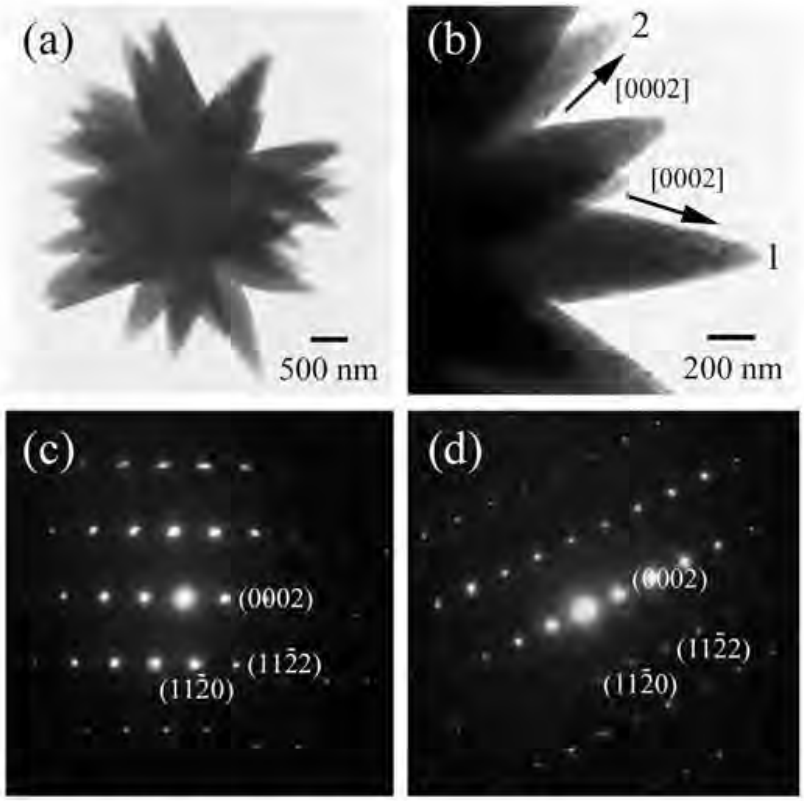

Fig. 7. (a, b) TEM images and (c, d) SAED patterns of hexagonal pyramids of flower-like ZnO microstructure synthesized in the solution with pH 13.

generally thought to be inert compared with the Zn terminated (0001) polar surfaces. During crystalline growth, the polar surfaces with the lowest energy (atoms/ions prefer to reside on the lowest energy level) are of the most rapid growth and fade away. Thus, growth of the hexagonal pyramids is along the [0001] direction or Zn polarized direction. Possibly, surface energies of polar surfaces are raised or passivated by oppositely charged ions. At high pH value, a strong electrostatic interaction between the ions and polar surfaces is created, leading to the increase in surface energies of the (0001) and (10$\bar{1}$1) polar surfaces in comparison with those of other crystalline surfaces. Thus, growth rates of these polar surfaces slow down and the polar surfaces appear as external surfaces on sharp tips of the hexagonal prisms with pyramid tips [28,36–41].

ZnO powders were dispersed in analytical grade ethanol for optical studying. Optical properties of the as-synthesized products were investigated through UV–visible absorption at room temperature as shown in Fig. 8. Their absorption spectra are broad over the range of 300–500 nm for flower-like ZnO microstructures of hexagonal prisms with planar tips and strong absorption band in the range of 350–550 nm for flower-like ZnO microstructures of hexagonal pyramids. They are excitonic characters with the absorption peaks at 397 nm with calculated band-gap of 3.12 eV for hexagonal prisms, and 384 nm with calculated band-gap of 3.23 eV for hexagonal pyramids, attributed to band edge absorption of the wurtzite hexagonal pure ZnO products [35,36,42]. These calculated band gaps were a little different from their bulk with E_g=3.37 eV [43].

In this research, the photocatalytic degradation efficiency of 75 ml of 2.5 mg/l RhB solutions was used to evaluate the photocatalytic activities under UV radiation of Hg lamp. Fig. 9 shows the decolorization efficiency of two ZnO microstructures under UV illumination for 140 min. This shows that ZnO microstructures were able to decolorize RhB to about 55% within 18 min. When the time was lengthened to 140 min, the decolorization efficiency of RhB by hexagonal pyramids of flower-like ZnO was 87% and by hexagonal prisms of flower-like ZnO was 77%. These results show that the hexagonal pyramids of flower-like ZnO exhibited the highest photocatalytic efficiency, which might be attributed to the unique structure, to absorb large fraction of UV light. Contrarily, the hexagonal prisms of flower-like ZnO with relatively less surface area could decrease the UV light utilization rate and reduce the photocatalytic activity, resulting in lower decolorization efficiency of RhB. These imply that the photocatalysis is highly dependent on UV light radiation. When photon

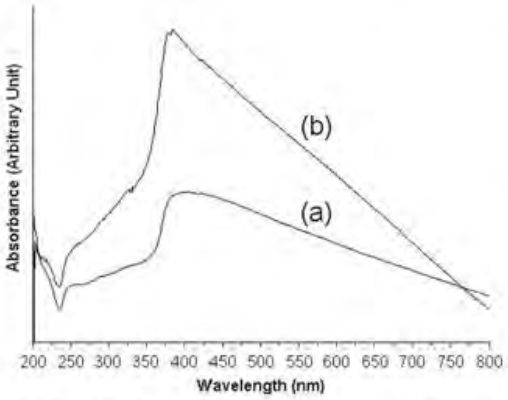

Fig. 8. UV–visible absorption of (a) hexagonal prisms and (b) hexagonal pyramids of flower-like ZnO microstructures.

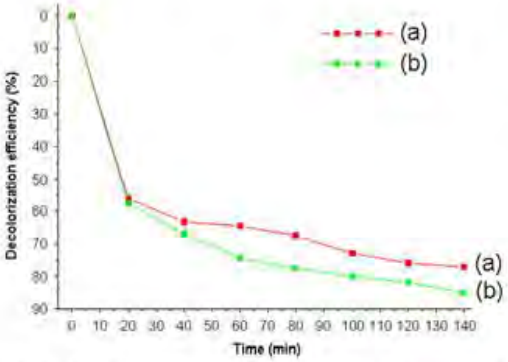

Fig. 9. Decolorization efficiency of RhB by (a) hexagonal prisms and (b) hexagonal pyramids of flower-like ZnO microstructures.

energy of the light source is greater than or equal to the band gap of ZnO, the photocatalysis will be activated. ZnO microstructures generate electron–hole pairs at the tail states of conduction and valence bands. The photogenerated electrons diffuse to the adsorbed RhB molecules on the photocatalytic surfaces. The excited electrons from the photocatalytic conduction bands enter into the molecular structure of RhB and disrupt its conjugated system, leading to the complete degradation of RhB. Holes in the valence bands react with water to generate $OH^{\bullet}$ and can be used for oxidation of the organic dye [44–46].

$$ZnO + h\nu \rightarrow ZnO(e^{-}_{CB} + h^{+}_{VB}) \quad (4)$$

$$H_2O + h^{+}_{VB} \rightarrow H^{+} + OH^{\bullet} \quad (5)$$

$$dye + OH^{\bullet} \rightarrow \text{oxidation products} \quad (6)$$

Reaction rate of photo-degradation of RhB by ZnO under UV–visible light was calculated using the normalized concentration. The $\ln C_0/C$ vs reaction time was plotted and apparent rate constant (k_a) values were determined from their slopes. The linearity of the plots with correlation coefficient $R^2 \rightarrow 1$ suggests that the decolorization reaction of RhB follows pseudo-first-order kinetics [43,45,47]. The reaction rate constants of RhB degradation of hexagonal prisms and hexagonal pyramids of flower-like ZnO microstructures are 5.44×10^{-3} and 8.68×10^{-3} min^{-1}, respectively. Clearly, hexagonal pyramids of the flower-like ZnO microstructure is the most appropriate for using as a potential photocatalyst under UV light irradiation.

4. Conclusions

In summary, hexagonal prisms and hexagonal pyramids of flower-like ZnO microstructures were successfully synthesized by a microwave-assisted radiation process. The phase, molecular vibration, morphology and optical properties of the as-synthesized ZnO products were characterized by XRD, Raman spectroscopy, FTIR, EM and UV–visible spectroscopy. In this research, the as-synthesized products were pure wurtzite hexagonal ZnO structure: hexagonal prisms of flower shape at pH 9 and hexagonal pyramids of flower shape at pH 13. The products show absorption peaks at 397 nm (3.12 eV) for hexagonal prism ZnO microstructure and 384 nm (3.23 eV) for hexagonal pyramid ZnO microstructure, which are almost consistent with that of their bulk. In this research, hexagonal pyramid flower-like ZnO exhibited the best photocatalytic activity for photodegradation of RhB with the reaction rate constant of 8.68×10^{-3} min^{-1}.

Acknowledgment

We wish to thank the Thailand Research Fund (TRF) for providing financial support through the TRF Research Contract MRG5580112.

References

[1] S. Suwanboon, R. Tanattha, R. Tanakorn, Fabrication and properties of nanocrystalline zinc oxide thin films prepared by sol–gel method, J. Sci. Technol. 30 (2008) 65–69.
[2] R. Yi, N. Zhang, H. Zhou, R. Shi, G. Qiu, X. Liu, Selective synthesis and characterization of flower-like ZnO microstructures via a facile hydrothermal route, Mater. Sci. Eng. B 153 (2008) 25–30.
[3] S.J. Kim, H.H. Kim, J.B. Kwon, J.G. Lee, B.H. O, S.G. Lee, E.H. Lee, S.G. Park, Novel fabrication of various size ZnO nanorods using hydrothermal method, Microelectron. Eng. 87 (2010) 1534–1536.
[4] A. Umar, S.H. Kim, J.H. Kim, Y.B. Hahn, Structural and optical properties of ZnO nanostructures grown on silicon substrate by thermal evaporation process, Mater. Lett. 62 (2008) 167–171.
[5] J. Zhao, Z.G. Jin, X.X. Liu, Z.F. Liu, Growth and morphology of ZnO nanorods prepared from $Zn(NO_3)_2$/NaOH solutions, J. Eur. Ceram. Soc. 26 (2008) 3745–3752.
[6] X. Ren, D. Han, D. Chen, F. Tang, Large-scale synthesis of hexagonal cone-shaped ZnO nanoparticles with a simple route and their application to photocatalytic degradation, Mater. Res. Bull. 42 (2007) 807–813.
[7] C. Deng, H. Hu, G. Shao, C. Han, Facile template-free sonochemical fabrication of hollow ZnO spherical structures, Mater. Lett. 64 (2010) 852–855.
[8] X. Jia, H. Fan, F. Zhang, L. Qin, Using sonochemistry for the fabrication of hollow ZnO microspheres, Ultrason. Sonochem. 17 (2010) 284–287.

[9] M. Mazloumi, S. Zanganeh, A. Kajbafvala, P. Ghariniyat, S. Taghavi, A. Lak, M. Mohajerani, S.K. Sadrnezhaad, Ultrasonic induced photoluminescence decay in sonochemically obtained cauliflower-like ZnO nanostructures with surface 1D nanoarrays, Ultrason. Sonochem. 16 (2009) 11–14.

[10] T. Thongtem, A. Phuruangrat, S. Thongtem, Effect of basicity on the morphologies of ZnO produced using a sonochemical method, Curr. Appl. Phys. 9 (2009) S197–S200.

[11] A.E. Kandjani, M.F. Tabriz, B. Pourabbas, Sonochemical synthesis of ZnO nanoparticles: the effect of temperature and sonication power, Mater. Res. Bull. 43 (2008) 645–654.

[12] X. Hou, F. Zhou, Y. Sun, W. Liu, Ultrasound-assisted synthesis of dentritic ZnO nanostructure in ionic liquid, Mater. Lett. 61 (2007) 1789–1792.

[13] K. Ada, M. Gökgöz, M. Önal, Y. Sarıkaya, Preparation and characterization of a ZnO powder with the hexagonal plate particles, Powder Technol. 181 (2008) 285–291.

[14] J. Lee, J. Chae, K. Nahm, M. Kang, Synthesis of nanometer-sized hexagonal disk-shaped ZnO in formic acid using a hydrothermal method and its optical properties, J. Ind. Eng. Chem. 15 (2009) 645–648.

[15] P.F. Lin, C.Y. Ko, W.T. Lin, C.T. Lee, Effects of processing parameters on ultraviolet emission of In-doped ZnO nanodisks grown by carbothermal reduction, Mater. Lett. 61 (2007) 1767–1770.

[16] Z. Liu, C. Liu, J. Ya, E. Lei, Controlled synthesis of ZnO and TiO_2 nanotubes by chemical method and their application in dye-sensitized solar cells, Renew. Energy 36 (2011) 1177–1181.

[17] Y.J. Chen, C.L. Zhu, G. Xiao, Ethanol sensing characteristics of ambient temperature sonochemically synthesized ZnO nanotubes, Sens. Actuat. B 129 (2008) 639–642.

[18] J.F. Yan, Y.M. Lu, H.W. Liang, Y.C. Liu, B.H. Li, X.W. Fan, J.M. Zhou, Growth and properties of ZnO nanotubes grown on Si(111) substrate by plasma-assisted molecular beam epitaxy, J. Cryst. Growth 280 (2005) 206–211.

[19] H.W. Liang, Y.M. Lu, D.Z. Shen, B.H. Li, Z.Z. Zhang, C.X. Shan, J. Y. Zhang, X.W. Fan, G.T. Du, Growth of vertically aligned single crystal ZnO nanotubes by plasma-molecular beam epitaxy, Solid State Commun. 137 (2006) 182–186.

[20] T. Thongtem, A. Phuruangrat, S. Thongtem, Characterization of nanostructured ZnO produced by microwave irradiation, Ceram. Int. 36 (2010) 257–262.

[21] K. Haga, M. Kamidaira, Y. Kashiwaba, T. Sekiguchi, H. Watanabe, ZnO thin films prepared by remote plasma-enhanced CVD method, J. Cryst. Growth 214-215 (2010) 77–80.

[22] Y. Kashiwaba, F. Katahira, K. Haga, T. Sekiguchi, H. Watanabe, Heteroepitaxial growth of ZnO thin films by atmospheric pressure CVD method, J. Cryst. Growth 221 (2000) 431–434.

[23] T.L. Phan, S.C. Yu, R. Vincent, N.H. Dan, W.S. Shi, Photoluminescence properties of various CVD-grown ZnO nanostructures, J. Lumin. 130 (2010) 1142–1146.

[24] Y. Köseoğlu, A simple microwave-assisted combustion synthesis and structural, optical and magnetic characterization of ZnO nanoplatelets, Ceram. Int. 40 (2014) 4673–4679.

[25] D. Li, J. Wang, X. Wu, C. Feng, X. Li, Ultraviolet-assisted synthesis of hourglass-like ZnO microstructure through an ultrasonic and microwave combined technology, Ultrason. Sonochem. 20 (2013) 133–136.

[26] Powder diffraction file, JCPDS-ICDD, 12 Campus Boulevard, Newtown Square, PA 19073-3273, USA, 2001.

[27] H.M. Cheng, K.F. Lin, H.C. Hsu, C.J. Lin, L.J. Lin, W.F. Hsieh, Enhanced resonant Raman scattering and electron-phonon coupling from self-assembled secondary ZnO nanoparticles, J. Phys. Chem. B 109 (2005) 18385–18390.

[28] O. Yayapao, T. Thongtem, A. Phuruangrat, S. Thongtem, Sonochemical synthesis of Dy-doped ZnO nanostructures and their photocatalytic properties, J. Alloys Compd. 576 (2013) 72–79.

[29] O. Yayapao, S. Thongtem, A. Phuruangrat, T. Thongtem, Sonochemical synthesis, photocatalysis and photonic properties of 3% Ce-doped ZnO nanoneedles, Ceram. Int. 39 (2013) S563–S568.

[30] S. Baruah, J. Dutta, Hydrothermal growth of ZnO nanostructures, Sci. Technol. Adv. Mater. 10 (2009) 013001.

[31] Z.L. Wang, ZnO nanowire and nanobelt platform for nanotechnology, Mater. Sci. Eng. R 64 (2009) 33–71.

[32] X.L. Hu, Y.J. Zhu, S.W. Wang, Sonochemical and microwave-assisted synthesis of linked single-crystalline ZnO rods, Mater. Chem. Phys. 88 (2004) 421–426).

[33] A. Umar, M.M. Rahman, A. Al-Hajry, Y.B. Hahn, Highly-sensitive cholesterol biosensor based on well-crystallized flower-shaped ZnO nanostructures, Talanta 78 (2009) 284–289.

[34] Y.J. Gao, W.C. Zhang, X.L. Wu, Y. Xia, G.S. Huang, L.L. Xu, J. C. Shen, G.G. Siu, P.K. Chu, Hydrothermal self-assembling of ZnO nanorods into sphere-like superstructures and their optical characteristics, Appl. Surf. Sci. 255 (2006) 1982–1987.

[35] R.B. Kale, Y.J. Hsu, Y.F. Lin, S.Y. Lu, Synthesis of stoichiometric flowerlike ZnO nanorods with hundred per cent morphological yield, Solid State Commun. 142 (2007) 302–305.

[36] T. Ghoshal, S. Kar, J. Ghatak, S. Chaudhuri, ZnO nanocones: solvothermal synthesis and photoluminescence properties, Mater. Res. Bull. 43 (2008) 2228–2238.

[37] S. Musić, Đ. Dragčević, S. Popović, Influence of synthesis route on the formation of ZnO particles and their morphologies, J. Alloys Compd. 429 (2007) 242–249.

[38] Y. Zhang, J. Mu, Controllable synthesis of flower- and rod-like ZnO nanostructures by simply tuning the ratio of sodium hydroxide to zinc acetate, Nanotechnology 18 (2007) 075606.

[39] P. Li, H. Liu, Y.F. Zhang, Y. Wei, X.K. Wang, Synthesis of flower-like ZnO microstructures via a simple solution route, Mater. Chem. Phys. 106 (2007) 63–69.

[40] S.C. Padmanabhan, D. Ledwith, S.C. Pillai, D.E. McCormack, J. M. Kelly, Microwave-assisted synthesis of ZnO micro-javelins, J. Mater. Chem. 19 (2009) 9250–9259.

[41] P. Li, Y. Wei, H. Liu, X. Wang, Growth of well-defined ZnO microparticles with additives from aqueous solution, J. Solid State Chem. 178 (2005) 855–860.

[42] Q. Xie, Z. Dai, J. Liang, L. Xu, W. Yu, Y. Qian, Synthesis of ZnO three-dimensional architectures and their optical properties, Solid State Commun. 136 (2005) 304–307.

[43] J. Xie, H. Wang, M. Duan, L. Zhang, Synthesis and photocatalysis properties of ZnO structures with different morphologies via hydrothermal method, Appl. Surf. Sci. 257 (2011) 6358–6363.

[44] X. Li, Y. Cheng, S. Kang, J. Mu, Preparation and enhanced visible light-driven catalytic activity of ZnO microrods sensitized by porphyrin heteroaggregate, Appl. Surf. Sci. 256 (2010) 6705–6709.

[45] S. Ma, R. Li, C. Lv, W. Xu, X. Gou, Facile synthesis of ZnO nanorod arrays and hierarchical nanostructures for photocatalysis and gas sensor applications, J. Hazard. Mater. 192 (2011) 730–740.

[46] J. Yang, J. Wang, X. Li, J. Lang, F. Liu, L. Yang, H. Zhai, M. Gao, X. Zhao, Effect of polar and non-polar surfaces of ZnO nanostructures on photocatalytic properties, J. Alloys Compd. 528 (2012) 28–33.

[47] Y. Lai, M. Meng, Y. Yu, X. Wang, T. Ding, Photoluminescence and photocatalysis of the flower-like nano-ZnO photocatalysts prepared by a facile hydrothermal method with or without ultrasonic assistance, Appl. Catal. B 105 (2011) 335–345.